N^o d'Ordre : D.U. **2182** PCCF T 1111

UNIVERSITE BLAISE PASCAL
U.F.R. Sciences et Technologies

ECOLE DOCTORALE DES SCIENCES FONDAMENTALES
N^o 695

THESE

présentée pour obtenir le grade de

DOCTEUR D'UNIVERSITE

Spécialité : Physique Corpusculaire

par **AHN Sang Un**

titulaire d'un Master of Physics

Analysis of Υ production in pp collisions at 7 TeV with the ALICE Muon Spectrometer

Soutenue publiquement le 5 décembre 2011, devant la commission d'examen

Président :	M. E. VERCELLIN	(Rapporteur)
Examinateurs :	M. P. DUPIEUX	
	M. D-W. KIM	
	M. S-K. OH	
	M. P. ROSNET	
	Mme J. SONG	(Rapporteur)

박사학위 청구논문
지도교수 **Philippe Rosnet**, 오선근

CERN 거대 강입자 가속기 실험에서 ALICE 뮤온 분광기를 이용한 Υ 입자 생성 연구

Analysis of Υ production in pp collisions at 7 TeV with the ALICE Muon Spectrometer

2012년 2월

건국대학교 대학원

물리학과

안상언

CERN 거대 강입자 가속기 실험에서 ALICE 뮤온 분광기를 이용한 Υ 입자 생성 연구

Analysis of Υ production in pp collisions at 7 TeV with the ALICE Muon Spectrometer

이 논문을 이학 박사학위 청구논문으로 제출합니다

2012년 2월

건국대학교 대학원

물리학과

안상언

안상언의 이학박사학위 청구논문을 인준함

심사위원장	**Ermanno Vercellin**	(인)
심사위원	**Pascal Dupieux**	(인)
심사위원	김도원	(인)
심사위원	송정현	(인)
심사위원	**Philippe Rosnet**	(인)
심사위원	오선근	(인)

2011년 12월

건국대학교 대학원

Contents

ABSTRACT

Analysis of Υ production in pp collisions at 7 TeV with the ALICE Muon Spectrometer

ALICE experiment is a general-purpose detector designed to study the Quark-Gluon Plasma in heavy-ion collisions at CERN LHC. One of powerful probe to the QGP is the heavy quarkonium production in heavy-ion collisions compared to the pp collisions. The interests of the heavy quarkonium production is not limited in heavy-ion physics since its production mechanism in pp collisions is still ambiguous. The aim of this thesis work is to estimate the production cross section of $\Upsilon(nS)$ in pp collisions at $\sqrt{s}$ = 7 TeV in their muon decay channel with the ALICE muon spectrometer. The ALICE muon spectrometer is located at the forward rapidity region $-4 < y < -2.5$. It consists of a set of absorbers, a warm dipole magnet, tracking and trigger stations. The online monitoring software for muon trigger system described in this thesis work has been developed in order to help efficient data taking. A part of data taken in 2010 has been analyzed to estimate Υ production cross section. The published J/ψ production cross section in pp collisions at the same energy is exploited in the estimation method. The preliminary result in the rapidity range $2.5 < y < 4$ is $\sigma_{\Upsilon(1S)} \times B_{\Upsilon(1S)\to\mu^+\mu^-} = 0.62 \pm 0.38(stat.)^{+0.12}_{-0.21}(syst.)$ nb per rapidity unit.

Keywords: CERN LHC, ALICE, Muon Spectrometer, Υ, cross section

Introduction

In 2010, the proton-proton collisions at the world highest energy[1] was successfully performed at CERN Large Hadron Collider which is located in the circular tunnel with 27 km circumference buried under the ground straddled the border of France and Switzerland in Geneva. The CERN LHC is designed to collide protons at $\sqrt{s}$ = 14 TeV energy and lead-ions at $\sqrt{s}$ = 5.5 TeV. In autumn in the same year, the lead-ion beam was successfully circulated and collided at $\sqrt{s_{\rm NN}}$ = 2.76 TeV (half of its nominal value) for a month. It has been expected that the CERN LHC will open the new energy regime and help to explore the uncovered physics.

In order to collect and exploit the new data to be produced at LHC energy, several huge complicated detectors have been designed and built for a decade. They are ALICE[2], ATLAS[3], CMS[4] and LHCb[5], alphabetically. In particular, ALICE is a detector dedicated to the heavy-ion physics which focused on the collective phenomena created in the ultra-relativistic heavy-ion collisions. The ALICE detector has a forward muon arm named the ALICE muon spectrometer in order to study the processes involving muons, such as low-mass resonances, heavy quarkonia, open-charm and beauty production, etc. Especially, heavy quarkonium states like J/ψ, ψ' (charmonium states) have provided a powerful tool to characterize new state of matter, such as the Quark-Gluon Plasma (QGP), via its di-muon decay channel. In addition to the charmonium states, at LHC energy, the bottomonium states, Υ fam-

[1]The collision energy $\sqrt{s} = 7$ TeV. The former world record was $\sqrt{s} = 1.96$ TeV at Tevatron

[2]A Large Ion Collider Experiment

[3]A Toroidal LHC ApparatuS

[4]Compact Muon Solenoid

[5]LHC beauty

ily, will be produced with more than an order of magnitude relative to the previous experiments and, thus, will provide a new probe to the QGP.

In this thesis, a preliminary result on the Υ production via its di-muon decay channel will be presented in Chapter 4 after the analysis of the data collected in pp collisions at $\sqrt{s} = 7$ TeV in the year 2010. Also, the detailed description of the software framework developed for the Υ analysis is presented in Chapter 2, together with the design and performance of the ALICE sub-detectors as well as the details of the ALICE muon spectrometer. A whole chapter is assigned to describe the on-line monitoring software development for the ALICE muon trigger system in Chapter 3. In the following chapter, a brief introduction to the strong interaction, QCD phase diagram, heavy quarkonium in the medium, and its hadroproduction will be presented. The axial coordinate system of the ALICE experiment, kinematic variables often used in this thesis and glossary are presented in the Appendices.

Chapter 1

Heavy Quarkonia and the QGP

1.1 Strong interaction and QCD phase transition

The origin of the strong interaction was started from some ideas introduced to explain how protons and neutrons can be combined inside a nucleus. The first idea was that the strength of this kind of force is simply greater than that of the electromagnetism. In other words, repulsive interaction between positive charged protons is overwhelmed by the force that binds protons together inside the atom,

$$\alpha_s \sim 1 (\text{while } \alpha_{em} \sim 10^{-2})$$

where α_s is the coupling constant of strong interaction, α_{em} is the coupling constant of electromagnetic interaction. On the other hand, the strong force does not affect the electrons located at relatively large distance. This leads to the second idea that the force is effective only at a short distance, namely the size of proton, ~ 1 fm. As the quark model has been developed, it is well known that a hadron, such as proton and neutron, consists of quarks and it has turned out that the protons and neutrons are bound together in a nucleus due to the strong interaction between quarks propagated by gluons. The theory of the interaction between quarks and gluons has been established and it is called *Quantum Chromodynamics* (QCD).

The main concept of the QCD is the color charge which is analogous to

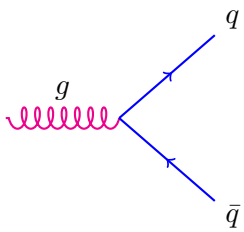

Figure 1.1: The fundamental form of quark-gluon interaction. The color charge is exchanged at the vertex.

the electric charge of the electromagnetism. It was insufficient to describe the strong interaction with only electric charge of quarks, which is a fractional charge. In QCD, a quark carries not only an electric charge, but also a color charge. There are three kinds of colors: Red, Blue and Green. A striking feature of QCD is that the color charge is not only carried by the quarks, but also carried by the gluons. The color charge is exchanged between quarks via a gluon at a vertex in a process (see Fig. 1.1). This leads to the fact that there are eight possible gluons in the combination of color and anti-color: it is called color-octet state,

$$
\begin{aligned}
|1\rangle &= (r\bar{b} + b\bar{r})/\sqrt{2} & |5\rangle &= -i(r\bar{g} - g\bar{r})/\sqrt{2} \\
|2\rangle &= -i(r\bar{b} - b\bar{r})/\sqrt{2} & |6\rangle &= (b\bar{g} + g\bar{b})/\sqrt{2} \\
|3\rangle &= (r\bar{r} - b\bar{b})/\sqrt{2} & |7\rangle &= -i(b\bar{g} - g\bar{b})/\sqrt{2} \\
|4\rangle &= (r\bar{g} + g\bar{r})/\sqrt{2} & |8\rangle &= (r\bar{r} + b\bar{b} - 2g\bar{g})/\sqrt{6}
\end{aligned}
$$

where r, b and g represent the three kinds of colors: Red, Blue and Green, respectively. Color-singlet state of gluon is forbidden because *white* gluon is not allowed. The color charge of gluons allows gluons to interact between themselves. This makes higher-order Feynman diagrams of the strong interaction not to be neglected and QCD calculation difficult.

The behavior of the coupling strength in QCD depending on the interaction distance is unique. On the one hand, in contrast to the electromagnetism, the longer is the distance between quark and anti-quark pair, the larger is the attractive strength between them. In other words, the energy that binds the quark and anti-quark pair together becomes larger when one tries to separates them. On the limit of the energy (or at a long distance)

enough to create a new quark and anti-quark pair, the binding of the original quark and anti-quark pair breaks and each quark and anti-quark are bound with the new quark and anti-quark into new two quark and anti-quark pairs. This is why an isolated (free) quark has never been observed. It is known as the *confinement* that quarks and gluons are always in a state forming a hadron. On the other hand, the shorter is the distance between the quark and anti-quark pair, the smaller is the strength of the coupling. In particular, the coupling strength of the strong interaction becomes weak as the momentum transfer, Q^2, is larger in a process (or *vice versa*). As a consequence, quarks become free at high energy which is called *asymptotic freedom* [1]. Therefore, the coupling strength of the strong interaction, α_s, is expressed as

$$\alpha_s(Q^2) \sim A \left[1/\ln \left(\frac{Q^2}{\Lambda^2_{\rm QCD}} \right) \right]$$

where the coefficient A is determined by the number of flavors (u, d, s, c, b and t) in a process and $\Lambda_{\rm QCD}$ is the QCD confinement scale which represents the typical binding energy of a hadron that depends on its mass. Figure 1.2 shows the summary of measurements of strong coupling as a function of the momentum transfer. The value of $\Lambda_{\rm QCD}$ is determined by experiments and known as,

$$\Lambda_{\rm QCD} \sim 200 \ \text{MeV} \ [3].$$

At the limit, $Q^2 \gg \Lambda^2_{\rm QCD}$, the coupling strength becomes much smaller, and thus the quarks and anti-quarks (almost) do not feel any constraints between them as if they are free from the *hadronic jail*. This is called *deconfinement*. This state can also be reached by squeezing hadrons tightly into a very small area. That is like increasing hadron (in particular, baryon like proton and neutron) density or energy density. The typical energy density of a nucleus is

$$\epsilon_{nucl} \sim 0.15 \ \text{GeV/fm}^3$$

At the limit, $\epsilon \sim 1$ GeV/fm^3, the quarks and gluons become free states, such a state of matter is called the Quark-Gluon Plasma (QGP).

The QGP is thought to be existed at the early stage of the evolution

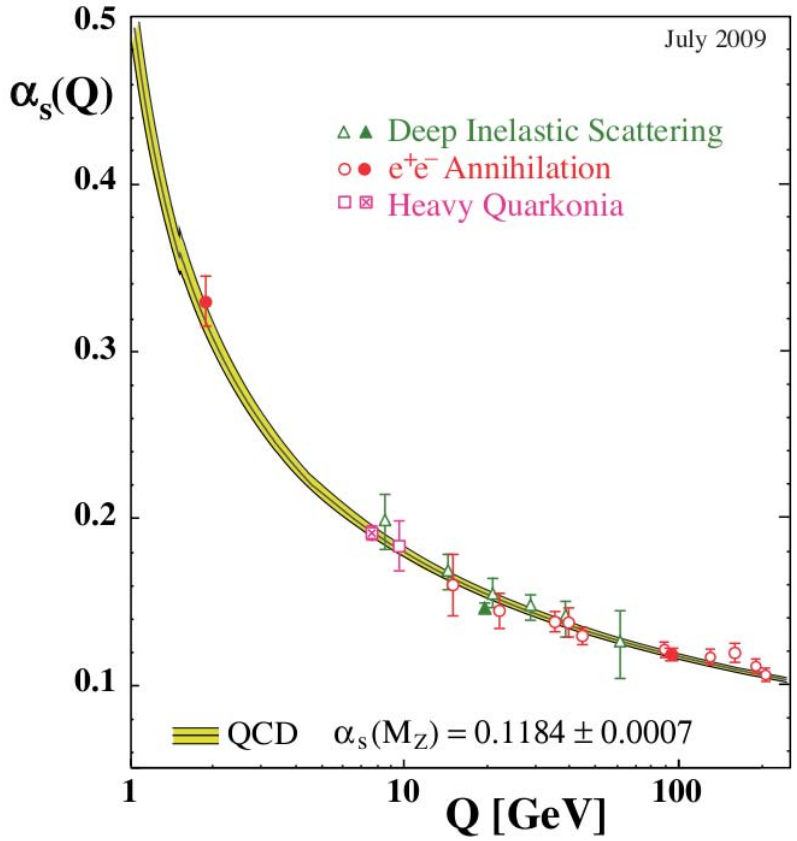

Figure 1.2: Summary of measurements of α_s as a function of Q [2].

of Universe after the Big Bang. After a few millionths of a second, at the temperature of order $T \sim 170$ MeV, the quarks and gluons start binding together confined into hadrons. In addition, the QGP can be found inside the cores of neutron stars, while unlike the matter formed after the Big Bang, this matter is *cold*. The nature of the QGP is an issue of fundamental interest. Thus the goal of heavy-ion physics is to recreate such a matter in the laboratory via ultra-relativistic heavy-ion collisions. The term "ultra-relativistic" is defined by the requirement to reach or exceed energy densities $\epsilon \sim 1$ GeV/fm^3. The required center of mass nucleus-nucleus energy $\sqrt{s_{\rm NN}}$ in heavy-ion collisions turned out to be $\sqrt{s_{\rm NN}} \geq 10$ GeV [4].

The whole picture of such variation of the state of the matter (hadrons) is drawn by the lattice calculation of QCD. The recent lattice QCD calculations at zero net-baryon density predicts that the phase transition from the hadrons to the deconfinement occurs at the temperature $T \sim 170$ MeV. And it suggests a phase diagram of QCD matter and its states in the plane of the temperature T and baryon number density (or baryon number chemical potential μ_B). At low energies the *fireball* produced after a collision contains about equal numbers of newly created quark-anti-quark pairs (of zero net baryon number) and of initial valence quarks that leads to a high μ_B value. Conversely, at (designed) LHC energy (5.5 TeV for Pb–Pb collisions), the initial valence quarks constitute a only 5% fraction of the total quark density that results in a small value of μ_B. In the extreme, the matter created after the Big Bang evolves toward hadronization (at $T_c = 170$ MeV) featuring $\mu_B \approx 0$.

A sketch of the QCD phase diagram is shown in Fig. 1.3. The (dominating) black band indicates the phase transition between hadron matter and the QGP. It interpolates between the extremes of predominant matter heating (high T, low μ_B) and predominant matter compression ($T \rightarrow 0, \mu_B > 1$ GeV). Onward from the later conditions, the transition is expected to be of first order [6] until the critical point of QCD matter is reached at $200 \leq \mu_B(E) \leq 500$ MeV. The relatively large position uncertainty reflects the preliminary calculations of lattice QCD. Onward from the critical point, E, the phase transformation at lower μ_B is a rapid cross-over [7].

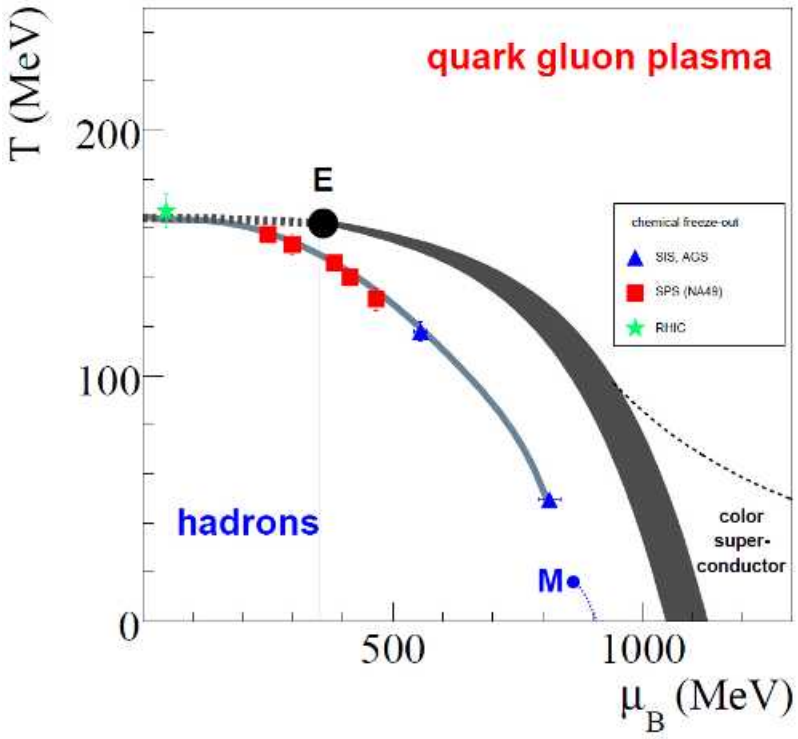

Figure 1.3: Sketch of the QCD matter phase diagram in the plane of temperature T and baryo-chemical potential μ_B. The parton-hadron phase transition line from lattice QCD ends in a critical point E. A cross-over transition occurs at smaller μ_B (see [5] and references therein).

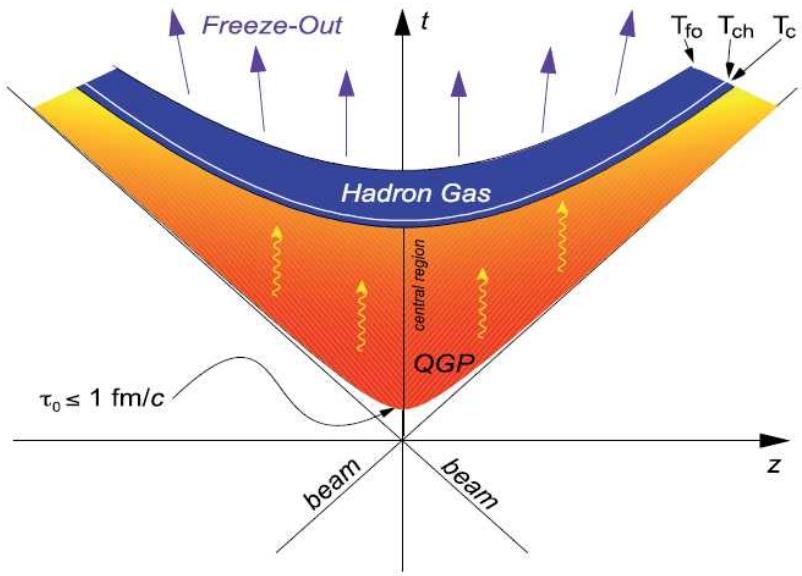

Figure 1.4: Schematic light cone diagram of the evolution of a high energy heavy-ion collision, indicating a QGP formation time τ_0 [5] (see text).

The hadronic freeze-out points are determined from data obtained in the nucleus-nucleus collisions at the various incident energy ranges from SIS at GSI via AGS at BNL and NA49 at CERN SPS to RHIC energies, *i.e.* $3 \leq \sqrt{s_{\rm NN}} \leq 200$ GeV. These points indicate the μ_B domain of the phase diagram that is accessible by the relativistic nuclear collisions. The domain at $\mu_B \geq 1.5$ GeV where a new phase of QCD featuring Color-Flavor Locking (CFL) and Color Superconductivity [8, 9] is predicted will probably be accessible only by astrophysical observation.

1.2 Dynamical evolution of a heavy-ion collision in space-time

The dynamical evolution in space-time of a central heavy-ion collision is sketched in Fig. 1.4 by means of a schematic 2-dimensional light cone diagram. Soon after the collision of the two nuclei[1], the energy density may be

[1]In ultra-relativistic heavy-ion collisions, such as Pb–Pb collisions at LHC, two nuclei traveling at relativistic speeds become longitudinally Lorentz-contracted discs.

sufficiently high enough to allow the formation of a Quark-Gluon Plasma in the central region. As the system expands, the temperature drops down and the hadronization takes place. Below the freeze-out temperature, hadrons stream out of the collision region. The entire process can be summarized as follows:

- pre-equilibrium (proper time τ_0<1 fm/c): hard and soft processes occur during the parton scattering;
- thermalization (possibly occurring at $\tau \sim 1 - 2$ fm/c): the multiple scattering among the quark and gluon constituents of the colliding nucleons and the particles newly produced during the collisions lead to the thermalization;
- QGP formation ($1 < \tau < 10 - 15$ fm/c): at high energy densities the system reaches the deconfinement phase with partonic degrees of freedom;
- hadronization ($\tau \sim 20$ fm/c): the temperature of the expanding medium drops down and, below the critical temperature T_c, the quarks and gluons becomes confined into hadrons;
- freeze-out ($\tau \to \infty$): the expansion and the temperature fall lead to a reduction of the inelastic processes among hadrons, until the relative abundance of hadron species is fixed (chemical freeze-out), and then to the stop of any interaction which fixes the kinematic spectra (kinetic freeze-out).

1.3 Observables to probe the QGP

In order to verify the existence of the phase transition and the formation of the Quark-Gluon Plasma in heavy-ion collisions, physics observable quantities having the information about the state of the produced medium during distinct stages of the dynamical evolution have to be identified. Ordered in sequence of their formation in the course of the dynamics, the most relevant observables are briefly characterized in what follows:

- Suppression of heavy quarkonia (J/ψ and Υ) production by Debye-screening in the QGP: the vector mesons produced from primordial creation of $c\bar{c}$ and $b\bar{b}$ pairs that would hadronize unimpeded in elementary collisions but are broken up at a certain temperature thresholds if immersed into a deconfined QGP.

- Suppression of di-jets (Jet quenching in A–A collisions): two quarks or gluons are produced in a collision, one of them leaves the medium directly while the other one traverses the medium and then is attenuated. The undisturbed parton hadronizes and forms a jet while the other one is absorbed in the medium and is not detected (or distorted).

- High-p_{t} particles: a variant of di-jet suppression. High p_{t} particles produced in primordial $q\bar{q}, gg$ or qq reactions with high momentum transfer are attenuated by gluonic bremsstrahlung ($q + q \rightarrow q + q + g$) in QGP-medium.

- Hydrodynamic collective motion, "flow", develops with the onset of thermal equilibrium. It is created by partonic pressure gradients that reflect the initial collisional impact geometry via anisotropies in particle emission called "directed" and "elliptic" flow. The latter reveals properties of the QGP.

- Hadronic "chemical" freeze-out fixes the abundance ratios of the hadronic species. Occurring close to, or at hadronization, it reveals the dynamical evolution path in QCD phase diagram and determines the critical temperature and density of QCD.

- Fluctuations from one collision event to another: it can be quantified in Pb–Pb collisions due to the high charged hadron multiplicity density ($\simeq 1500$ per rapidity unit at LHC energy [10]). This reflects the existence and position of the critical point of QCD.

- Two particle Bose-Einstein-Correlations: the analog of the Hanbury-Brown, Twiss (HBT) effect of quantum optics. They result from the last interaction experienced by hadrons, *i.e.* from the "kinetic" freeze-

out stage. They reveal information on the overall space-time development of the "fireball" evolution.

1.4 Heavy quarkonium as a probe of the QGP

Heavy quarkonium is a meson state composed of a heavy quark, such as c quark or b quark, and its anti-quark. There are two kinds of heavy quarkonium that have been found[2], they are "charmonium" and "bottomonium". The charmonium is a $c\bar{c}$ bound state, such as J/ψ, ψ', χ_c, etc. The bottomonium is a $b\bar{b}$ bound state, such as Υ, Υ', Υ'', χ_b, etc.

1.4.1 The discovery of heavy quarkonia

J/ψ meson is the firstly revealed $c\bar{c}$ bound state of charmonia with mass ~ 3.1 GeV/c^2 and it was found in 1974. Its discovery was made in different laboratories at the almost same time, Brookhaven National Laboratory (BNL) [11] (see Fig. 1.5a) and Stanford Linear Accelerator Center (SLAC) [12] (see Fig. 1.5b). The first excited state of J/ψ, the ψ' (or $\psi(2S)$) was discovered by the same group at SLAC.

In 1977, new resonance in the higher mass region ~ 9.5 GeV/c^2 was found via muon pair detection at Fermi National Accelerator Laboratory (FNAL) [13] (see Fig. 1.6) in proton-nucleus collisions at $\sqrt{s} = 400$ GeV. The resonance was named Υ and turned out that it is a meson system composed of b quark and its anti-quark. Like the J/ψ case, the first excited state Υ' (or $\Upsilon(2S)$) was directly found [14], and the $\Upsilon(3S)$ state and an evidence of $\Upsilon(4S)$ state were found at FNAL [15] in turn.

In addition, there had been efforts to find the unhidden c and b quarks from their quark-antiquark bound states since an isolated quark is not allowed due to the confinement feature of QCD (see Section 1.1). The first charmed meson named D^0 was found in 1976 [16], and the first charged charmed meson, D^+ was discovered [17] after that. The first charmed baryon, Λ_c^+, was also discovered in the same year [18]. For the first bottom meson,

[2] A bound state of a top quark and its anti-quark, called "toponium", has not been found.

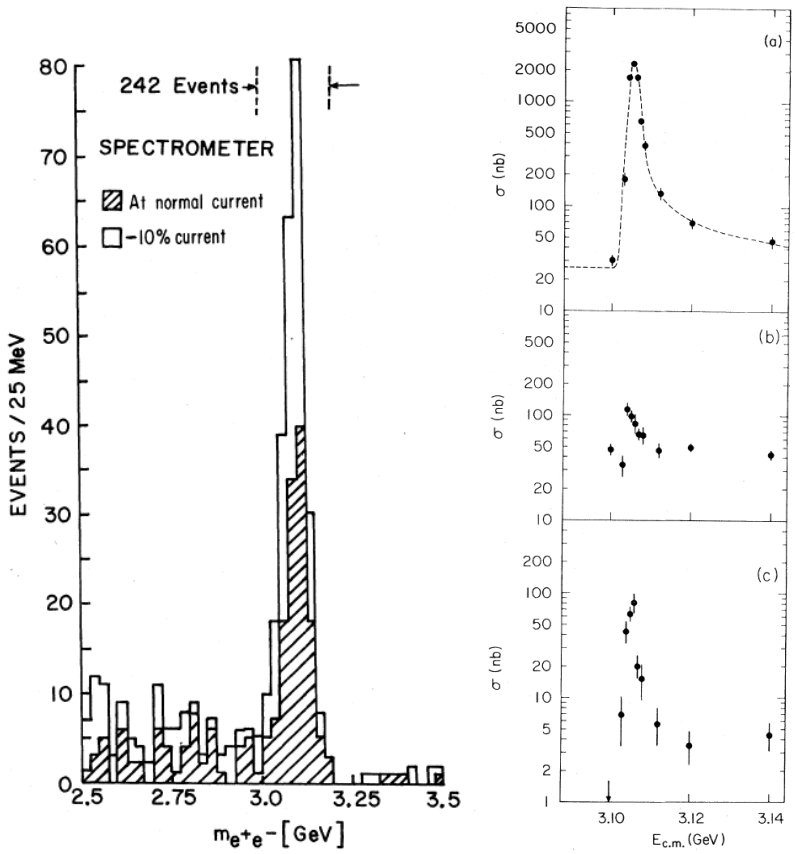

Figure 1.5: Mass spectrum showing the existence of J/ψ meson reported by (a) BNL [11] and (b) SLAC [12].

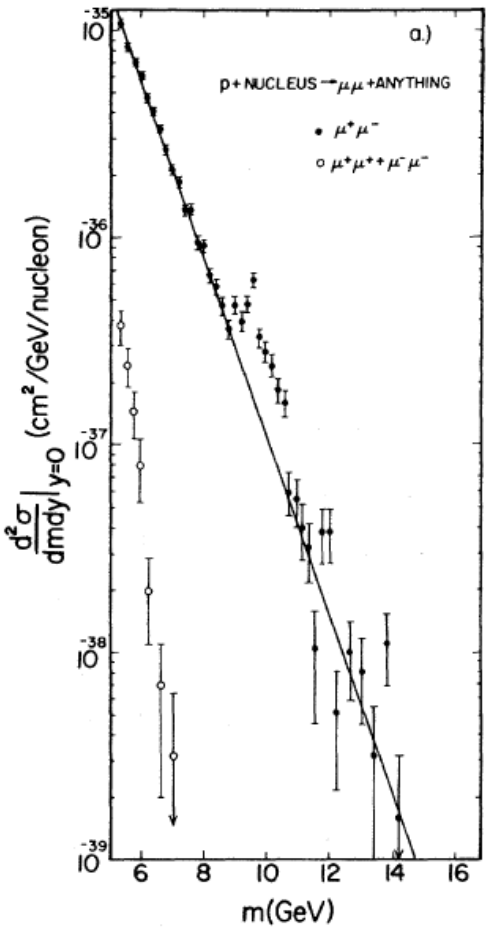

Figure 1.6: Measured di-muon production cross section as a function of the invariant mass of the muon pair [13]. The closed circles are data points of unlike sign muon pair and the open circles are that of like sign muon pair. The solid line is the continuum fit.

B, its evidence was confirmed by the CLEO collaboration in 1980 [19], and in the following year, the first evidence for baryons with b quark, Λ_b^0, was reported at CERN [20].

1.4.2 The characteristic of heavy quarkonium

The mass of heavy quarks m_Q[3], $m_c \simeq 1.5$ GeV/c^2 and $m_b \simeq 4.7$ GeV/c^2 are larger than the QCD confinement scale $\Lambda_{\rm QCD}$ (see Section 1.1). Thus, one can expect that the strong coupling constant α_s will be smaller than 1. Since the typical velocity (relative with respect to the speed of light, c) of heavy quarks inside the bound state is small compared to the light quarks ($v^2 \sim 1$), $v^2 \sim 0.3$ for $c\bar{c}, v^2 \sim 0.1$ for $b\bar{b}$, the bound system of heavy quarkonium is non-relativistic. The non-relativistic hierarchy of energy scales,

$$m_Q \gg p \ \sim 1/r \sim m_Q v \gg E \sim m_Q v^2$$

where r is the distance between the heavy quark and the anti-quark, and m_Q is the heavy quark mass (hard scale), p is the momentum (soft scale), and E is the binding energy (ultra-soft scale). The strong coupling constant, α_s, is small, $\alpha_s(m_Q) \ll 1$ for the mass scale, since $m_Q \gg \Lambda_{\rm QCD}$. Also, possibly $\alpha_s(m_Q v) \ll 1$ for the momentum scale if $m_Q v \gg \Lambda_{\rm QCD}$. The strong coupling constant, α_s, as a function of quarkonium radius r is shown in Fig. 1.7.

The bound state of heavy quarks can be described by the non-relativistic Schrödinger equation,

$$\left(-\frac{\nabla^2}{2(m_Q/2)} + V(r)\right)\Psi(r) = E\Psi(r)$$

where $m_Q/2$ is a reduced mass, E is the binding energy, and $V(r)$ is the static $Q\bar{Q}$ potential in the form of,

$$V(r) = \kappa r - \frac{4}{3}\frac{\alpha_s}{r},$$

where r is the distance between the quark and the anti-quark, κ is the string tension which represents the strength of quark confinement force. The po-

[3] heavy quarks are denoted by Q; (small) q for light quarks.

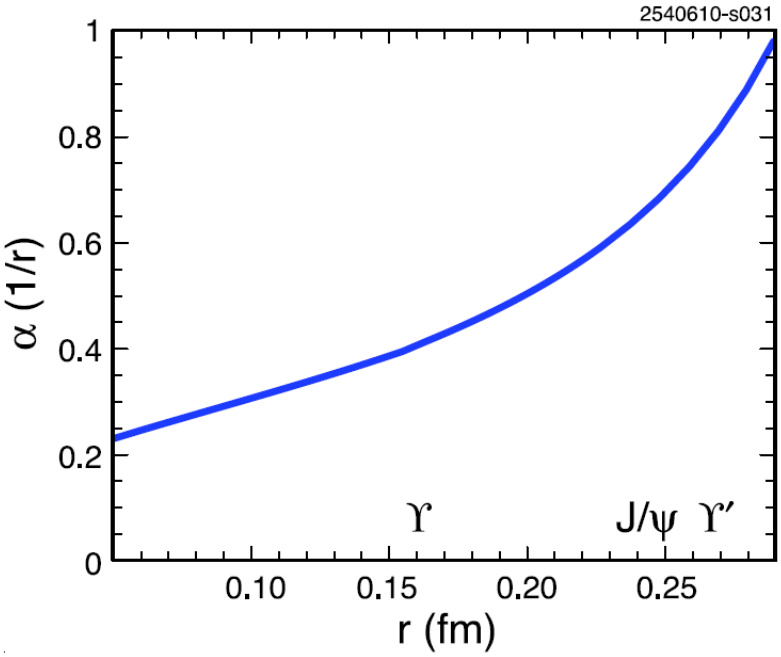

Figure 1.7: The strong coupling constant, α_s, as a function of quarkonium radius r, with labels indication approximate values of $m_Q v$ for $\Upsilon(1S)$, J/ψ, and $\Upsilon(2S)$ [21].

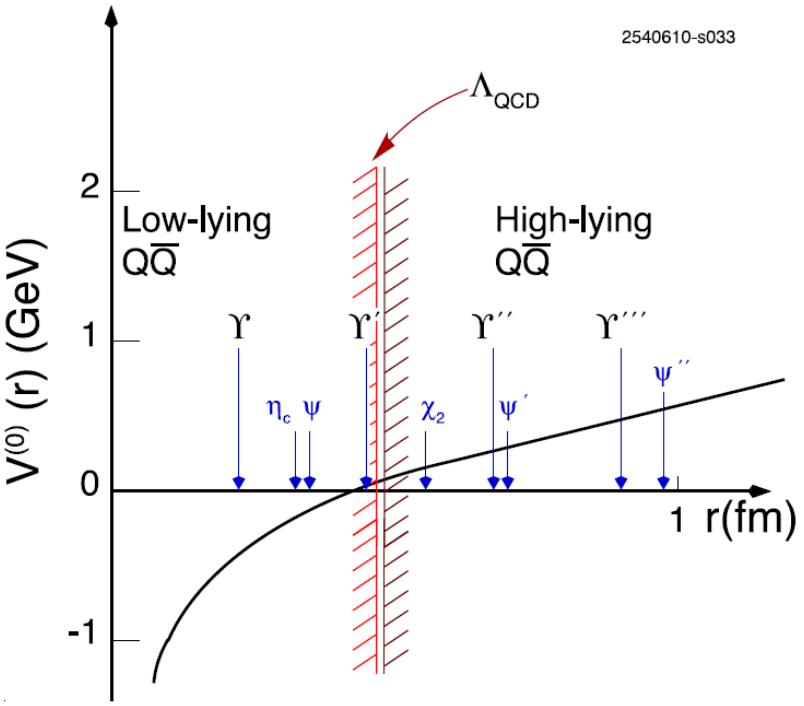

Figure 1.8: Static $Q\bar{Q}$ potential as a function of quarkonium radius r [21].

tential represents the Coulomb-like behavior, $V \sim 1/r$, of the strong interaction at short range and the confinement increasing without limit at long distances, $V \sim r$. This is depicted in Fig. 1.8.

1.4.3 Heavy quarkonium in hot medium

The string tension, κ, will decrease as the temperature T approaches the critical temperature T_c, and it eventually vanishes above T_c. The binding between Q and $\bar{Q}$, thus, becomes weak. In addition, the QCD string between the heavy quarks will be broken at long distances due to the light quark pairs, $q\bar{q}$ in such a hot environment. Hence, the heavy quark pairs, $Q\bar{Q}$, break up into heavy-light quark pairs, $Q\bar{q}$ and $\bar{Q}q$. Then, $V(r)$ becomes flat above some critical distance. For $T > T_c$, the confining potential disappears. We thus expect,

$$V_{\text{eff}}(r) = -\frac{4}{3}\frac{\alpha_s}{r} exp[-r/r_D(T)]$$

Table 1.1: Upper bounds on the dissociation temperatures [24].

state	χ_c	ψ'	J/ψ	Υ'	χ_b	Υ
T_{diss}	$\leq T_c$	$\leq T_c$	$1.2T_c$	$1.2T_c$	$1.3T_c$	$2T_c$

where $r_D(T)$ is the Debye screening radius which depends on the temperature. When the screening radius, r_D, falls below the binding radius, r, of heavy quarkonia, the quark and its anti-quark can no longer *see* each other. Hence the bound state becomes dissociated [22]. Otherwise, the effective potential still supports the bound state when the radius r is smaller than r_D.

The screening radius and radii of heavy quarkonium states depend on the temperature. By pinning down the dissociation points of heavy quarkonia, we can determine the temperature of the QGP medium. In this respect, the measurement of the dissociation point of individual quarkonium states is referred to as a QGP thermometer [23]. An upper bound on the dissociation temperature for the different quarkonium states obtained from a full QCD calculation [24] are given in Tab. 1.1. All charmonium states are dissolved in the deconfined phase while the bottomonium $1S$ state may persist up to $\sim 2T_c$.

The dissociation of all charmonium states and the excited bottomonium states in deconfined medium leads to the reduction of the quarkonium yields in heavy-ion collisions compared to the pp collisions. However, not all of the observed quarkonium suppression is due to QGP formation. In fact, quarkonium suppression was also observed in proton-nucleus (p-A) collisions where no hot and dense matter effects are expected, so that part of the nucleus-nucleus suppression is due to Cold-Nuclear-Matter (CNM) effects. Therefore it is necessary to disentangle the CNM effects through p-A collisions.

1.4.4 Cold-Nuclear-Matter effects

There are several CNM effects. First, the shadowing effects which modifies the parton distribution functions in the nucleus relative to the nucleon. In particular, the gluon shadowing effects will plays a crucial role in the quarkonium production in hadronic collisions. Current shadowing models pa-

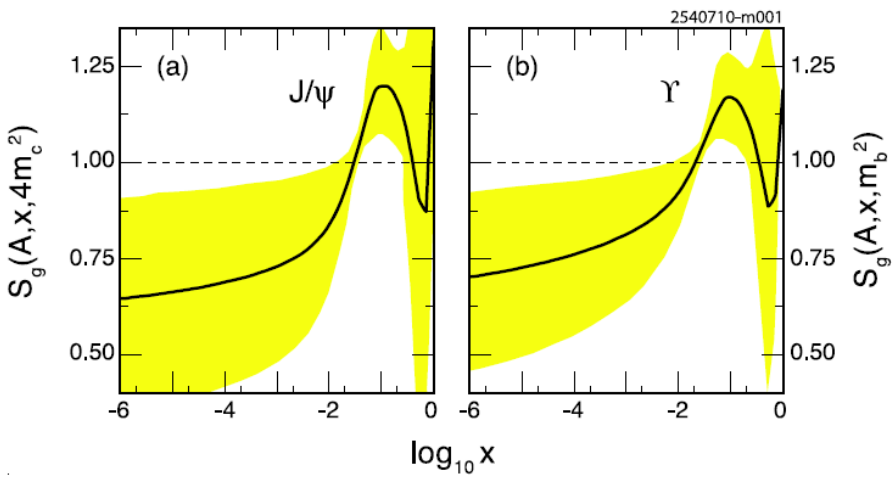

Figure 1.9: The EPS09 gluon-shadowing parameterization [25] at $Q = 2m_c$ and m_b. The central value (solid curves) and the associated uncertainty (shaded band) are shown.

rameterize the various experimental data to the nuclear parton densities. This effects with the possible range as a function of Bjorken-x[4] is shown in Fig. 1.9 [25]. Second, the nuclear absorption which represents break-up of the quarkonium state as it passes through the nucleus. The effect occurs after the $Q\bar{Q}$ pair has been produced and while it is traversing the nuclear medium. The probability to survive from the absorption depends on the quarkonium absorption cross section. Detailed analyses show that the quarkonium absorption cross section decreases with increasing energy [26, 27]. In addition, the energy loss of the parton traversing the nucleus before the hard scattering and a discussion of several types of energy-loss models is presented in [28].

1.4.5 Experimental results of heavy quarkonium suppression

The studies of charmonium suppression in heavy-ion collisions has been carried out by the several experiments: NA50 and NA60 experiments at CERN SPS, and PHENIX and STAR experiments at RHIC. The NA50 collaboration showed the results obtained in Pb–Pb collisions at 158 GeV/nucleon

[4] the momentum fraction carried by a parton compared to the nucleon

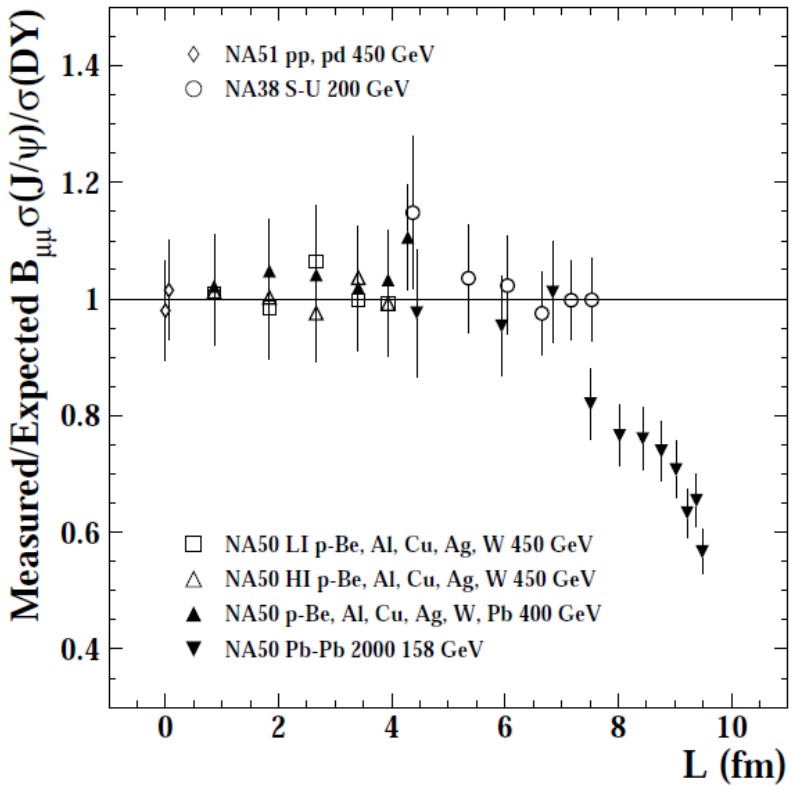

Figure 1.10: The J/ψ/Drell-Yan cross-sections ratio vs. L (see text) for several collision systems divided by the nuclear absorption pattern [29].

(see Fig. 1.10) of which J/ψ yield was suppressed with respect to the CNM effects [29]. The CNM effects has been extracted by extrapolating the J/ψ production data collected at higher energy (450 GeV) in p-A collisions than the Pb–Pb collisions and in a slightly different rapidity domain. The suppression pattern was shown as a function of the scale L, the average length of nuclear matter traversed by the $c\bar{c}$ state. The magnitude of J/ψ suppression was measured to be about 40%. However, the observed J/ψ suppression would be compatible with the suppression of χ_c and ψ' resonances if one considers that the contribution on the J/ψ production from higher resonances (χ_c and ψ') is $\sim 35\%$.

The NA60 collaboration measured the J/ψ production in p-A collisions and Pb–Pb collisions at the same energy. A new evaluation of the quarko-

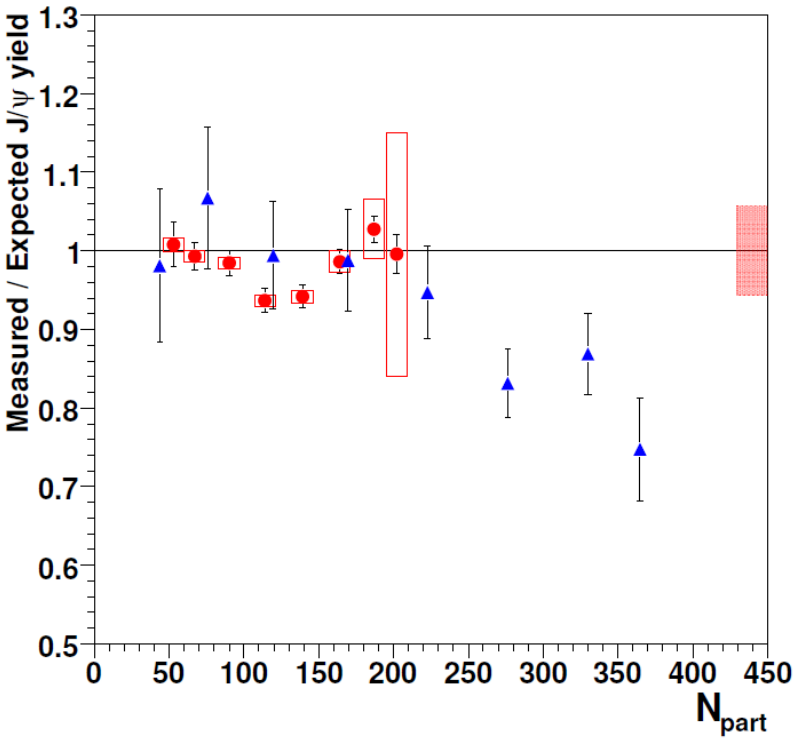

Figure 1.11: J/ψ suppression pattern in In–In (circles) and Pb–Pb (triangles) as a function of $N_{\rm part}$. Boxes around the points correspond to the correlated systematic errors, while the filled box on the right corresponds to the uncertainty on the absolute normalization of In–In points [30].

nium absorption in CNM was performed and a first attempt to consider the shadowing was addressed (detailed discussions can be found in [30]). The outcome of this analysis is that only about 20-30% of the suppression in the most central Pb–Pb collisions at SPS energies is indeed due to dissociation in hot QCD matter. The J/ψ suppression pattern observed by NA60 collaboration in In–In and Pb–Pb collisions as a function of $N_{\rm part}$, the number of participant nucleons, is shown in Fig. 1.11.

The PHENIX experiment at RHIC has published the observation of J/ψ suppression in central Au–Au collisions at $\sqrt{s_{\rm NN}} = 200$ GeV [31]. The result is shown in Fig. 1.12. The J/ψ suppression is roughly estimated to 40-80% in central Au–Au collisions at RHIC energy. The suppression is stronger at forward rapidity than at mid-rapidity and the physical interpretation is on-

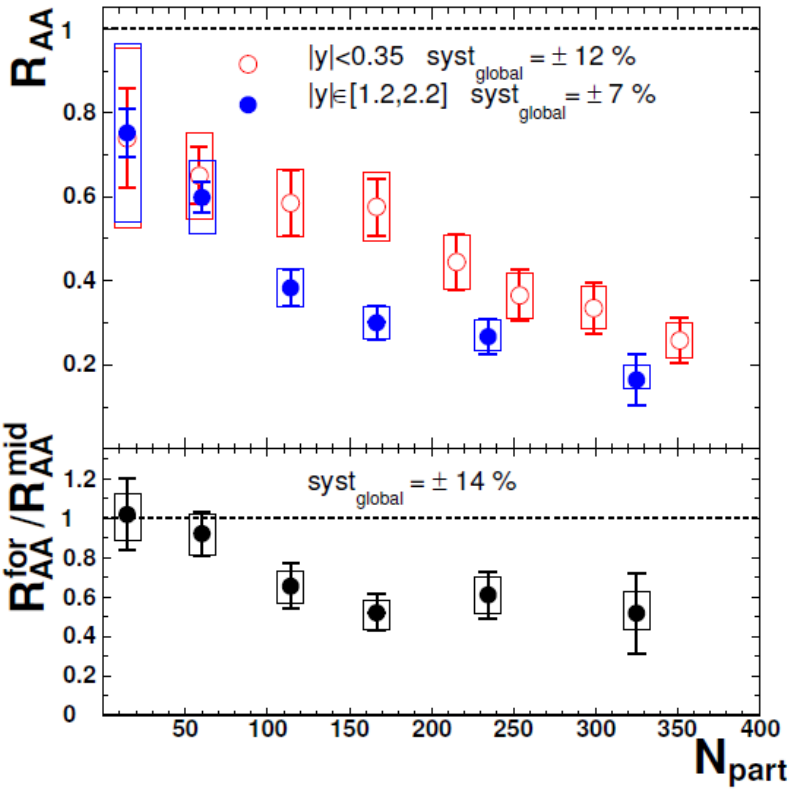

Figure 1.12: The nuclear modification factor $R_{AA}^{J/\psi}$ as a function of $N_{\rm part}$ in Au–Au collisions observed by PHENIX collaboration for $|y| < 0.35$ and $1.2 < |y| < 2.2$ [31].

going. In order to estimate the CNM contribution to the nuclear modification factor $R_{AA}^{J/\psi}$ in Au–Au collisions, the d-Au collisions have been utilized [32].

1.5 Production mechanisms of heavy quarkonia

The production of heavy quarkonia in nucleon-nucleon collisions at high energies, so-called hadroproduction, has not been well explained and predicted. It is known that the production process of heavy quarkonium can be understood in two steps:

- the creation of heavy quark pair, $Q\bar{Q}$ after the nucleon-nucleon colli-

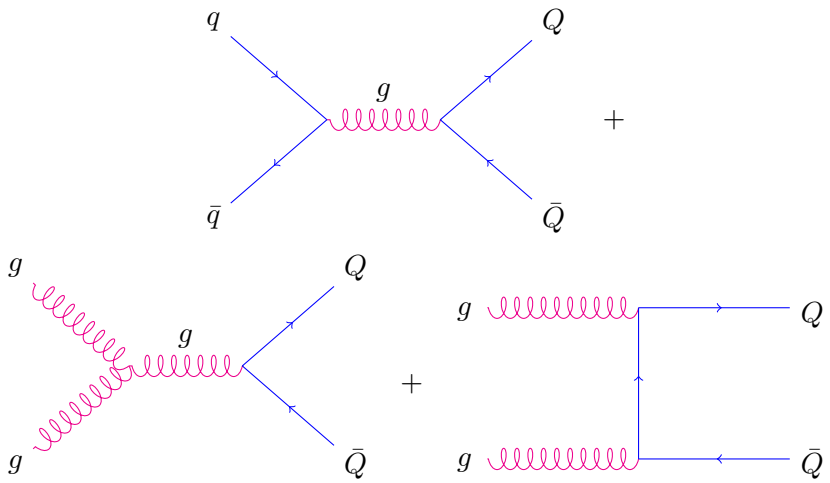

Figure 1.13: The leading-order QCD processes.

sions,

- and the subsequent evolution of the $Q\bar{Q}$ pair to form the quarkonium.

The first step, the creation of $Q\bar{Q}$ pair, occurs at short-distance which can be calculable in perturbation theory. The leading-order QCD processes are: quark and anti-quark pair annihilation and gluon-gluon fusion (see Fig. 1.13). The second step involves the long-distance scales that is non-perturbative transition. The formation of the heavy quarkonium state should be independent of the details of the heavy quark pair creation. Therefore, it is natural to factorize the heavy quarkonium production into the short-distance part and the long-distance effect, which is called "factorization".

The different treatments of the non-perturbative evolution (long-distance effect) of the $Q\bar{Q}$ pair transformation into a quarkonium have led to various theoretical models in describing the heavy quarkonium production mechanism. The Color Singlet Model (CSM), the Color Evaporation Model (CEM), and the Non-Relativistic QCD (NRQCD) approach are the most notable among them.

The CSM [33] was first proposed shortly after the discovery of the J/ψ. It is assumed that the $Q\bar{Q}$ pair that evolves into the heavy quarkonium is in a color singlet state and the quantum numbers, in particular, spin and an-

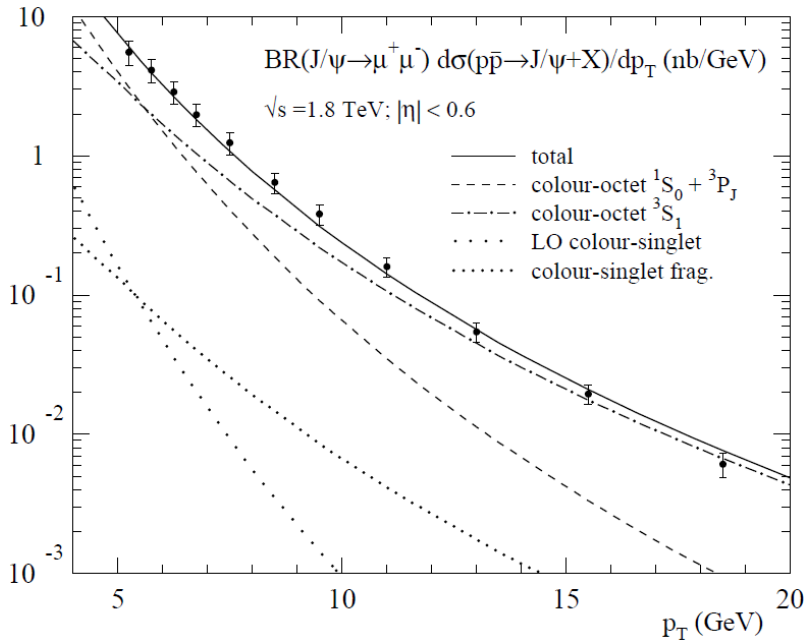

Figure 1.14: Comparison between preliminary measurements from CDF for J/ψ and the various models, CSM (dotted curves), CEM (dashed curves), and NRQCD (solid curves) [21]. The CSM fragmentation contribution is also shown [36].

gular momentum of $Q\bar{Q}$ pair are conserved after the formation of the heavy quarkonium. The CSM was successful in predicting heavy quarkonium production rates at relatively low energy [34]. However, it failed to describe the data for charmonium measured by CDF collaboration in $p\bar{p}$ collisions. The experimental measurement showed large discrepancy between the data and the CSM prediction by more than one order of magnitude [35] as shown in Fig. 1.14. It was pointed out that the CSM ignored the fragmentation processes from a higher state quarkonium or B meson that is dominant at high energies, such as the Tevatron energies ($\sqrt{s} = 1.8$ TeV) [37]. Recently, the CSM with corrections at next-to-leading order (NLO) and next-to-next-to-leading order (NNLO) gives a prediction close to the $\Upsilon(1S)$ production cross section [38] (see Fig. 1.15).

The CEM was initially introduced in 1977 [39] and was revived in 1996 [40] after the failure of the CSM. In the CEM, the production rate for the heavy

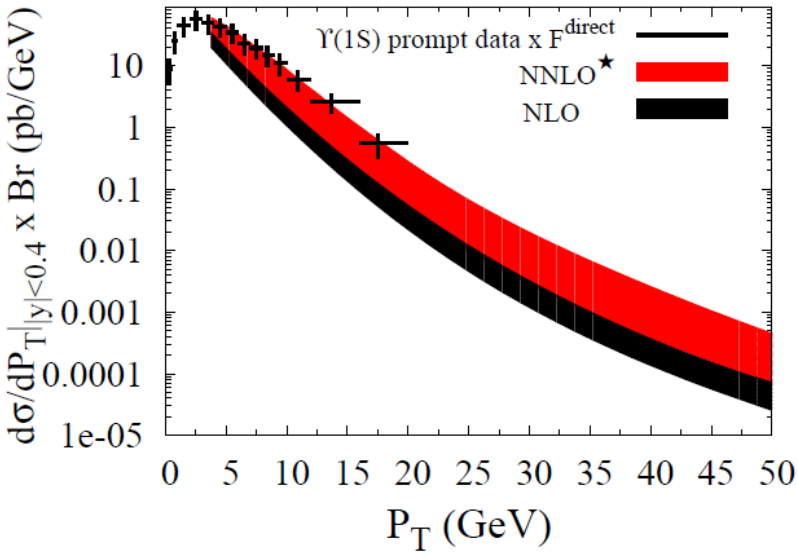

Figure 1.15: p_{t} dependence of $\Upsilon(1S)$ production cross section measured by CDF and the comparison with CSM NLO and NNLO* [38].

quarkonium state is treated as some fraction of the cross section for producing $Q\bar{Q}$ pairs with the mass below the lowest charm or bottom meson. That is, the cross section of the heavy quarkonium state is limited by the $Q\bar{Q}$ pair mass. In the model, it is assumed that the $Q\bar{Q}$ pair neutralizes its color by interaction with the collision induced color field, that is, by "color evaporation", and this color field randomizes the spin of the $Q\bar{Q}$ pair. The latter assumption leads to the prediction that the quarkonium production rate is independent of the quarkonium spin that is contradicted by the measurements of non-zero polarization of the quarkonium states. The CEM predictions were fit to the CDF measurement for charmonium states production including P-wave states, χ_c, but showed poor result [41, 42] (see Fig. 1.14).

The Non-Relativistic QCD is an effective field theory of QCD [43] which reproduces accurately full QCD at momentum scales order $1/m_Q v$ or larger. Within the framework of NRQCD, the cross section for the production of a quarkonium state H can be written as a sum of terms, each of which factors into a short distance partonic cross section and a long distance matrix

element:

$$\mathrm{d}\sigma(H+X) = \sum_n \mathrm{d}\hat{\sigma}(Q\bar{Q}[n]+X)\langle \mathcal{O}^H[n]\rangle.$$

The sum includes all color and angular momentum states of the $Q\bar{Q}$ pair, denoted collectively by n: color singlet or color octet. The short distance coefficients $\mathrm{d}\hat{\sigma}$ are proportional to the cross sections for production of a $Q\bar{Q}$ pair in the state n and with small relative momentum which can be calculated in perturbation theory. The non-perturbative transition probabilities from the $Q\bar{Q}$ state n into the quarkonium H are given by the vacuum expectation values of operators in NRQCD. The NRQCD can reproduce the cross section of charmonium production in $\mathrm{p\bar{p}}$ collisions at Tevatron energies, $\sqrt{s} = 1.8$ TeV (see Fig. 1.14), however, it failed to describe the polarization of heavy quarkonium as shown in Fig. 1.16.

As we have seen, the mechanism of the hadroproduction of heavy quarkonium is still an open question. The efforts for establishing the theory of the heavy quarkonium production in hadronic collisions have been continued and its completion will help us to understand the phenomena expected in the medium created in heavy-ion collisions.

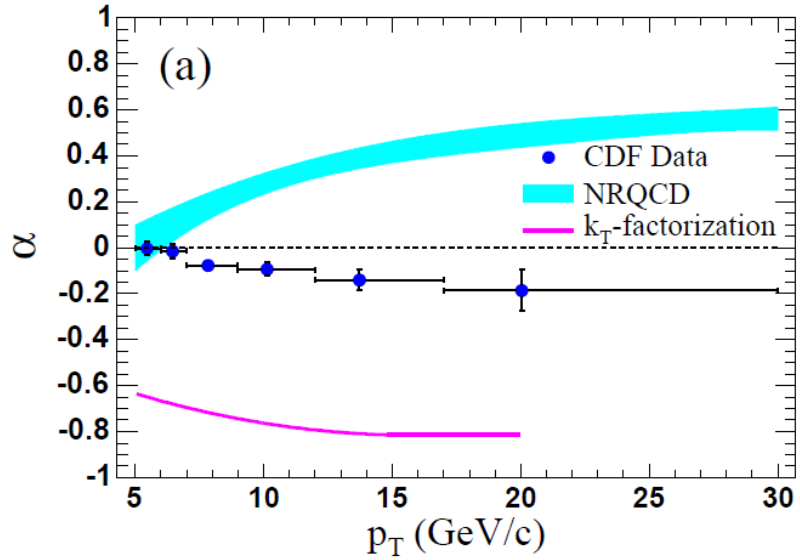

(a)

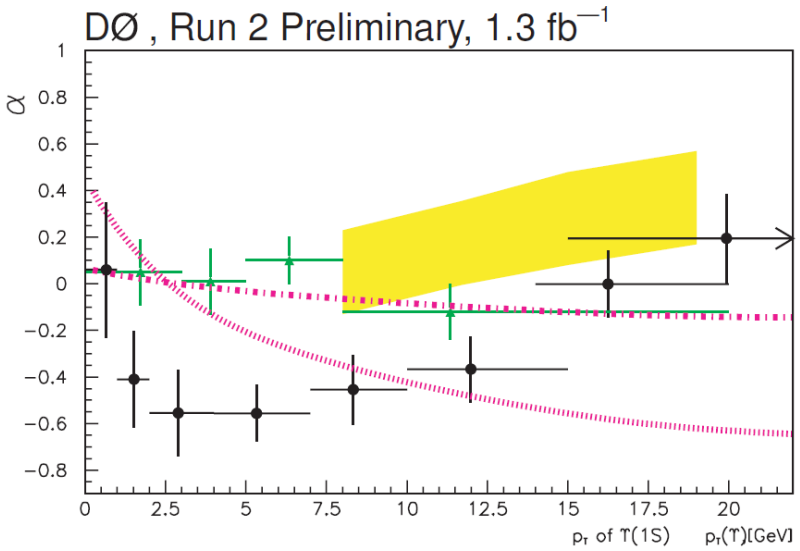

(b)

Figure 1.16: (a) Polarization of prompt J/ψ as a function of p_t measured by CDF (blue points with black error bars). The blue band (magenta line) is the prediction from NRQCD [44] (the k_T factorization model [45]). (b) Polarization of inclusive $\Upsilon(1S)$ as functions of p_t measured by CDF (green) and D0 (black). The yellow band (magenta curves) is the prediction from NRQCD [46] (the k_T factorization model [45]).

Chapter 2

ALICE Detectors

ALICE [47] is a general-purpose particle detector to study the physics phenomena that can arise in heavy-ion collisions as well as in proton-proton collisions at CERN LHC. The crucial requirement of its design is to be optimized to track and identify particles in an environment with very high charged-particle multiplicities created in the central heavy-ion collisions, up to 8,000 charged particles per rapidity unit at mid-rapidity[1]. ALICE has been built by an international collaboration including currently over 1,000 members from 116 institutes in 33 countries.

The unique features of the ALICE detector are the tracking and particle identification over a wide range of momenta, from the very low (∼100 MeV/c) transverse momentum, p_{t}, up to high (∼100 GeV/c) p_{t}, therefore it is feasible to reconstruct short-lived particles such as hyperons[2], D and B mesons. Its layout, shown in Fig. 2.1, consists of a central detector system ($|\eta| \leqslant 0.9$) seated in a magnetic field of 0.5 T and several additional detectors at the large rapidity region. The central system is optimized to track and identify hadrons, electrons and photons, and the forward detectors complement the rapidity coverage of the central detectors (up to $\eta = 5.1$) and provide the interaction trigger, and the detection and identification of muons as well.

[1] Upper value was predicted at the moment of the design

[2] Any baryon containing one or more strange quarks, but no charm or bottom quark

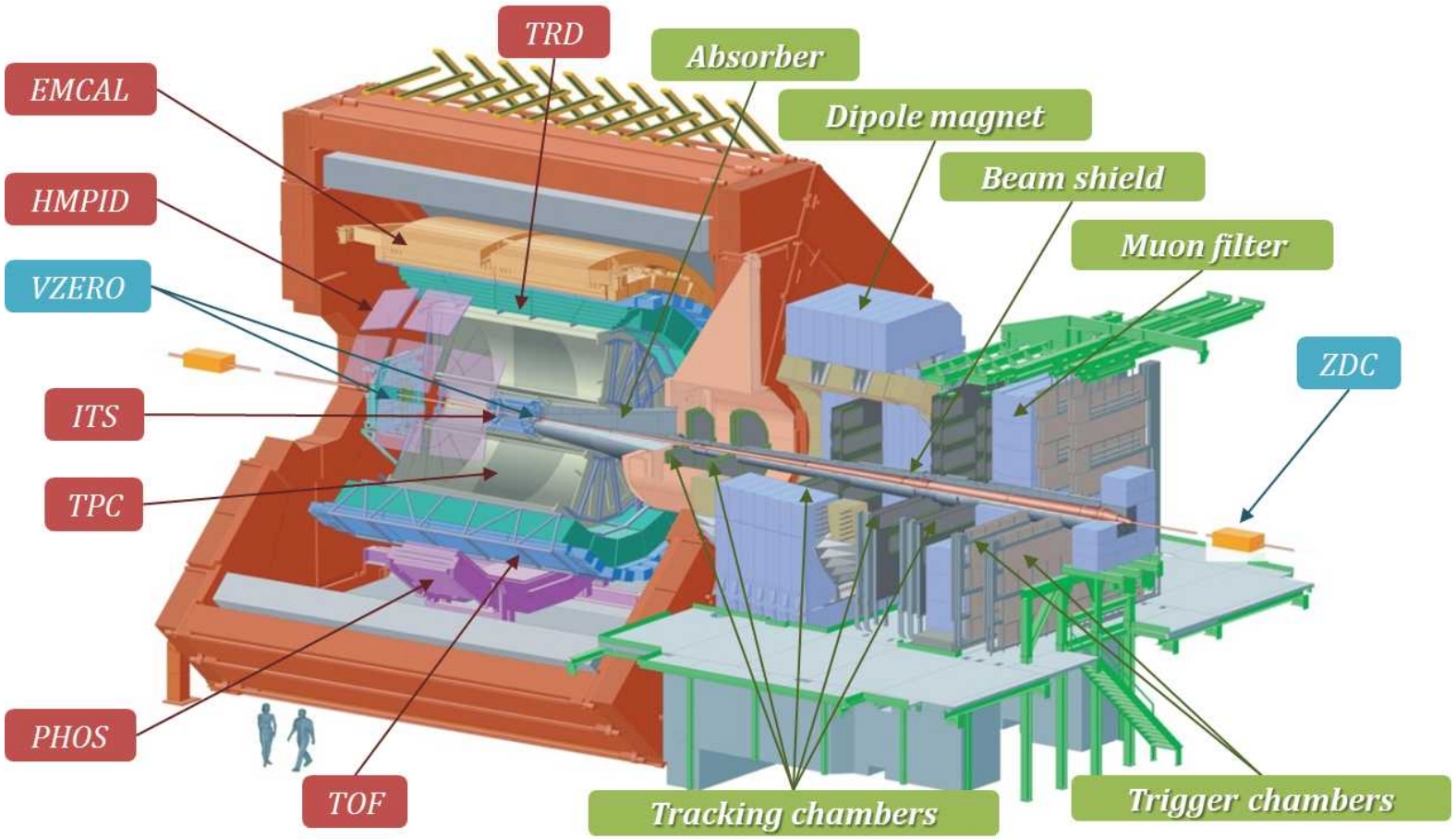

Figure 2.1: A schematic 3D view of the ALICE detector [47].

2.1 Central Detectors

The central system, covering mid-rapidity ($|\eta| \leqslant 0.9$) over the full azimuth, is installed inside a large solenoidal magnet constructed for the L3 experiment at LEP [48]. The nominal field of the solenoid is 0.5 T. The central system includes, from the interaction point to the outside (with full azimuthal coverage): the Inner Tracking System (ITS), the Time-Projection Chamber (TPC), the Transition-Radiation Detector (TRD), and the Time-Of-Flight (TOF). Tracking and particle identification in the central region depend on these four detectors. There are additional central detectors covering smaller acceptance than those mentioned above: High-Momentum Particle Identification Detector (HMPID), Photon Spectrometer (PHOS), Electromagnetic Calorimeter (EMCal) and the ALICE Cosmic Ray Detector (ACORDE). The detector parameters of the central detectors are summarized in Tab. 2.1.

2.1.1 Inner Tracking System

ITS [49] is designed to localize a primary vertex with a resolution better than 100 μm, so that we can reconstruct secondary vertices from the decays of hyperons, D and B mesons, and to track and identify low momentum particles ($<$ 200 MeV/c) in order to improve the momentum and angular resolution for particles reconstructed by TPC and to reconstruct particles traversing dead regions of TPC.

The ITS surrounds the Interaction Point (IP)[3] as well as the beam pipe and consists of six cylindrical layers of silicon detectors, as shown schematically in Fig. 2.2. It covers the rapidity range of $|\eta| < 0.9$. The first layer has an extended coverage ($|\eta| < 1.98$) to provide a continuous rapidity coverage for the measurement of charged-particle multiplicity together with the Forward Multiplicity Detectors (FMD). It consists of Silicon Pixel Detectors (SPD) and Silicon Drift Detectors (SDD) for the innermost four layers, and double-sided Silicon micro-Strip Detectors (SSD) for the outermost two layers. Except SPD, all the layers, SDD and SSD, identify particles via $\mathrm{d}E/\mathrm{d}x$ measurement in the low momentum region. This gives ITS a stand-alone

[3] where the collisions occur.

Table 2.1: A summary of the detector parameters of the central detectors.

Detector	$\|\eta\|$ coverage	$\Delta\phi$ coverage	Radial position (cm)	Read-out channels	purpose
ITS	0.9 (1.98)	360°	$3.9 < r < 48.9$	1.26×10^7	localize vertex
TPC	0.9 (1.5)	360°	$84.8 < r < 246.6$	5.57×10^5	track reconstruction
TRD	0.84	360°	$290 < r < 368$	1.18×10^6	electron PID
TOF	0.9	360°	$370 < r < 399$	1.57×10^5	hadron PID
HMPID	0.6	57.6°	500	1.61×10^5	hadron PID ($p_{\mathrm{t}} > 1$ GeV/c)
PHOS	0.12	110°	460	8.96×10^4	photon PID
EMCal	0.7	107°	450	2.53×10^4	jet physics
ACORDE	1.3	120°	850	120	cosmic ray study

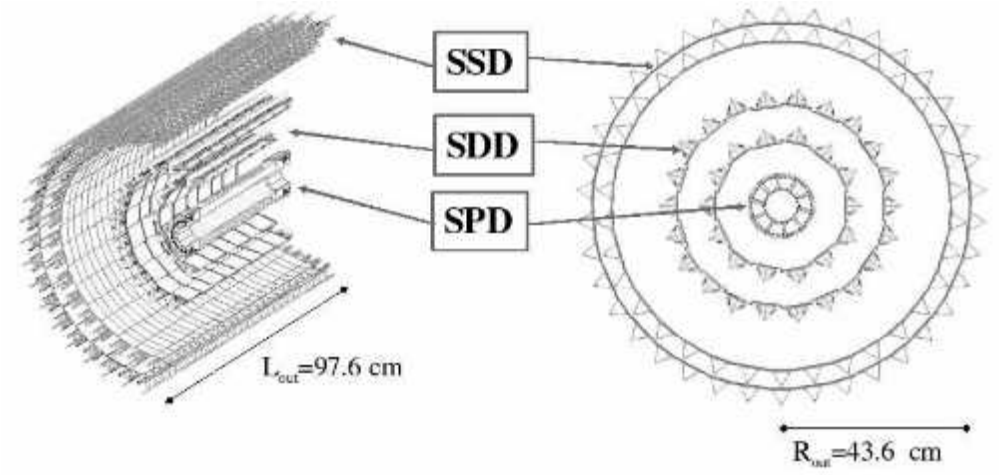

Figure 2.2: Layout of Inner Tracking System.

capability as a low-p_{t} particle spectrometer.

ITS detectors provide a resolution on the impact-parameter measurement adequate for heavy-flavored particle detection (better than 60 μm for $p_{\mathrm{t}}>$ 1 GeV/c). The measurement of open charm and open beauty produced in the collisions can be possible together with TRD. A similar technique can be used to separate directly produced J/ψ mesons from those produced in B-decays.

In particular, SPD plays a crucial role of triggering the minimum bias event in proton-proton collisions and Pb–Pb collisions with V0 (some details about V0 detector are described in Section 2.2.4).

2.1.2 Time-Projection Chamber

TPC [50] is the main tracking detector of the central barrel consisting of multi-wire proportional chambers and is cylindrical in shape with an inner radius of about 80 cm, an outer radius of about 250 cm, and an overall length in the beam direction of 500 cm. The TPC 3D-layout of the field cage is shown in Fig. 2.3.

The information provided by this detector, together with the other central barrel detectors, ITS, TRD and TOF, allows to measure charged-particle

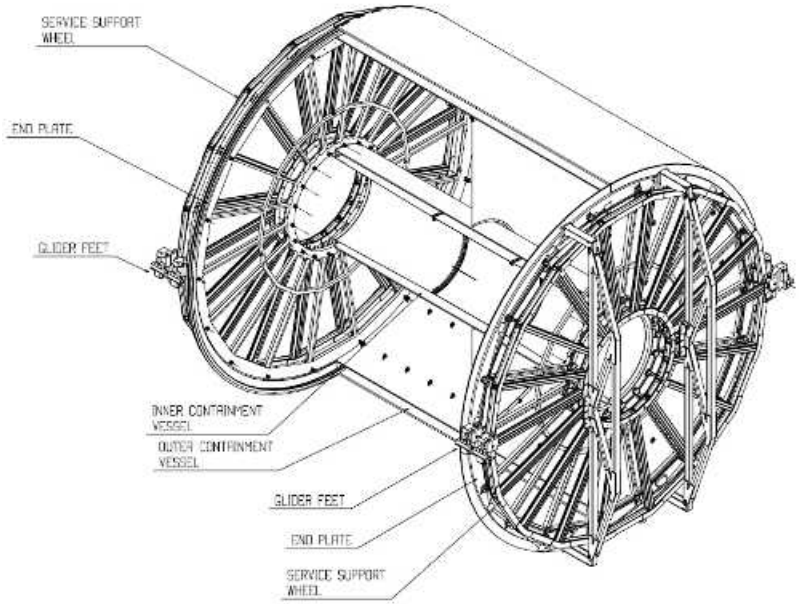

Figure 2.3: A 3D view of TPC field cage and service support wheels.

momenta, particle identification via $\mathrm{d}E/\mathrm{d}x$ (see Fig. 2.4), and vertex determination with sufficient momentum resolution and good track separation. The phase space covered by TPC in pseudo-rapidity is $|\eta|< 0.9$ for tracks with full radial track length; up to $|\eta| = 1.5$ for reduced track length (at innermost radius). A large p_{t} range is covered from low p_{t} of about 0.1 GeV/c up to 100 GeV/c with good momentum resolution.

The maximum occupancies of TPC are about 40% at the innermost radius; 15% at the outermost radius for an extreme charge particle multiplicity density of $\mathrm{d}N_{ch}/\mathrm{d}\eta = 8{,}000$ in Pb–Pb collisions that leads to the corresponding interaction rates of up to 200 Hz. In pp collision runs, due to the drift time ~ 90 μs, at a pp luminosity of about 5×10^{30} cm^{-2}s^{-1}, the corresponding interaction rate is limited of about 350 kHz.

2.1.3 Transition-Radiation Detector

The main purpose of TRD [51] is to provide electron identification in the central barrel for momenta above 1 GeV/c. Below this momentum electrons can be identified via specific energy loss measurement in TPC. Above 1

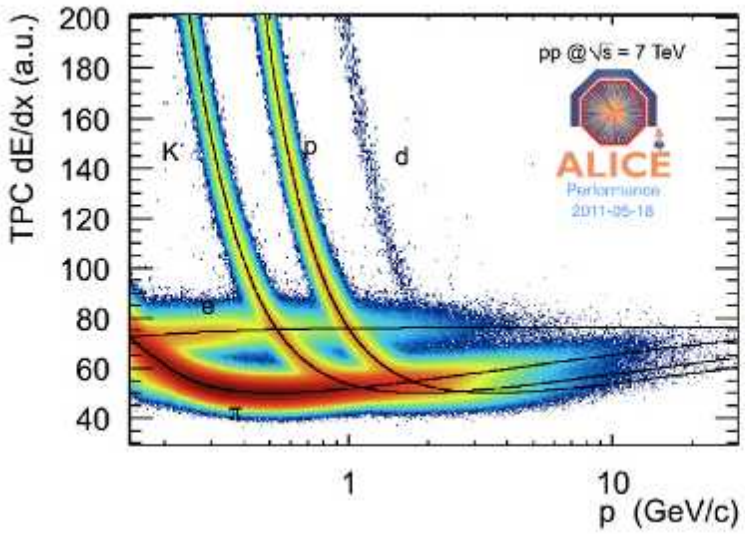

Figure 2.4: A $\mathrm{d}E/\mathrm{d}x$ spectrum versus momentum of TPC in pp collisions at $\sqrt{s} = 7$ TeV. The lines are a parameterization of the Bethe-Bloch curve.

GeV/c transition radiation from electrons passing a radiator can be exploited to obtain the necessary pion rejection capability. In conjunction with data from ITS and TPC it is possible to measure the production of light and heavy vector-meson resonances and the di-lepton continuum both in pp as well as in Pb–Pb collisions.

The TRD is designed to derive a fast trigger for charged particles with high momentum. It is part of the Level 1 trigger and can significantly enhance the recorded Υ-yields and high-p_{t} J/ψ in the di-electron mass spectrum. The mass resolution of about 100 MeV/c^2 for Υ measurement, the expected momentum resolution of 3.5 (4.7)% at 5 GeV/c (depending on multiplicity). The maximum occupancy is 34% at the highest simulated multiplicity density of $\mathrm{d}N_{ch}/\mathrm{d}\eta$ = 8,000 including secondary particles. The layout of TRD is depicted in Fig. 2.5.

2.1.4 Time-Of-Flight Detector

TOF [52] detector is a large array equipped with the Multi(10)-gap Resistive Plate Chamber (MRPC) [53] for particle identification (PID) in the interme-

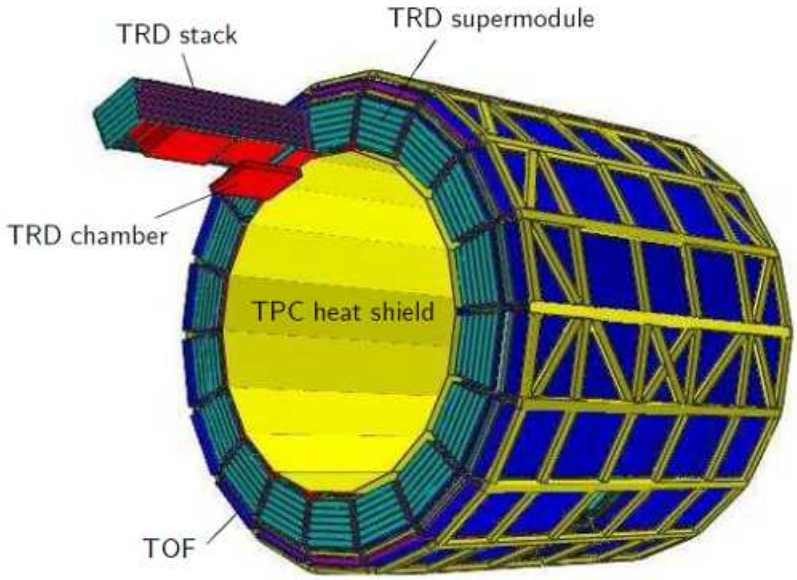

Figure 2.5: A schematic 3D drawing of TRD layout in the ALICE space frame.

diate momentum range, below about 2.5 GeV/c for pions and kaons, up to 4 GeV/c for protons, with a good π, K and proton separation (see Fig. 2.6).

The rapidity coverage is $|\eta| < 0.9$ and the maximum occupancy for Pb–Pb, is not exceeding the 10-15% level at the high charged-particle density of $\mathrm{d}N_{ch}/\mathrm{d}\eta$ = 8,000. The time resolution provided by the MRPC is better than about 40 ps with an efficiency $\sim$ 100%. A schematic layout of one super-module inside the ALICE space frame is shown in Fig. 2.7.

2.1.5 High-Momentum Particle Identification Detector

HMPID [54], based on Ring Imaging Cherenkov (RICH) counters [55], provides hadron identification with $p_{\mathrm{t}} > 1$ GeV/c. The aim is to enhance the PID capability of ALICE by enabling identification of charged hadrons beyond ITS and TPC ($\mathrm{d}E/\mathrm{d}x$) and TOF. The detector was optimized to extend the useful range for π/K and K/p discrimination up to 3 GeV/c and 5 GeV/c, respectively. It was designed as a single-arm array in azimuthal coverage $1.2^\circ < \phi < 58.8^\circ$ results in the acceptance of 5% in phase space.

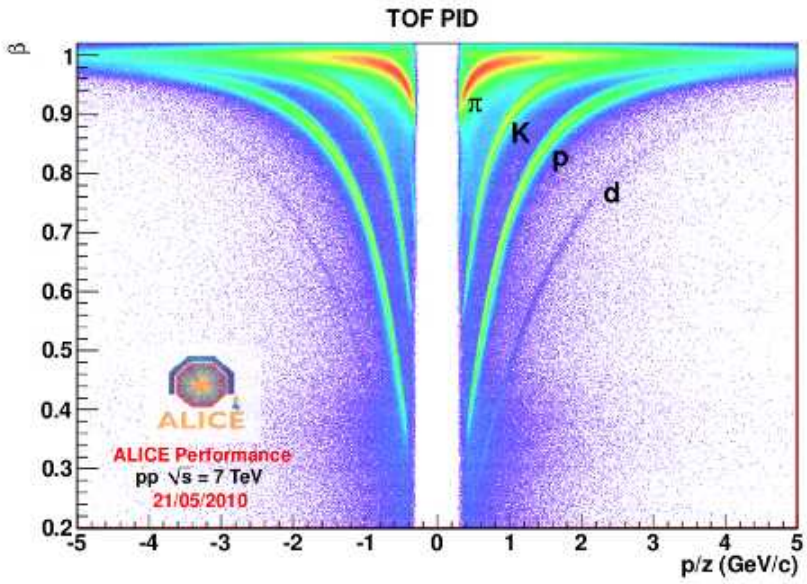

Figure 2.6: Particle identification of TOF via measured particle $\beta(= v/c)$ versus momentum in pp collisions at $\sqrt{s} = 7$ TeV.

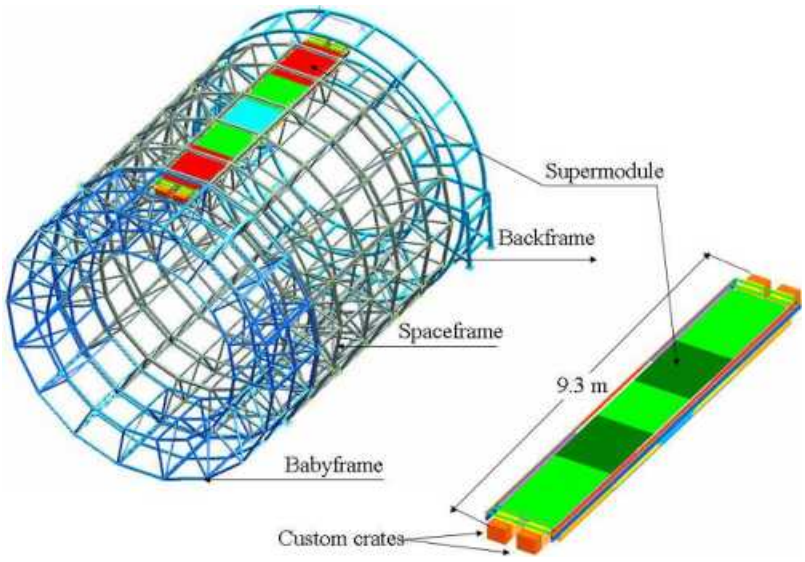

Figure 2.7: A schematic drawing of one TOF super-module in the ALICE space frame.

Figure 2.8: View of modules of HMPID mounted on the cradle.

The picture of HMPID is shown in Fig. 2.8.

2.1.6 Photon Spectrometer

PHOS [56] is designed to detect and identify photons consisting of electromagnetic calorimeter and a Charged-Particle Veto (CPV) detector. The rapidity coverage is $|\eta| < 0.12$ and the azimuthal coverage is $220^\circ < \phi < 320^\circ$. It is positioned on the bottom of the ALICE setup at a distance of 460 cm from the interaction point. The layout of PHOS is shown in Fig. 2.9. The two-photon invariant mass resolution of PHOS at the π^0 peak is 3.5% and the achieved timing resolution is about 2 ns.

2.1.7 Electromagnetic Calorimeter

EMCal [57] is a large Pb-scintillator sampling calorimeter with cylindrical geometry, located adjacent to the ALICE magnet coil at a radius of $\sim$ 4.5 meters from the beam line. It covers $|\eta| \leq 0.7$ and $\Delta\phi = 107^o$, and is positioned approximately opposite in azimuth to the PHOS. The integration layout of EMCal is shown in Fig. 2.10.

The detector increases the electromagnetic calorimeter coverage and en-

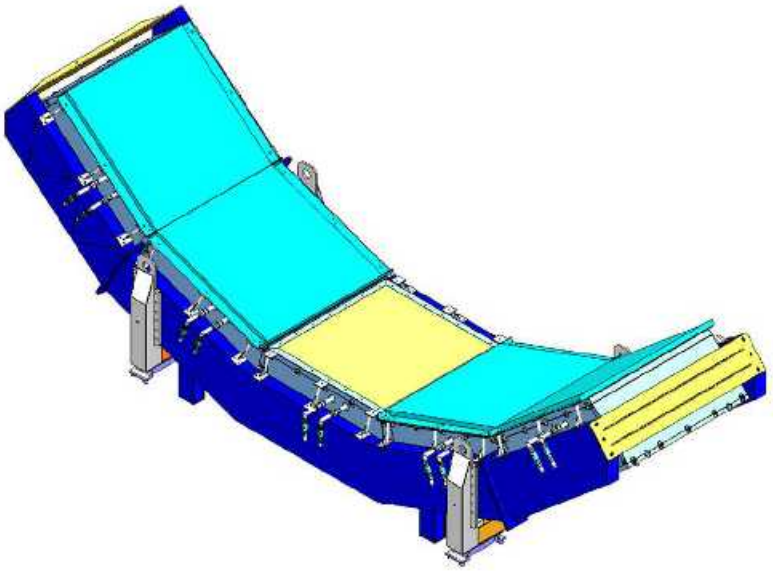

Figure 2.9: View of modules of PHOS.

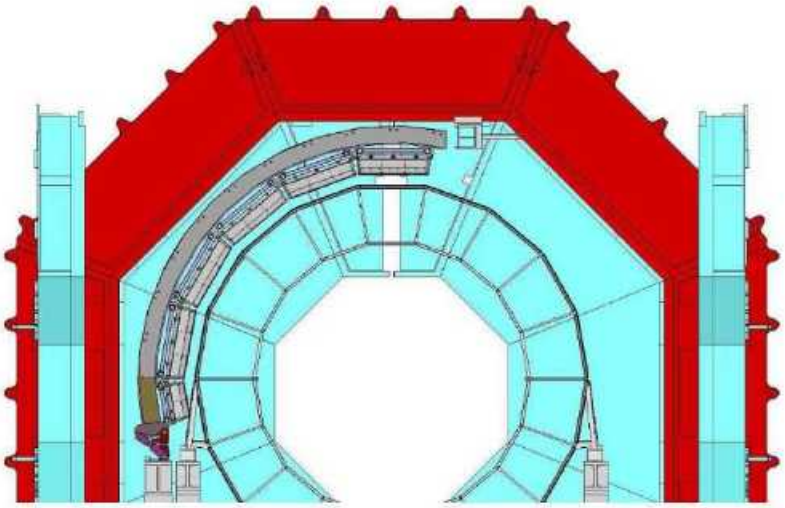

Figure 2.10: Schematic integration drawing of the end view of the ALICE central barrel.

Figure 2.11: Photograph of ACORDE scintillator modules on the upper faces of the magnet yoke of ALICE.

hances the capability of jet physics. It provides a trigger for hard jets, photons and electrons. It also measures the neutral energy component of jets, enabling full jet reconstruction both in pp and Pb–Pb collisions.

2.1.8 ALICE Cosmic Ray Detector

ACORDE [58] consists of scintillator counters and is placed on the upper surface of the L3 magnet (see Fig. 2.11). It provides a Level 0 trigger signal for the commissioning, calibration and alignment of the tracking detectors. It is designed to detect single atmospheric muons and multi-muon events (so-called muon bundles) and to study high-energy cosmic rays in combination with TPC, TRD and TOF.

2.2 Forward Detectors

The large rapidity systems include Muon Spectrometer (a detailed discussion of this detector is provided in the next section), Photon Multiplicity Detec-

tor (PMD), and Forward Multiplicity Detector (FMD) covering the rapidity region up to $\eta = 5.1$ (see Fig. 2.12). T0 and V0 will provide fast trigger signals and Zero-Degree Calorimeter (ZDC) will measure the nucleus-nucleus centrality together with V0 (see Fig. 2.13). The detector parameters of the forward detectors are summarized in Tab. 2.2.

2.2.1 Zero Degree Calorimeter

ZDC [62] provides the estimation of the number of participant nucleons related to the geometry of Pb–Pb collisions by measuring the energy carried in the forward direction (at 0° relative to the beam direction) by non-interacting nucleons.

The detector consists of two hadronic ZDCs (ZN for neutron and ZP for proton) located at 116 m on either side of the IP and two small electromagnetic calorimeters (ZEM) placed at about 7 m from the IP on both sides of the LHC beam pipe, opposite to the muon arm (see Fig. 2.14). The ZEM complement the hadronic ZDCs to distinguish two classes of events: the central events with small number of spectators; and the very peripheral events.

2.2.2 Photon Multiplicity Detector

PMD [63] measures the multiplicity and spatial distribution (in $\eta - \phi$ plane) of photons in the pseudo-rapidity region of $2.3 < \eta < 3.7$. These measurements provide estimations of transverse electromagnetic energy and the reaction plane on an event-by-event basis.

2.2.3 Forward Multiplicity Detector

FMD [64] is to provide charged-particle multiplicity information in the pseudo-rapidity range $-3.4 < \eta < -1.7$ and $1.7 < \eta < 5.0$. It helps to increase the pseudo-rapidity coverage of ALICE together with SPD layers: $-3.4 < \eta < 5.0$ (see Fig. 2.12). FMD2 and FMD3 each consist of both an inner and an outer ring of silicon sensors and are located on either side of ITS detector. FMD1 is placed further from the IP opposite to the muon spectrometer to extend the charged particle multiplicity coverage. The layout of FMD is shown in

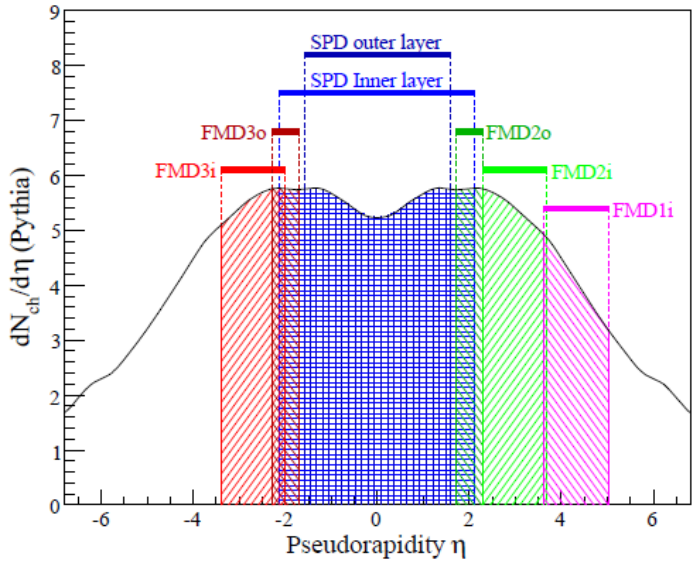

(a)

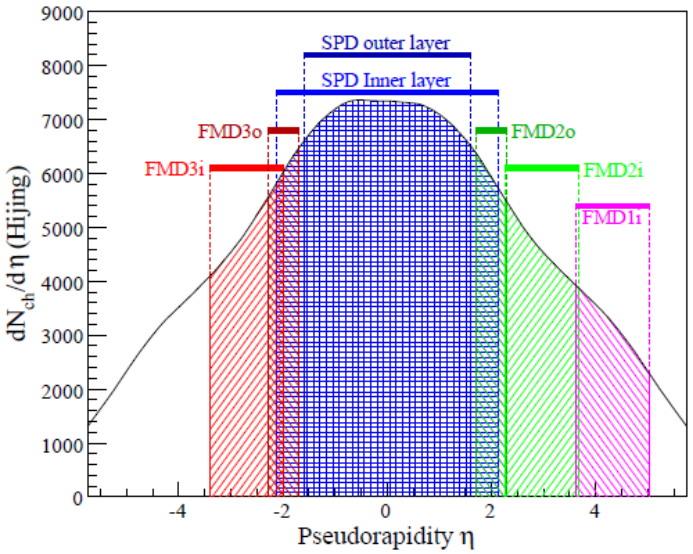

(b)

Figure 2.12: Simulated pseudo-rapidity coverage of FMD rings (1 inner, 2 inner and outer, and 3 inner and outer) along with two SPD layers. The multiplicity distribution is produced by (a) PYTHIA [59] in pp collisions at $\sqrt{s} = 14$ TeV; (b) HIJING [60, 61] in Pb–Pb collisions at $\sqrt{s_{\mathrm{NN}}} = 5.5$ TeV.

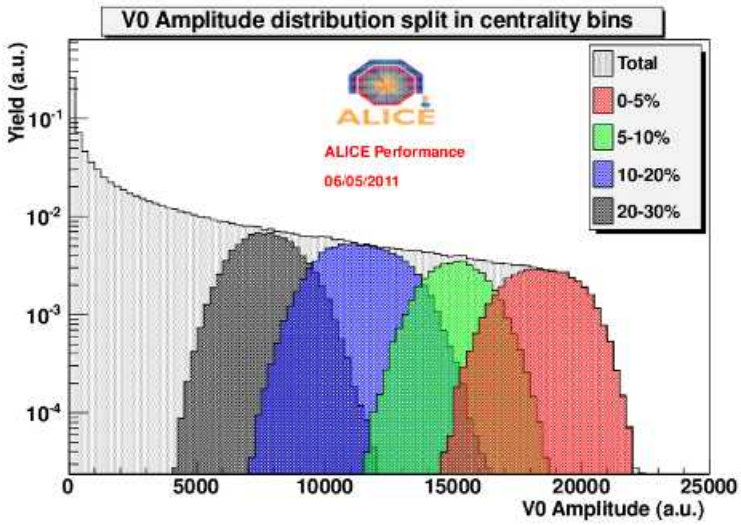

Figure 2.13: V0 amplitude distribution split in event centralities determined by ZDC: 0-5%, 5-10%, 10-20%, and 20-30%.

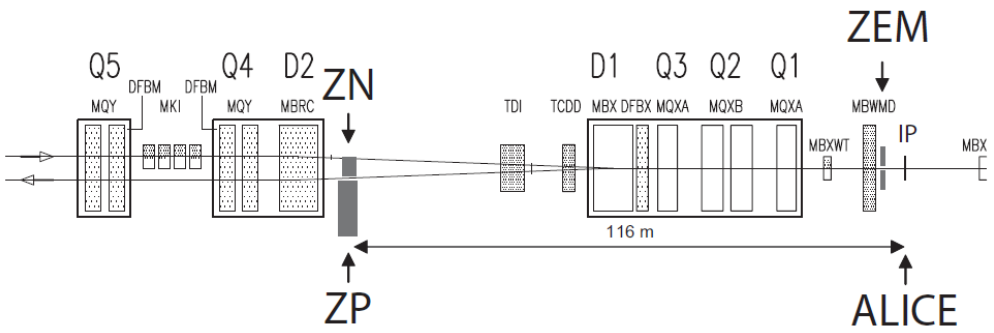

Figure 2.14: Schematic top view of the side of ALICE beam line opposite to the muon arm. The locations of the neutron (ZN), proton (ZP) and electromagnetic calorimeters (ZEM) are shown.

Table 2.2: A summary of the detector parameters of the forward detectors.

Detector	η coverage	Longitudinal position (m)	Read-out channels	purpose
ZDC	$\sim\infty(0^\circ)$	7 (116)	11	N_{part} estimation & event centrality
PMD	$2.3 \leq \eta \leq 3.7$	3.64	2.21×10^5	photon multiplicity & spatial distribution
FMD	$-3.4 < \eta < -1.7$, $1.7 < \eta < 5.0$	3.2 (FMD1), $7.52 < z < 8.34$ (FMD2), $-7.52 < z < -6.28$ (FMD3)	5.12×10^5	charged particle multiplicity
V0	$2.8 < \eta < 5.1$ (V0A), $-3.7 < \eta < -1.7$ (V0C)	3.4 (V0A), 0.9 (V0C)	64	(μ-)MB trigger & event centrality
T0	$4.61 \leq \eta \leq 4.92$ (T0A), $-3.28 \leq \eta \leq -2.97$ (T0C)	3.75 (T0A), -0.7 (T0C)	24	start time (T0) & vertex position

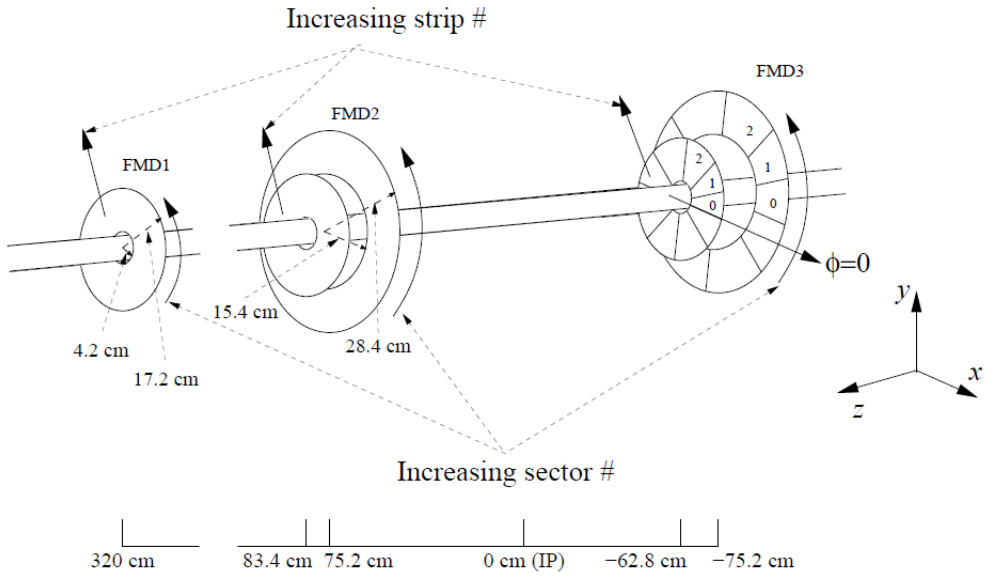

Figure 2.15: Layout of FMD rings. FMD3 and FMD2 are located on each side of ITS; FMD1 is much further away from IP.

Fig. 2.15.

2.2.4 V0 Detector

V0 detector [64] provides:

- minimum-bias triggers both in pp and Pb–Pb collisions;
- an indicator of the centrality of the collision via the multiplicity recorded in the event [65] together with ZDC (see Fig. 2.13);
- a trigger of the interaction of protons with the residual gas of the vacuum chamber which can help to eliminate false events [66];
- a good signal to reject a large part of the false muon triggers with the absence of minimum-bias trigger from V0C alone [67].

It also participates in the measurement of luminosity in pp collisions with a good precision of about 10% [68].

It consists of two arrays of scintillator counters, called V0A and V0C, which are installed on either side of the ALICE IP at a small angle. The

V0A detector is located 340 cm from the IP on the side opposite to the muon spectrometer whereas V0C is fixed to the front face of the hadronic absorber, 90 cm from the IP. They cover the pseudo-rapidity ranges 2.8 < η < 5.1 (V0A) and -3.7 < η < -1.7 (V0C).

2.2.5 T0 Detector

T0 detector [64] is designed to:

- generate a start time (T0) for TOF detector;
- measure the vertex position (with a precision $\pm$1.5 cm) for each interaction;
- provide a L0 trigger when the position is within the preset values that can help discriminate against beam-gas interactions.

It can also generate so-called *wake-up* signal to TRD, prior to L0.

T0C, one of the arrays, is placed 72.7 cm from the IP and covers the pseudo-rapidity range $-3.28 \leq \eta \leq -2.97$. T0A, the other of the arrays covering the pseudo-rapidity range of $4.61 \leq \eta \leq 4.92$, is located 375 cm on the opposite side of the IP grouping together with FMD, V0 and PMD (see Fig. 2.16).

2.3 Muon Spectrometer

Muon spectrometer [69, 70, 71] is designed to detect and identify muons in the pseudo-rapidity range $-4.0 < \eta < -2.5$. It is feasible to measure the whole spectrum of heavy quark meson resonances, such as charmonia (J/ψ, ψ') and bottomonia (Υ family) as well as low mass vector mesons (ϕ, ρ) in their $\mu^+\mu^-$ decay channel. In addition to vector mesons, it is available to study the production of the open (heavy) flavors (charm and beauty) with this detector at LHC energy in which the semi-leptonic decay is dominant.

The layout of the muon spectrometer is shown in Fig. 2.17. It consists of a set of absorbers, a warm dipole magnet, 10 tracking chambers and 2

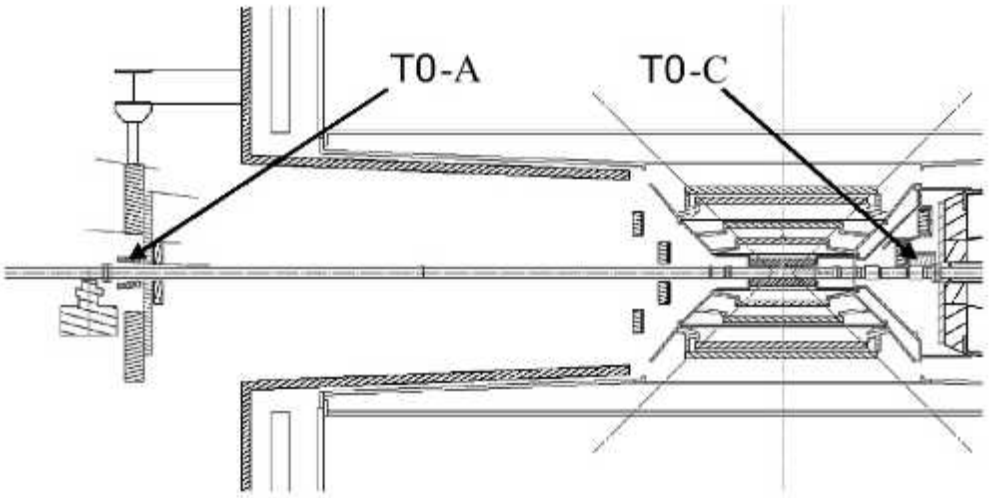

Figure 2.16: Layout of T0 detectors.

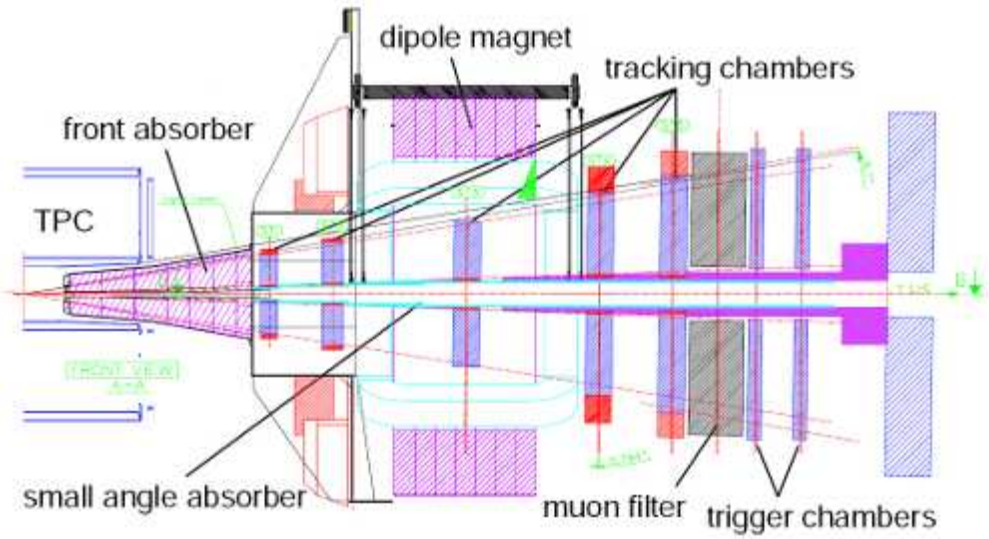

Figure 2.17: Muon spectrometer longitudinal section

(a) (b)

Figure 2.18: (a) Graphite and (b) steel envelope for the front absorber

trigger stations. In order to reduce the flux of hadrons in the heavy-ion environment, the large amount of absorber material is required, and thus muons with the momenta above 4 GeV/c are only detectable in the muon spectrometer. However, measurement of charmonia with p_{t} down to 0 is possible since the muon spectrometer is located at large rapidity region where muons are Lorentz boosted. For Υ measurement, the required mass resolution is 100 MeV/c^2 to resolve the Υ resonances. This requirement determined the bending strength of the warm dipole magnet ($\sim$ 3 Tm) as well as the spatial resolution of the tracking chambers ($\sim$ 70 μm). The tracking chambers are designed to handle the high multiplicity environment expected in heavy-ion collision with a high granularity read-out ($\sim 1 \times 10^6$ channels). The trigger system has a selective feature for single- and di-muon to achieve the maximum trigger rate ($\sim$ 1 kHz).

2.3.1 Absorbers and dipole magnet

Front absorber

The front absorber is located at 90 cm from the IP inside the solenoid L3 magnet. Its length is 4.13 m. The volume of the absorber is made out of carbon, concrete and steel having a conical geometry, see Fig. 2.18. It is designed to limit multiple scattering and energy loss by traversing muons,

but also to protect other ALICE detectors from secondaries produced within the absorbing material itself [72]. For this, It is covered by a 10 mm layer of tungsten at the front end of the cone (close to ITS) and in the sector between 10.5° and 12.5° where faces TPC. A tungsten cover of 100 mm thickness at the back end absorbs most of the low energetic electrons created inside the absorber. An additional ring of 100 mm of tungsten is added to the 2° cone to improve the shielding against particles from the beam pipe.

Beam shield

A tube made out of tungsten, lead and steel surrounds the beam pipe to reduce background particles emerging from the beam pipe. It forms a cone with an opening angle of 2° close to the IP while a cylinder of 58 cm diameter at 5.5 m from the IP. The length of the beam shield is ~ 18 m.

Muon filter

An iron wall of 1.2 m thickness is located in front of the first trigger chamber (about 15 m distance from the IP) to provide an additional protection to the trigger chambers: it is called muon filter. Together with the front absorber, it stops muons with $p < 4$ GeV/c. The view of muon filter is shown in Fig. 2.19 along with a warm dipole magnet.

Dipole magnet

A warm dipole magnet is located at ~ 10 m distance from the IP housing the third tracking station and providing the bending power necessary to measure the momenta of muons which is important. The direction of magnetic field is horizontal perpendicular to the beam pipe: x-axis. The central value of magnetic strength is 0.67 T and the integral of field is 3.0 Tm (in 4.97 m). The magnet is also used as a support for the front absorber and beam shield. An additional radial space of $10 - 15$ cm is provided to house the support frames of the tracking chambers inside the magnet. The view of the warm dipole magnet is shown in Fig. 2.19.

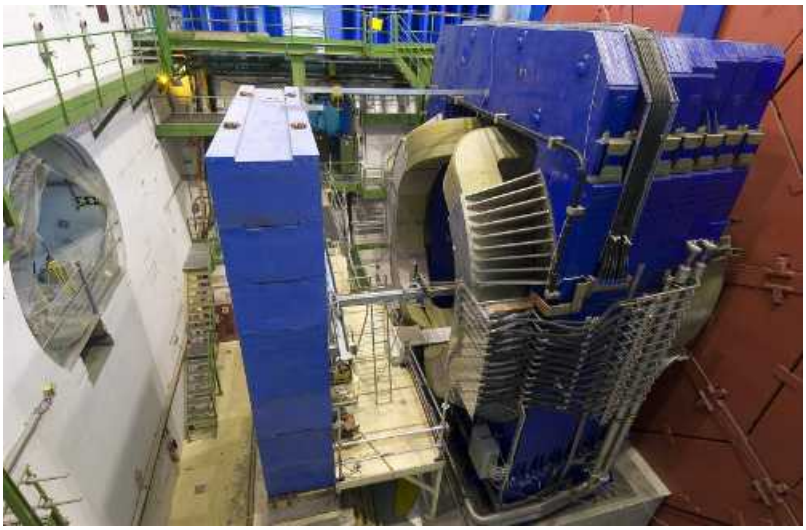

Figure 2.19: View of the muon filter (left) and dipole magnet (right).

2.3.2 Tracking system

Tracking chambers

The tracking chambers were designed to achieve a spatial resolution of about 100 μm, necessary for an invariant mass resolution of the order of 100 MeV/c^2 at the Υ mass [73, 74] and to operate at the maximum hit density of about 5×10^{-2}cm^{-2} expected in central Pb–Pb collisions.

All these requirement were fulfilled by the use of cathode pad chambers. They are arranged in five stations: two are placed before, one inside and two after the dipole magnet. The first station is located right behind the front absorber to measure the exit points of the muons. Each station consists of two chamber planes has different size with two kinds of types: the first two stations are based on a quadrant structure [75, 76], with the readout electronics distributed on their surface; for the other stations, a slat architecture was chosen, see Fig. 2.20, with the electronics implemented on the side of the slats. The slats and the quadrants overlap to avoid dead zones on the detector. Each chamber has two cathode planes, which are both read out to provide two-dimensional hit information.[4] The segmentation of the readout

[4]The clusterization of hits and tracking algorithms are discussed in [77, 78].

pads is implemented following the fact that the hit density decreases with the distance from the beam pipe, and thus larger pads are used at larger radii. This helps to keep the occupancy below 5%.

Tracking electronics

The design of the electronics of the tracking system was driven by two main requirements:

- to read about one million channels up to a rate of the order of kHz;
- and to achieve a space resolution of the tracking chambers of at least 100 μm.

The electronics chain is divided in three parts:

- the front-end boards (FEB or FEE) called MAnas NUmérique (MANU);
- the readout system called Cluster Read Out Concentrator Unit System (CROCUS);
- and the interface with the general ALICE trigger called Trigger CROCUS Interface (TCI) [79].

The FEE is based on a chip called Multiplexed ANALogic Signal processor (MANAS). The channels of four of these chips are read out by the Muon Arm Readout Chip (MARC). This chain is mounted on MANU chip on each FEE. Thus, total 1.08×10^6 channels of the tracking system are treated by about 17,000 MANU cards. In order to achieve the required space resolution, the gain of each channel has to be precisely known (checked just after the assembly of the boards) and they are controlled in periodic calibration runs during the data taking (called *pedestal run*) and stored for the use in off-line track reconstruction.

The Protocol for ALICE Tracking Chambers (PATCH) buses provide the connection between the MANUs and the CROCUS crate. Each chamber is read out by 2 CROCUS (one for half chamber) leading to a total number of 20 CROCUS. The main tasks of the CROCUS are to concentrate and format the data from the chambers, to transfer them to the DAQ and to

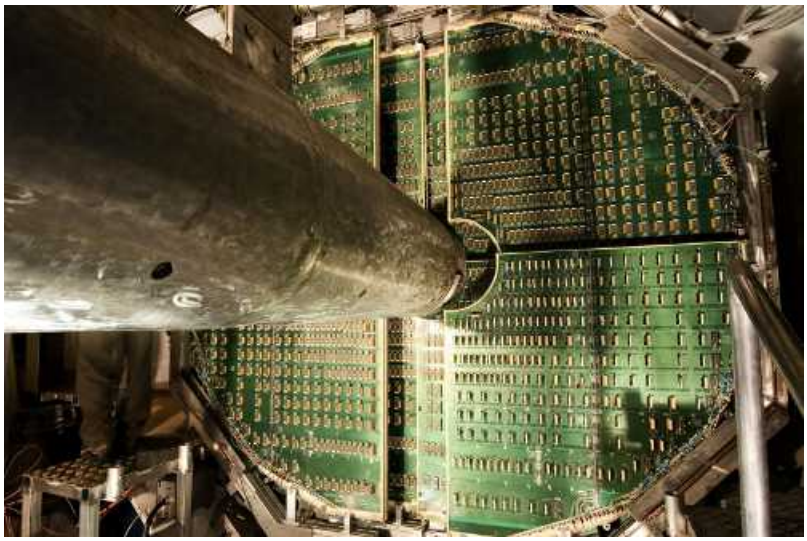

(a) Quadrant structure

(b) Slat structure

Figure 2.20: View of two kinds of tracking station: (a) station 2 (quadrant type); (b) stations 4 and 5 (slat type).

dispatch the trigger signals. Each CROCUS crate houses five frontal (FRT) data readout boards. Each FRT drives up to 10 PATCH buses and collects the data sent by the MANUs. The data from each FRT are transferred to the data concentrator (CRT) board where they are encapsulated and then sent to the DAQ. Therefore, a CROCUS is able to read up to 50 PATCH buses with rates of the order of kHz.

The trigger signals, coming from the Central Trigger Processor (CTP), are distributed to each MANU through CROCUS by TCI. The main goals of the TCI are to decode the trigger signal, to generate the Level-1 reject in the Frontal Fan-out Trigger (FFT) and to manage the busy signals of all the CROCUS crates. All these signals are sent to 20 CROCUS via 5 Frontal Trigger Dispatching (FTD) cards.

Geometry Monitoring System (GMS)

Dedicated runs without magnetic field is carried out at the beginning of each data taking period to align the tracking chambers with straight muon tracks, thus determining the initial geometry of the system. However, the displacements and deformations of the tracking chambers from the initial geometry caused by the magnetic fields are unavoidable. Measuring these displacements is highly important to achieve the required mass resolution. The GMS is an array of 460 optical sensors installed on platforms placed at each corner of the tracking chambers to monitor the position of all the tracking chambers. It measures and records the displacements and deformations of the tracking chambers with respect to the initial geometry during data taking. And these measurements will be implemented into the off-line reconstruction.

The GMS is consist of 3 parts:

- Longitudinal Monitoring System (LMS) monitoring the relative positions between the chamber planes;
- Transverse Monitoring System (TMS) monitoring the flatness of the planes supporting chambers;

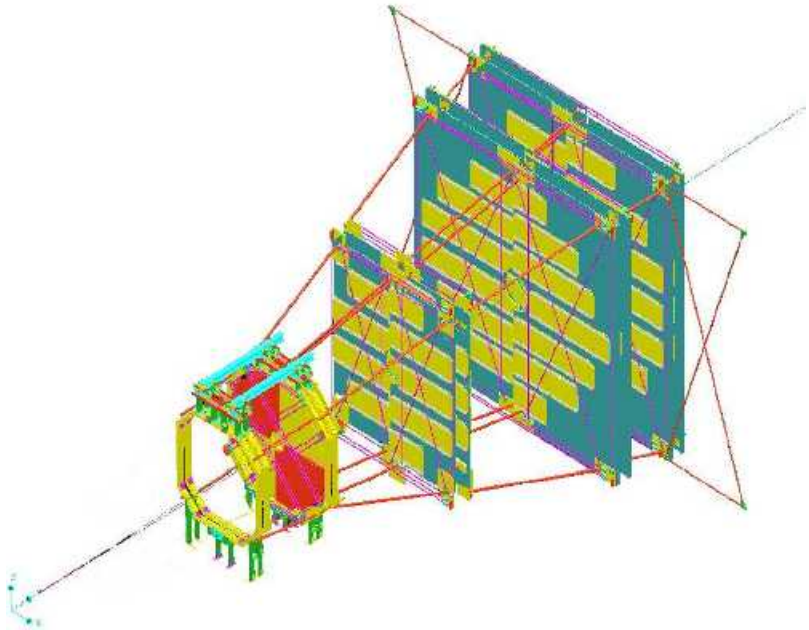

Figure 2.21: General view of the GMS setup. The lines on this figure represent the optical lines.

- and External Monitoring System (EMS) monitoring the displacement of the whole spectrometer.

The GMS setup is shown in Fig. 2.21.

2.3.3 Trigger system

Trigger chambers

Trigger chambers are consist of 4 chamber planes arranged in two stations (one meter apart from each other) placed behind the muon filter at about 16 m distance from the IP. Each plane consists of 18 RPCs with 2 mm single-gas-gap. The hits on RPC are read out by segmented strips providing two-dimensional information: x-strip (horizontal strip); y-strip (vertical strip). Due to the magnetic field produced by the warm dipole magnet, the x-strips measure the bending deviation (bending plane: $x-z$ plane) and the y-strips measure the non-bending deviation (non-bending plane: $y-z$ plane).

The view of the two trigger stations is shown in Fig. 2.22.

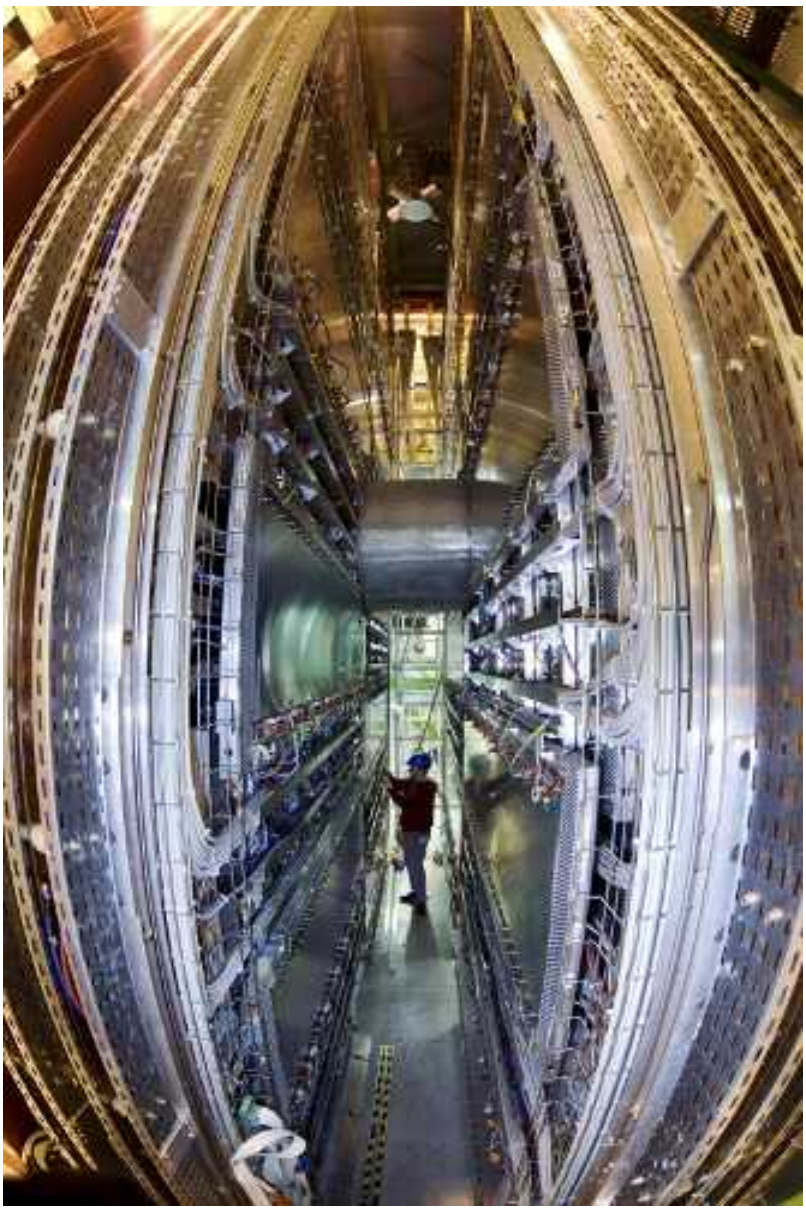

Figure 2.22: View of the two trigger stations.

Trigger electronics

The RPCs are equipped with the front-end boards (FEE). From the FEE, the signals are sent to the local trigger board based on programmable circuits. Each local trigger board forms a trigger zone and thus there are total 234 trigger zones. Figure 2.23 shows a schematic view of the trigger zone positions in one plane of trigger chambers, as seen from the interaction point. The trigger zone density reflects the strip segmentation which is finer in the region close to the beam pipe, where a higher particle multiplicity is expected; moving from the beam pipe outwards, the strip pitch is about 1, 2 and 4 cm in the bending plane and about 2 and 4 cm in the non-bending plane.

The information in one trigger zone includes 4 detector planes, thus the local trigger algorithm reconstruct a single muon trigger track to calculate the momentum of the track. The least requirement of the track reconstruction is hits on at least 3 planes out of 4 planes for both bending and non-bending planes. The momentum of the track is determined by the deviation (the displacement of hit on the last plane with respect to the hit on the first plane) of the trigger track relative to a straight track with infinite momentum representing how much the track is bent by Lorentz force due to the magnetic field of dipole magnet (see Fig. 2.24). All the references are pre-calculated and stored in the local trigger board: called *Look-Up-Table* (LUT). The maximum measurable deviation is fixed to ± 8 strips in the bending plane; and ± 1 strips in the non-bending plane (which ensures that the track comes from the IP). The threshold on the deviation is programmable remotely and the value of p_{t} thresholds ranges from $0.5 - 4.2$ GeV/c. Low-$(0.5 - 1.0$ GeV/c) or high-$(1.0 - 4.2$ GeV/c) p_{t} trigger cut can be changed in data taking period for a physics purpose.

The trigger electronics is organized in 3 levels: 234 local trigger boards, 16 regional trigger boards and a global trigger board. The signals of $9 - 16$ local boards (trigger momentum decisions: low- or high-p_{t}) are gathered by a regional board. 16 regional boards are connected with the global trigger board which decide the final 5 trigger signal to be transferred to CTP (in $\sim$ 800 ns after the collision) out of 6 trigger decisions: single muon low-/high-

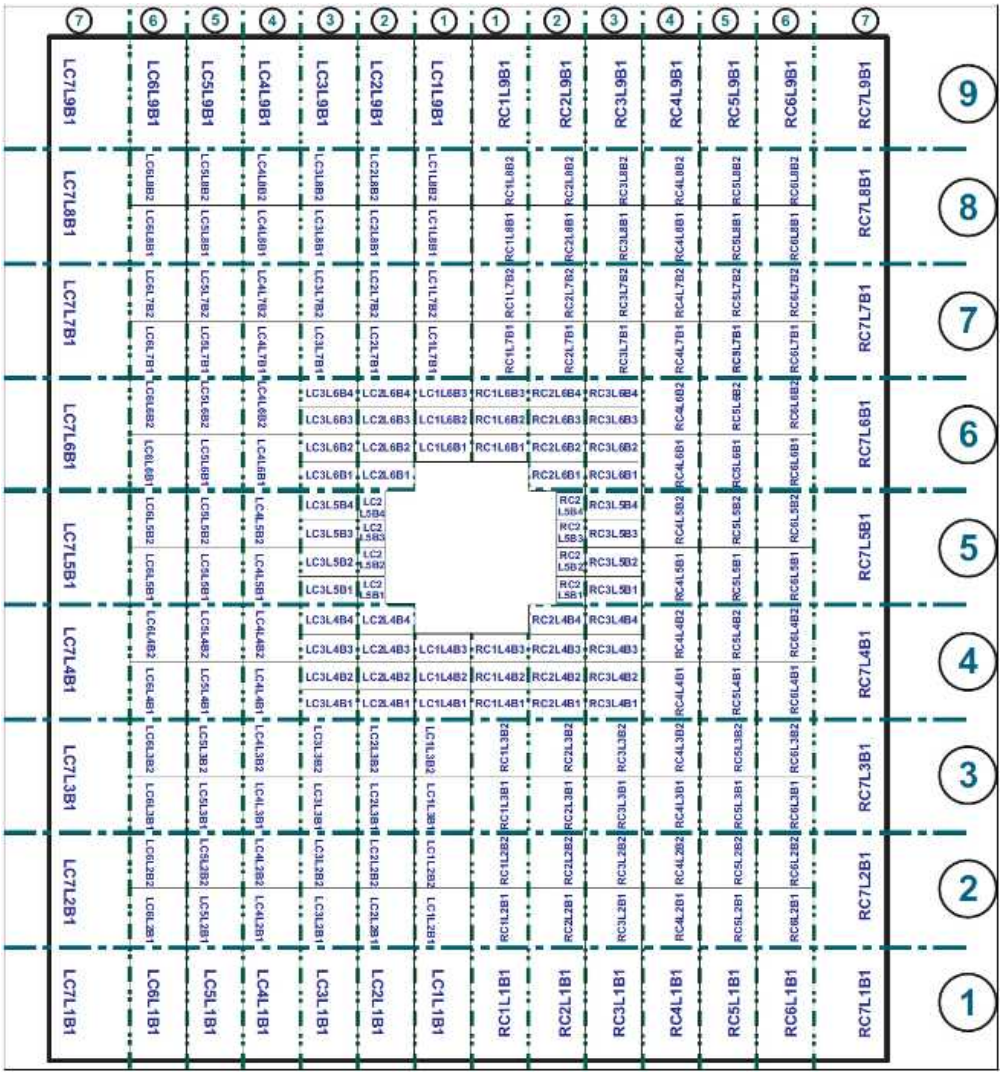

Figure 2.23: Map of the trigger zones boards as seen from the interaction point.

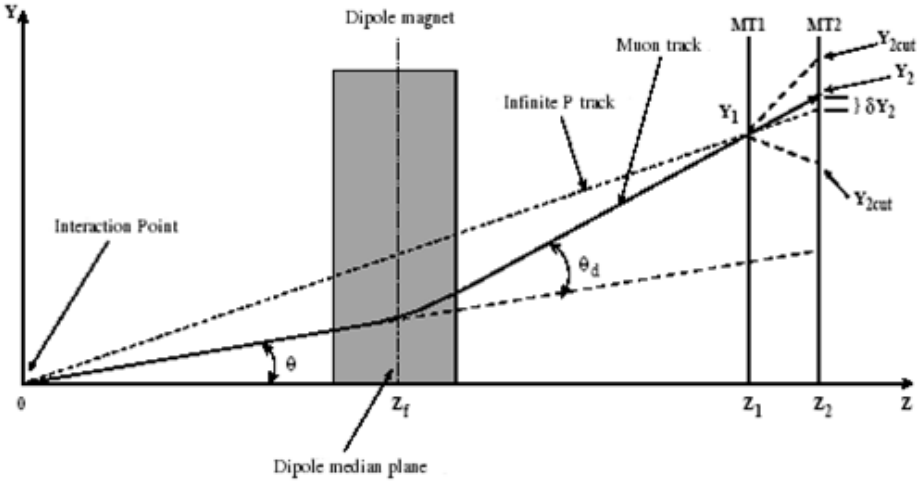

Figure 2.24: The schematic longitudinal view of the muon spectrometer. The track deviation relative to a particle with infinite momentum is computed and then the deviation cut performed by means of look-up tables.

p_{t}; like-sign di-muon low-/high-p_{t}; unlike-sign di-muon low-/high-p_{t}. These are controlled by 2 Di-muon-trigger Alice Readout Controller (DARC) boards: each DARC for half of the detector planes (outside or inside). Only one DARC board is connected to CTP and transfers 5 trigger signals to CTP. And dead channels can be masked and LUT can be update by JTAG board. The schematic view of the trigger electronics organization is shown in Fig. 2.25. The FET generator is used to generate a pulse to FEEs for the test purpose or for the check the electronics. In any cases, it is called *calibration* run, and the all electronics read out the signal generated by FET as well as the scalers containing the information relate to the corresponding electronics. Analyzing these scalers, we can check the status of the trigger electronics, see Sec. 3.3.

2.4 The ALICE off-line framework

The ALICE off-line framework, AliRoot [80] is a software framework based on Object-Oriented technique for programming with the extended detector specific classes and libraries of ALICE grouped with ROOT framework [81]

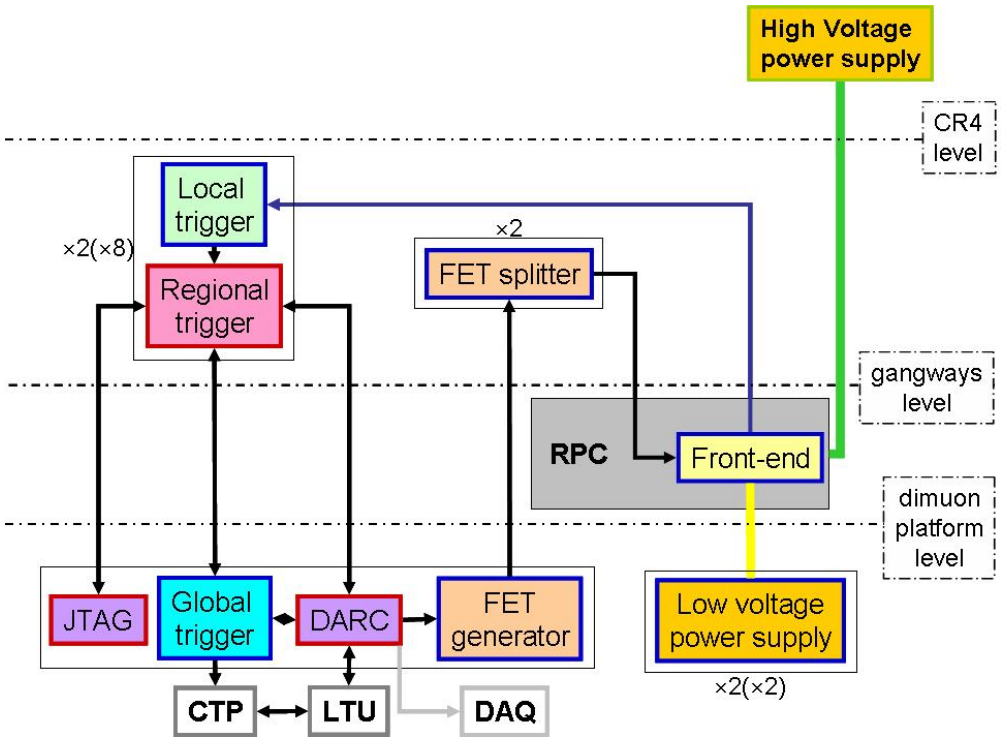

Figure 2.25: The schematic view of the trigger electronics.

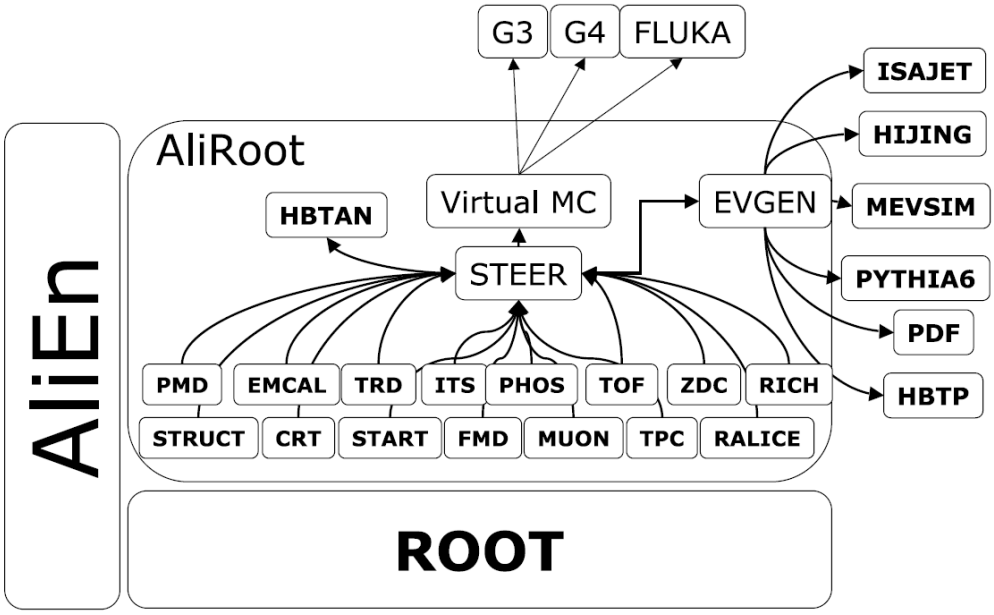

Figure 2.26: Schematic view of the AliRoot framework.

as a supporting framework. It is complemented by the AliEn [82, 83] system which gives access to the computing resources distributed all over the world, so called *Grid*. Its architecture is shown in Fig. 2.26.

The AliRoot framework is used for simulation, alignment, calibration, reconstruction, visualization and analysis of the experimental data. The main simulation class is `AliSimulation` which provides interfaces to event generators and geometry builder (magnetic field generator and access to the alignment as well). The event simulation provided by AliRoot framework has the following options:

- Interfaces to several external generators, such as PYTHIA [59] for pp collisions, HIJING [60, 61] for A–A collisions. Several event generators are available via the generic generator interface class; `TGenerator`.

- η and p_{t} parameterizations for the cases in which the expected transverse-momentum and rapidity distributions of particles are known. Primary particles and their decay can be produced by sampling from parameterized spectra;

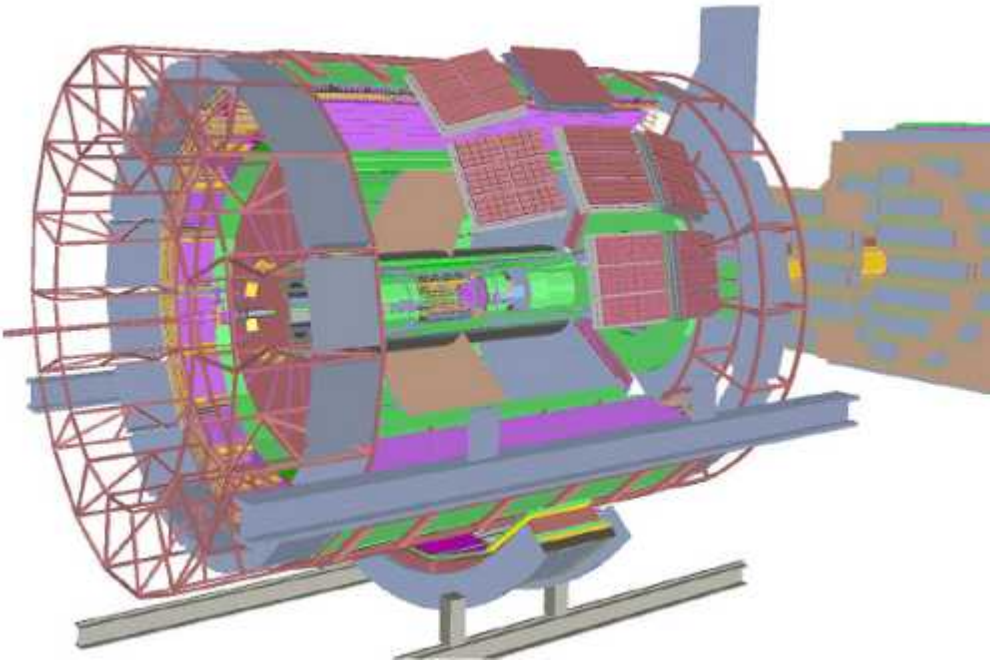

Figure 2.27: Geometry of the ALICE detector in the AliRoot simulation.

- Event merging (so called *Cocktail*) combines signal events and underlying events.

In order to obtain the detector response for the simulated events, AliRoot provides different Monte Carlo packages: GEANT 3 [84, 85], GEANT 4 [86] and FLUKA [87]. They are interfaced to the Virtual Monte Carlo class in ROOT to be able to use them to simulate the ALICE detector via the AliRoot framework. The virtual geometry of ALICE detectors are built in the packages as shown in Fig. 2.27 including support structures, absorbers, shielding, and beam pipe. The magnetic field of the solenoid and the warm dipole magnet can be described in the simulation as well. At the beginning of the simulation, the ideal geometry of ALICE is generated. The modifications of the geometry can be made by accepting the adjustments (measured by calibration or alignment data stored in the Off-line Conditions Data Base (OCDB) [88]) of the parts of the detector different from the ideal one. The simulated particle transport is performed in this modified geometry. The same procedure can be repeated for reconstruction. In this cycle, we can also

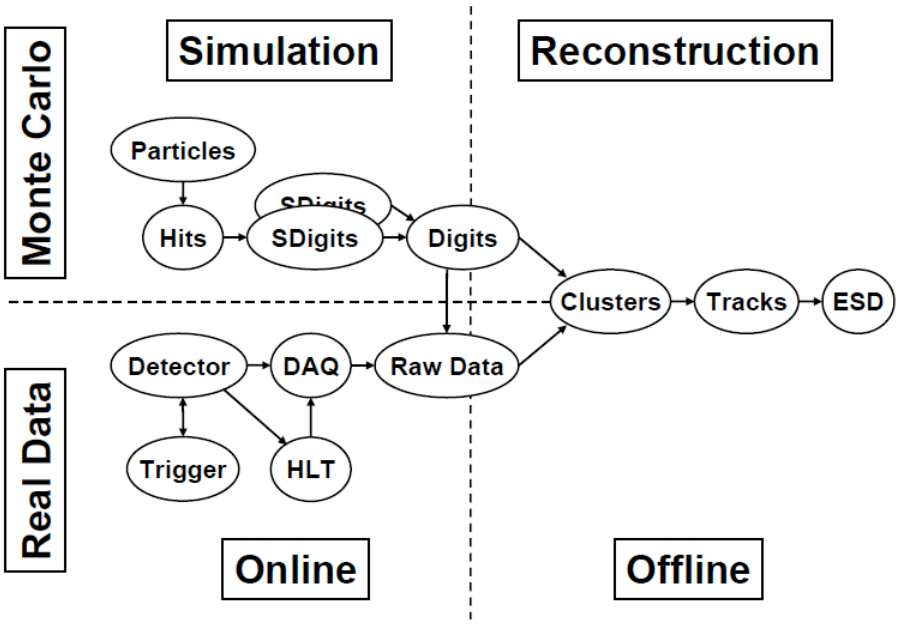

Figure 2.28: Interaction of the reconstruction code with the other parts of AilRoot.

test the effect of detector misalignment and the alignment algorithms which can be useful for real data reconstruction. During the reconstruction of real data, the best geometry is loaded from the OCDB. The first reconstruction (called *pass 1*) is performed with the alignment data from the survey (calibration or geometry monitoring). The subsequent reconstructions (called *pass 2, 3*, and so on) can be performed with the optimized alignment data improving the reconstruction quality.

The reconstruction uses the digits (the output of the simulation) or the raw data produced in data taking, as an input (see Fig. 2.28). The output of the reconstruction is the Event Summary Data (ESD) containing, for example, lists of reconstructed charged particle tracks, particles reconstructed in the calorimeters and so on. The main reconstruction class is `AliReconstruction` which provides interfaces to the reconstruction and configuration of the reconstruction procedure. The sequence of the reconstruction steps are:

- reconstruction executed for each detector separately;

- primary vertex reconstruction;
- track reconstruction and particle identification;
- secondary vertex reconstruction.

The detailed description of the reconstruction and particle identification in all the ALICE detectors can be found in [89].

2.4.1 Correction framework

The Correction framework [90] is the official ALICE procedure used for correction purpose. The simulated data which will be described in Chap. 4, the official Physics Data Challenges in 2009 (PDC09) for the test purpose of the analysis in both steps of Monte Carlo data and reconstructed one, and the real data taken in 2010 at LHC with 7 TeV energies (LHC10g period) to be corrected were used as the input to create the acceptance times efficiency correction map and to perform the correction process of Υ analysis in this framework. This framework consisting of classes which is developed with the purpose of assisting the ALICE users in deriving the corrections. The classes can be grouped into two categories:

- Container classes to store both real and simulated data over binned N-dimensional grids, then to derive the acceptance times efficiency correction maps and correct the observed data;
- Selection classes to give the general selection common to several analyses, at different stages of the selection process.

The container classes are the core of Correction framework and the selection classes are a tool which guide the user in applying selections.

Container classes

The general schema of the Correction framework container classes is shown in Fig. 2.29. These classes are used to store counts over N-dimensional grids (or histograms) while looping on real or simulated event samples at various selection levels (MC or Reco). The dimension of the grid can be any, not

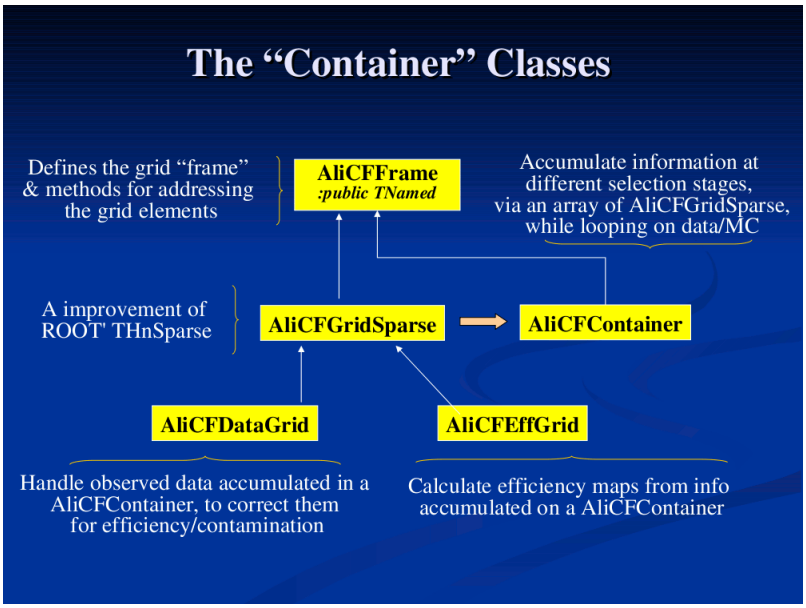

Figure 2.29: The general scheme of the container classes of the Correction framework.

restricted to a certain maximum dimensions. The list of the container classes used in this analysis is reported below, together with a brief description. For all of them, additional information is documented in the header/implementation file of the classes. All these classes inherit from `TNamed` class in ROOT.

- `AliCFFrame`: The base class of the Correction framework. It defines the structure (or *frame*) of the N-dimensional grid. The structure is defined by the number of dimensions of the grid corresponding to the number of variables, the number of bins and binning in each dimension.

- `AliCFGridSparse`: The class containing N-dimensional grid of histograms. This class is based on `THnSparse` class in ROOT, which makes an efficient use of memory for multi-dimensional histograms which are sparsely filled. This class allow to perform basic operations such as addition, multiplication, division, scaling (in the case of conventional TH1, 2, 3 histograms), integration, projection (or slice), etc. In particular, the projection creates a 1-dimensional histogram corresponding to a variable (`ivar`), as well as 2- or 3-dimensional histograms to get the cor-

relation between the variables (`ivar1` and `ivar2` or `ivar1`, `ivar2` and `ivar3`) by using the methods:

```
virtual TH1D* Project(Int_t ivar) const;
virtual TH2D* Project(Int_t ivar1, Int_t ivar2) const;
virtual TH3D* Project(Int_t ivar1, Int_t ivar2,
                                   Int_t ivar3) const;
```

In addition, one can *slice* into a histogram with some cuts on the variables for their analysis purpose, like:

```
virtual TH1D* Slice( Int_t ivar1, Int_t ivar2=-1,
                     Int_t ivar3=-1, Double_t *varMin,
                     Double_t *varMax) const;
```

- `AliCFContainer`: The class books and fills a group of N-dimensional grids. Any number of analysis steps can be configured for either real data or simulated one (for both MC and Reco). The efficiency between two different steps can then be derived by dividing the contents of the two corresponding grids, to be then applied to the appropriate set of observed data. The filling of the grid corresponding to step, `istep`, is performed by calling the following function:

  ```
  virtual void Fill(Double_t *var, Int_t istep, ...);
  ```

- `AliCFEffGrid` and `AliCFDataGrid`: The classes handle the acceptance times efficiency map and the uncorrected/corrected data, respectively. The acceptance times efficiency corresponding to two different steps, for example, `istep1` (reconstructed data as a numerator) and `istep2` (Monte Carlo simulated data as a denominator) can be derived by calling the method in the former:

  ```
  virtual void CalcualteEfficiency(Int_t istep1, Int_t istep2);
  ```

  In the acceptance times efficiency calculation, binomial errors are always assumed. The latter is used to deposit the measured (uncorrected)

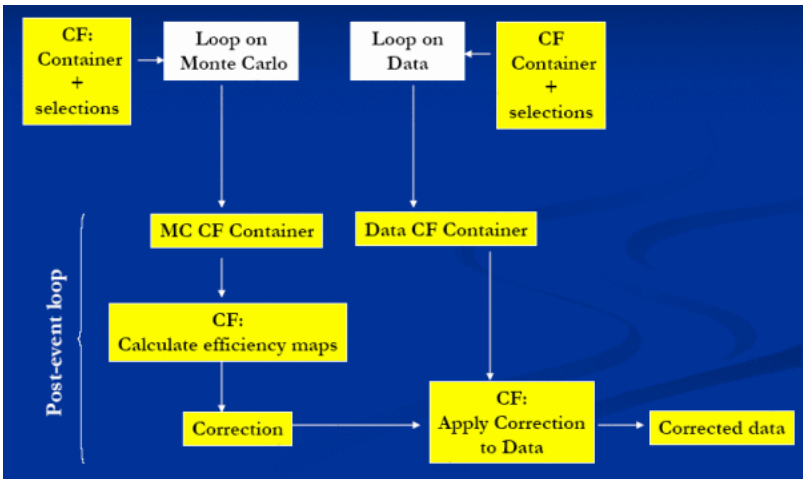

Figure 2.30: A typical flow of the correction process.

data stored in an `AliCFContainer` at a given step, and then the correction can be performed (by using the result stored in the `AliCFEffGrid`) via the method:

```
virtual void ApplyEffCorrection(const AliCFEffGrid &eff);
```

A typical flow of the correction process is shown in Fig. 2.30.

Selection classes

A set of classes handling general selections at Event or Particle-level has been prepared. The selection classes are based on the code in PWG0 AliRoot repository, `AliPWG0Helper` and `AliESDtrackCuts`. The base class for selection classes is `AliCFCutBase`, which derives from `AliAnalysisCuts`. The list of some selection classes used in this thesis work is the following:

- `AliCFParticleGenCuts`: Non-kinematic basic selections on generated particles, for example, PDG code, decay mode, vertex, charge, etc.
- `AliCFTrackKineCuts`: Kinematic selections on both generated and reconstructed tracks, for example, momentum range, charge, rapidity, etc.

2.4.2 Dedicated classes for Υ analysis

A set of codes dedicated for Υ analysis based on the Correction framework has been composed and committed to AliRoot package. It consists of two classes:

- `AliCFMuonResUpsilon`: The class, based on `AliAnalysisTaskSE` class, that accumulates information with the event selections from the simulation data, for example PDC09 data, as well as the real data into N-dimensional grids and filling a `AliCFContainer`-type object. This class has a capability to read both type of data, Event Summary Data (ESD) type and Analysis Of Data (AOD) type (a detailed description of these data types can be found in [80]) stored in the local path or on the remote storage connected with Grid (thanks to the interface with AliEn). In addition, the physics selection (see Sec. 2.4.2 for more details) task is introduced in this stage for the real data analysis;

- `upsilonCORRFW`: The class performs the main tasks with the `AliCFContainer`-type object built in the `AliCFMuonResUpsilon` class, for example, creating an efficiency correction map; fitting the data point in case of reconstructed/real data; then performing the efficiency correction.

An additional C++ macro is required to configure variables of the `AliCFContainer`-type object, together with their bins and binning and selection cuts based on the selection classes of the Correction framework. In addition, this macro provides the input and output management for the analysis. In particular, it has an interface to the Grid connection offered by the AliEn plug-in. The list of variables in `AliCFContainer`-type object used in this analysis is the following:

- For event selection,
  - the number of event with/without event selections or cuts for quality check including the physics selection;
  - the event trigger side of the collisions (beam-beam, beam-empty, and empty-empty) according to the fired trigger classes[5];

[5]ALICE DAQ/CTP configures the trigger classes during data-taking as following the

- For Υ or $\mu^+\mu^-$ candidates,
  - p_t, rapidity and invariant mass of Υ at the generation level in case of Monte Carlo simulated data, and $\mu^+\mu^-$ pair candidates at the reconstruction level in both cases of Monte Carlo or real data;
- For single muon tracks,
  - kinematics of single muon tracks: momentum, charge, pseudo-rapidity (η), z-component of vertex, R_{abs} (the radius from the beam line at the end of the front absorber), etc.;
  - a digit for track-trigger matching on each muon track with low-/high-p_t cut at trigger electronics level.

The comparison of the results between ESD and AOD was performed with the simulation in order to make sure that the result is consistent with different data type, and then take advantage of AOD. Since AOD is produced from ESD with only interesting kinematics and parameters for a specific analysis purpose, for example, we produce muon AODs in which there are nothing but only muon tracks, thus the size of AOD is much reduced than ESD that leads to reduce the computing resources, especially the size of storage required to store data as well as the computing time to process the data. As shown in Fig. 2.31 and Fig. 2.32, the results of two different data types with the same data set seem to be consistent each other.

Physics selection

A dedicated class for the physics selection, `AliPhysicsSelection`, selects events that:

- have the correct event type (tagged as *physics* during data taking);

detector partitions. During 2010 data taking the main trigger classes were [91]: CINT-type for minimum bias events and CMUS-type for muon events. According to the collision type, the trigger classes are separated as A (beam-empty), B (beam-beam), C (empty-beam) and E (empty-empty). Therefore we can figure out the interested physics events with the name of those trigger classes, for example CMUS1-B-NOPF-ALL for muon event after the beam-beam interaction.

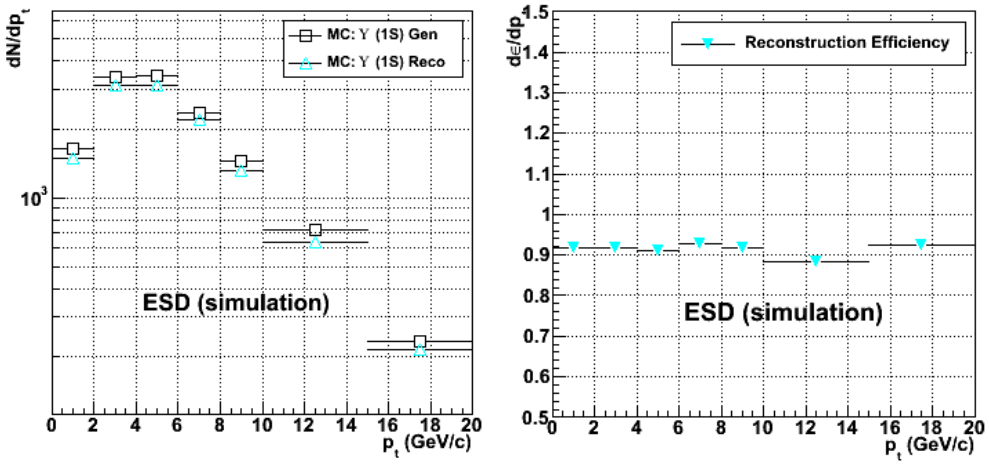

(a)

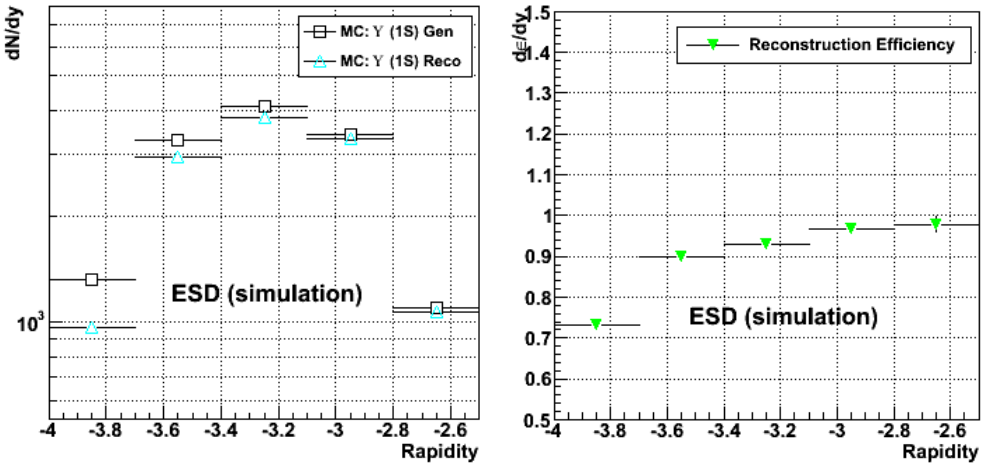

(b)

Figure 2.31: The (a) p_{t} and (b) rapidity distribution of simulated $\Upsilon(1S)$ and corresponding reconstruction efficiency obtained from ESD type data.

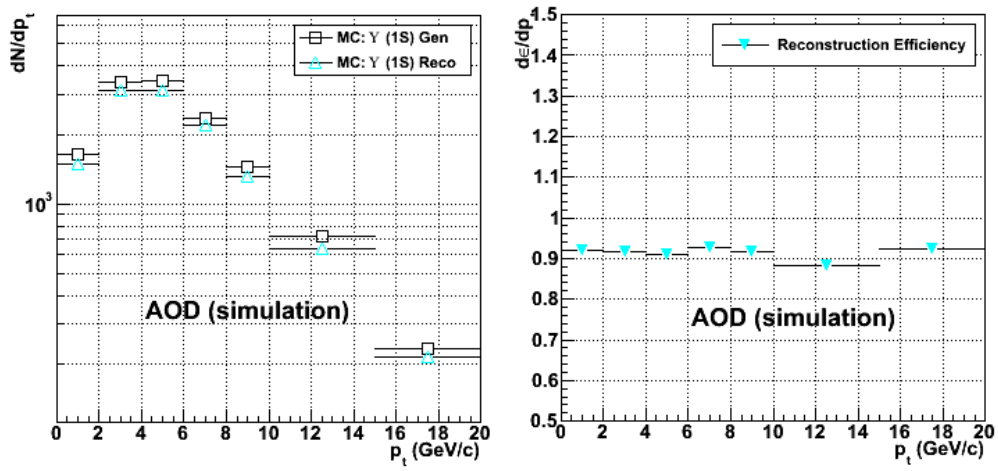

(a)

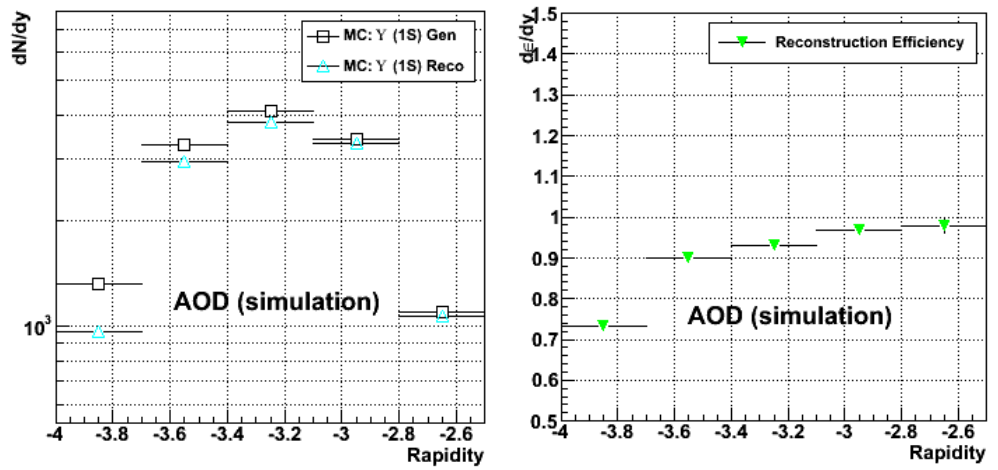

(b)

Figure 2.32: The (a) p_{t} and (b) rapidity distribution of simulated $\Upsilon(1S)$ and corresponding reconstruction efficiency obtained from AOD type data.

- have the interaction trigger, *i.e.* trigger on bunch crossings, for example CINT1-B triggered events;
- fulfill the on-line trigger condition (hardware trigger);
- are not flagged as beam-empty (or beam-gas) event by either V0A or V0C;
- for pp collisions, are not flagged as beam-gas based on the correlation of SPD clusters and tracklets;
- for Pb–Pb runs, are not identified as *debunched* events by the ZDC timing cut.

In this thesis work, we used `AliVEvent::kMUON` for muon trigger among the options defined in `AliVEvent::EOfflineTriggerTypes`. In order to activate the physics selection in the user analysis, add the task `AliPhysicsSelectionTask` in C++ macro by using:

```
gROOT->LoadMacro(
        "$ALICE_ROOT/ANALYSIS/macros/AddTaskPhysicsSelection.C");
AliPhysicsSelectionTask* physSelTask = AddTaskPhysicsSelection();
```

Then, we can use the result of the selection inside `AliCFMuonResUpsilon` class with the following line:

```
// for minimum bias event
Bool_t isSelected = (((AliInputEventHandler*)
       (AliAnalysisManager::GetAnalysisManager()->
       GetInputEventHandler()))->IsEventSelected()
                                              & AliVEvent::kMB);


// for muon analysis
Bool_t isSelected = (((AliInputEventHandler*)
       (AliAnalysisManager::GetAnalysisManager()->
       GetInputEventHandler()))->IsEventSelected()
                                            & AliVEvent::kMUON);
```

More detailed discussion can be found in [92].

Chapter 3

Online DQM for Muon Trigger

Data Quality Monitoring (DQM) is an important aspect of every High-Energy Physics experiment. It is evident that a feedback on the quality of the data which are actually recorded for offline analysis is of great importance, especially in the era of LHC where the detectors are extremely complicated devices. The Data Acquisition and Test Environment (DATE) [93, 94], which is the main DAQ software framework of ALICE, provides a low-level monitoring package which forms the basis of any high-level monitoring framework for ALICE. It exposes a uniform Application Programming Interface (API) for accessing on-line raw data on DAQ nodes as well as data written in files. It gives the possibility of selecting the event sampling strategy for on-line streams in order to balance the required computing resources.

In this chapter, the development of software for online DQM of the raw data, produced by ALICE Muon Trigger system, will be described. The aim of this software is to provide information of data-taking status as well as the status of the electronics of muon trigger to shifters. It is designed to be able to display the quality of the data by decoding the raw data format, which contains hits, scalers and bits presenting the status of the system at each stage: from detector to signal trigger.

This online monitoring tool was developed on the two different frameworks: firstly, the Monitoring Of Online Data (MOOD) and subsequently, it was adapted to the Automatic MOnitoRing Environment (AMORE), and both of them are based upon the DATE. This tool publishes monitor ob-

jects, which are defined from the necessity of the detector group, such as raw data structure, data size, multiplicity of electronics participating in the corresponding data, efficiency of 4 trigger RPC planes, 6 global trigger output and corresponding scalers generated via the muon trigger algorithm, in the form of histograms. In addtion, any anomalies, for example, the raw data in the non-standard structure and size, and the error arised in the trigger algorithm calculation, found in the course of the decoding are displayed in a way easily recognizable.

3.1 Interactive Data Quality Monitoring: MOOD

MOOD [95] is the project aimed to serve the interactive DQM needs of ALICE. It is written in C++ and makes heavy use of the ROOT framework which provides Graphic User Interface (GUI) and the analysis tools such as histograms and graphs. The interface to the DAQ is provided by the DATE monitoring library. MOOD provides a framework by the template feature of C++. This helps that any user class derived from an Abstract Base Class (ABC) can redefine the pure virtual functions of the base class and execute the custom code; while it makes whole MOOD package strongly dependent on each detector code developed by users. The base classes of MOOD are: `TMMainFrame` is the main class for the modules and provides the generic GUI functionalities, such as menu bar, status bar, and so on; `TMBaseModule` is the ABC that can be derived for any detector modules. The following virtual functions drive the monitoring process:

- `InitMonitors`: This is used to acquire configuration/values settings from the GUI and store them in C++ variables so that user code can access them at runtime. For example, if a user enters a value in a textbox, the value should be copied in a variable by this function.

- `ResetMonitors`: This function is called when the histograms is needed to be reset, for example when the *Reset* button is pressed.

- UpdateMonitors: This function is called to update the screen. User code selects the appropriate pad where a histogram should be drawn

and issues a screen drawing command.

- `PreMonitor`: This function is excuted after the update of the screen. It follows that analysis is done on all the events in the background while the update of screen is being processed.

- `PostMonitor`: The code in this function is executed before the update of the screen.

- `MonitorEvent`: Actual analysis for monitoring is taken place in this function. The event fragments are accessible by MOOD API that can help user code to be able to subsequently decode the payload, to perform analysis and to store the results, usually by filling histograms. MOOD API provides all the information for the event, for example event type and trigger masks, which are available by DATE. These information can be expolited to differentiate the behavior of MonitorEvent according to the event type: physics event or calibration event, for instance.

- `UpdateMonitors`: This function is excuted periodically at a given time or by request.

- `ConstructMonitors` and `ConstructGUI`: They are helpful for each module to book the histograms and to create GUI.

There are two mode of monitoring operations supported by MOOD, see Fig. 3.1.

- By pressing *Get Event* button the following call sequence is implemented: `InitMonitors`, `PreMonitor`, `MonitorEvent`, `PostMonitor`, and `UpdateMonitors`.

- By filling a number N in *Maximum number of events* textbox or a period M in terms of number of events in *Update period* textbox, the total number of events N to be monitored as well as the update period M of the screen and pressing the *Start Event Loop* button the following call sequence is implemented: `InitMonitors`, $N/M\times$ (`PreMonitor`, $M\times$`MonitorEvent`, `PostMonitor`, `UpdateMonitors`).

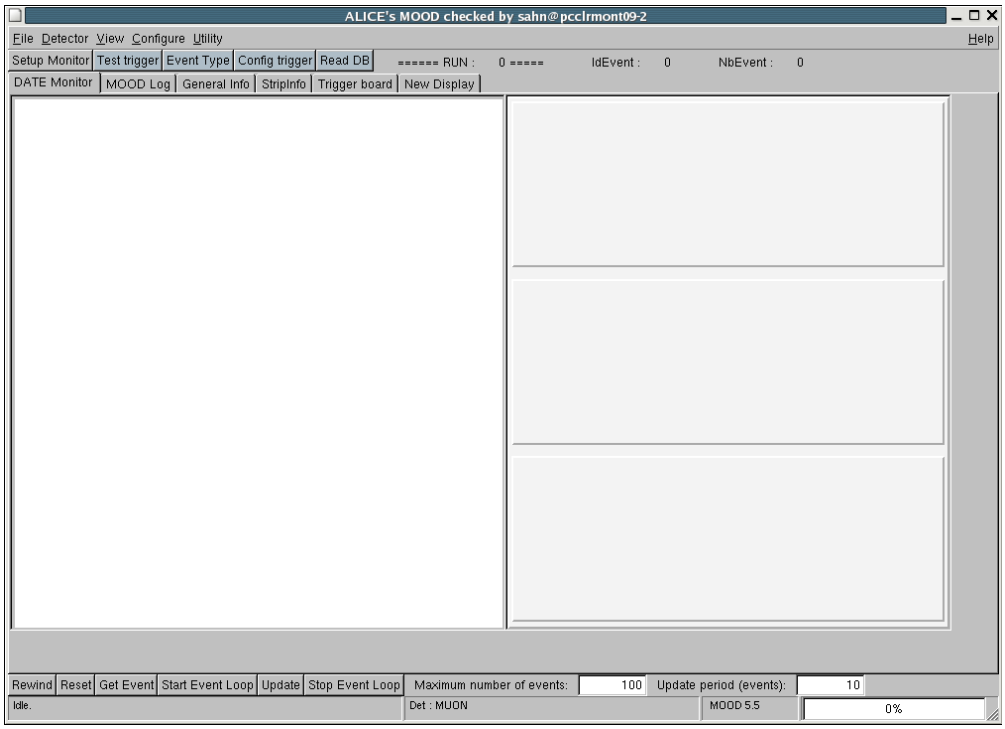

Figure 3.1: Example of MOOD screen view.

MOOD has been playing an important role during the commissioning phase with its solid design and supports by the project team in ALICE. From the beginning of LHC running, the role has been handed over to the new *automatic* DQM framework, AMORE, which has been doing a great role since the data taking started.

3.2 Automatic Data Quality Monitoring: AMORE

In such a complex system of ALICE, a large number of information (for example, histograms) is produced, distributed and consumed by users simultaneously which cannot be fulfilled with an interactive *server-client* scheme where MOOD is based on. And the heavy dependence on the detector code of MOOD can be a serious obstacle of the development, especially for the beginners.

Upon these requirements, AMORE [96] features the *publish-subscribe* scheme involving many-to-many connection between publishers (`amoreAgents`), subscribers (`amoreClients`), and the intermediate pools for data exchange (`amorePools`). It is designed to be independent on the detector codes as well by introducing *reflective programming*[1]. The comparison between features of MOOD and AMORE are shown in Fig. 3.2.

The 3-tiers of publish-subscribe scheme of AMORE are described as the following (see Fig. 3.3):

- `amoreAgents` as publishers have access to raw data, process the data to produce the `MonitorObjects`, and publish them on the pools.
- `amorePools` are implemented as the MySQL [98] database servers for the exchange of `MonitorObjects`. This allows the transactions of `MonitorObjects` between `amoreAgents` and `amoreClients` without any direct transfers.
- `amoreClients` can subscribe to `MonitorObjects` on any `amoreAgents`, thus `amoreClients` will recieve regular updates on the contents of the

[1] In computer science, reflection is the process by which a computer program can observe and modify its own structure and behavior at runtime. The first notion of computational reflection was introduced in [97].

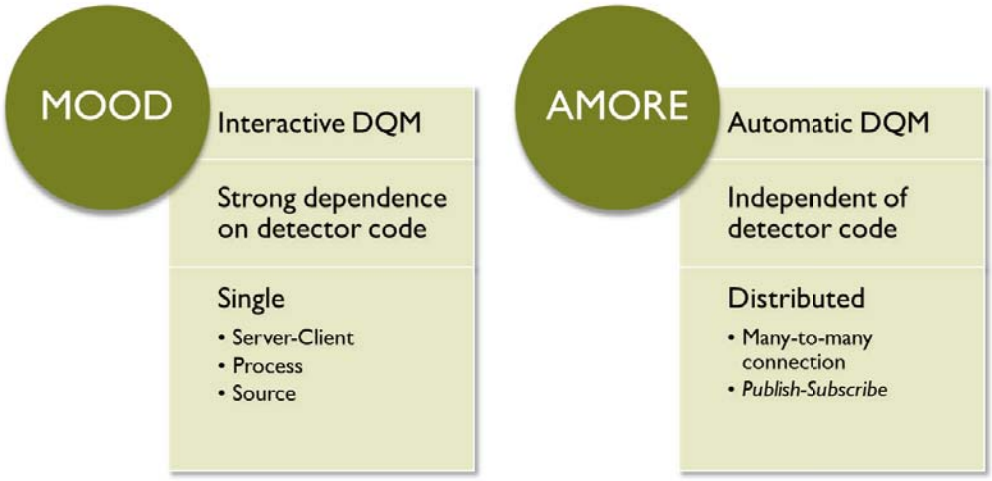

Figure 3.2: The comparison between the features of MOOD and AMORE.

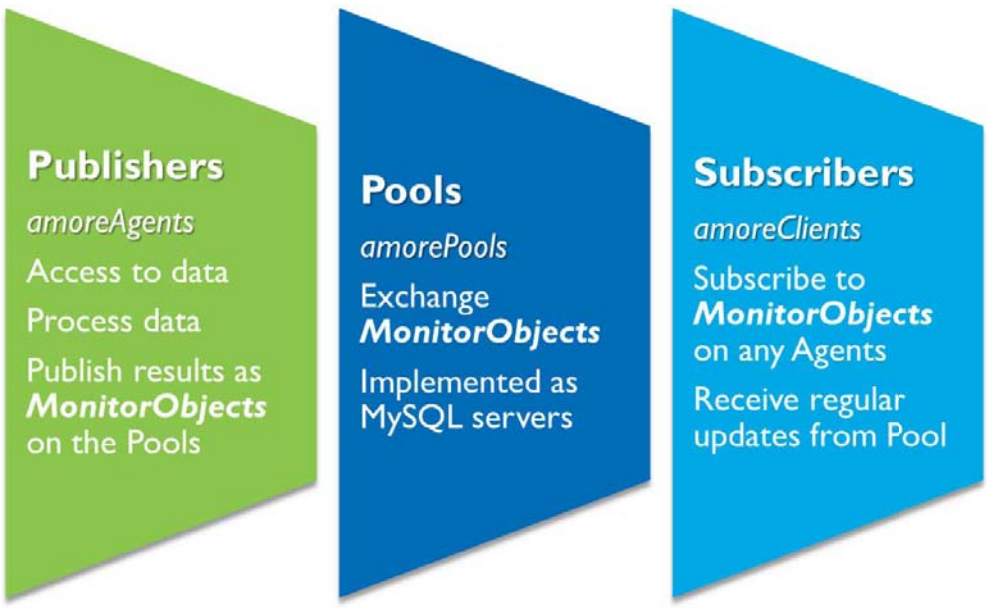

Figure 3.3: Publish-subscribe scheme of AMORE.

subscribed `MonitorObjects`.

The `amoreAgents` decode and transform the raw data into physical quantities, and store in the form of `MonitorObjects`. For the moments, it suffices to consider the `MonitorObjects` as histograms. The `amoreAgents` dispatch the `MonitorObjects` to `amorePools`. Each `amoreAgent` can connect to only one `amorePool` for this purpose. The `amoreAgents` can also access to `MonitorObjects` published by other `amoreAgents`.

To accomplish the execution of user code, the `amoreAgent` subsequently calls member functions of an abstract based class, called `PublisherModule`. User code implements the pure virtual functions of this class in derived classes and a specific part of the agent, called `Publisher`, calls these derived member functions. The same approach is followed throughout the framework where large parts of user-defined code are to be executed. For this purpose, specialized abstract base classes exist for a subscriber and for a generic GUI client.

Each `amoreAgent` is represented by a table in a database. Each row of the agent table is associated with a `MonitorObject` that is published by the agent at any given moment. As with the DATE software environment, MySQL is used to define the configuration of the framework, namely the initial conditions for each agent, such as the operating node, the associated pool and the data source.

It is practical to define an abstraction that can unify the various types of histograms and other less utilized but still useful data types. The base class, named `MonitorObject`, is abstract and holds an interface which is common for all the derived classes. For example there are functions to retrieve the identity of the `MonitorObject` or to reset it. The derived classes are mostly template-based, for example a `MonitorObjectScalar<ScalarType>`, that can be instantiated for all the C++ fundamental data types. The same holds for various types of histograms which are instantiated using the relavant ROOT data types, for example 1-, 2- and 3-dimensional histograms; 1- and 2-dimensional histogram profiles.

The publishing interface follows the general form,

```
void Publish(MonitorObject<Type>*&, "unique name", ...);
```

where the first argument is a refence to a pointer of a templated `MonitorObject` as described above. The second argument is a character string representing the `MonitorObject`s unique name. A unique identification for every `MonitorObject` is the form of a pair with `amoreAgent` name and `MonitorObject` name with a qualified pathname, such as

```
/amore/<amoreAgent name>/<MonitorObject name>.
```

Finally, a variable number of arguments follow in the sense of several overloaded `Publish` function definitions with different number of arguments.

The subscription interface follows the general form,

```
void Subscribe(MonitorObject<Type>*&, "unique name");
```

A shortly typed version of the subscription function also exists, namely

```
void Subscribe("unique name");
```

In this case, as there is no direct pointer handle, user code queries the subscription backend executing in C++ pseudocode the following operation

```
MonitorObject<Type>* pointer=
                    dynamic_cast<MonitorObject<Type>*>
                    (gSubscriber->GetMonitorObject("unique name"));
```

where `gSubscriber` is the interface to the subscription backend.

3.3 Development of online DQM software for Muon Trigger

There exists an online DQM tool for ALICE Muon Trigger system developed on both framework, MOOD and AMORE as mentioned at the beginning of this chapter. Only MOOD-based version of the tool for detector experts was prepared during the commissioning phase of the detector. It provides detailed information useful for experts in the form of one and two dimensional histograms. For example, the hit multiplicity of each FEB on each trigger station can be monitored as shown in Fig. 3.4a. Each pad can be zoomed

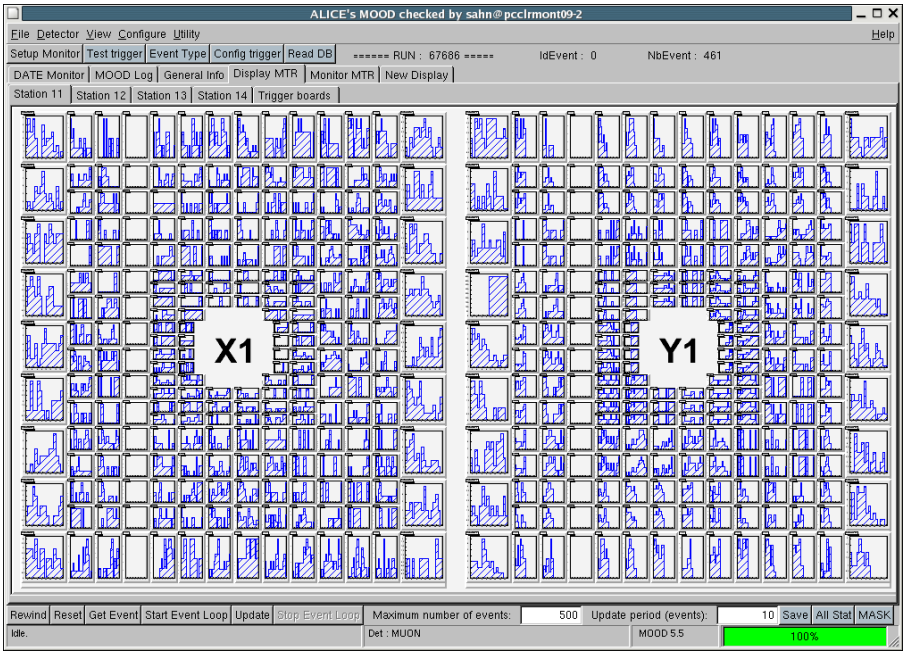

(a)

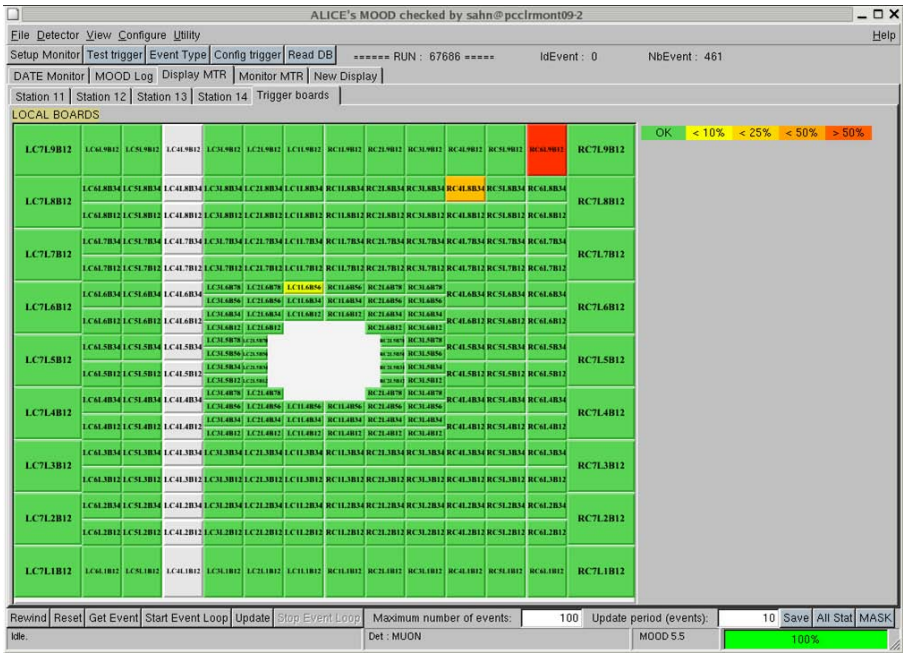

(b)

Figure 3.4: An example view of (a) hit multiplicity panel and (b) trigger algorithm panel of MOOD expert version. There is a missing column in both figures due to the problem with a regional trigger board. A mal-functioning local trigger board can be found in (b).

in by clicking the pad which is implemented by the ROOT user interface class `TButton` in which one can easily find out noisy channels or errors on the specific electronics. In addition, it provides a detailed checks for trigger algorithm and two dimensional histograms for the hit multiplicity of strips and local trigger boards as shown in Fig. 3.4b.

Although the expert version is useful and extended, it takes much of time to load and update its own histograms that makes it hard to display the histograms without delay in a short time interval. In addtion, some of histograms are not appropriate for the non-experts, who take shifts during the data taking. These prevent it from being used in that period, therefore, a fast and easy-to-use version, called *shift* version of the online DQM tool is required.

The development of the shift version based on MOOD was started checking and reporting the raw data structure of ALICE Muon Trigger at the beginning. First of all, it was mandatory to understand the mechanism of payload decoder and the structure of raw data coming from the electronics through the Detector Data Link (DDL). By understanding them, we can display any histograms containing the information as we want to see. In addition, it was necessary to know how to construct GUI in order to implement the histograms in MOOD, and eventually, to construct a new GUI for shift version. After the implementation of the shift version of MOOD was complete, the conversion into AMORE had started. The name of AMORE module for shift is *MTRUI3*, where *MTR* is the detector code in AMORE framework. The general scheme of AMORE modules for trigger system is described in Fig. 3.5. The shift version of MOOD and AMORE are now installed at the ALICE control room. The screen view of the shift version of MOOD and AMORE is shown in Fig. 3.6.

3.3.1 Payload decoder

The payload decoder translates the raw data of standard structure provided by ALICE. An ALICE raw event includes an event header of 17 words (1 word = 32 bits) and the DDL structure [99]. The DDL sub-event begins with an equipment header of 7 words followed by a Common Data Header

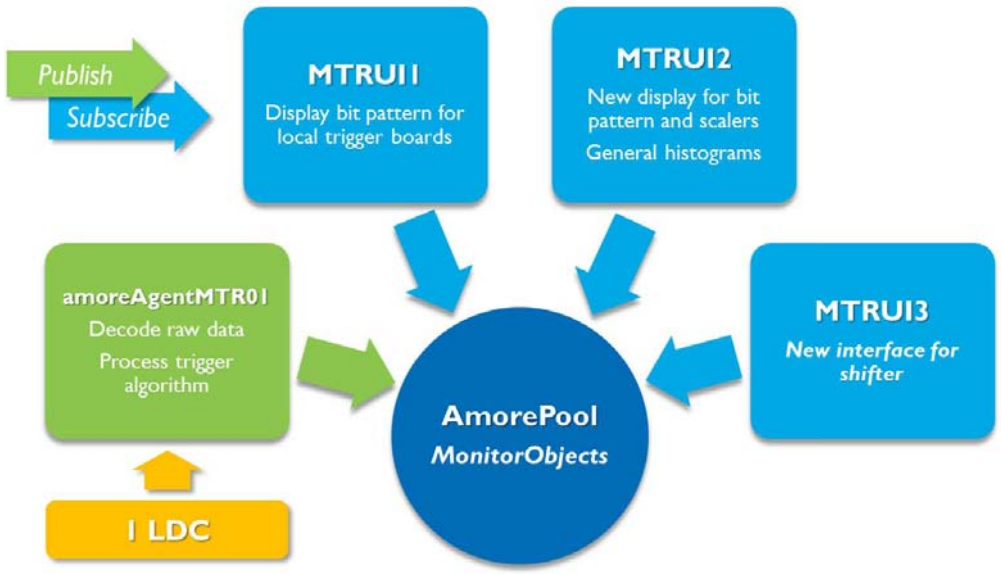

Figure 3.5: A general scheme of AMORE modules for trigger system. Green-colored boxes represent the publish process while green-colored boxes represent the subscribe process. Yellow-colored box indicates the raw data flow from the detector. `amoreAgentMTR01` is a `amoreAgent` responsible for publishing the `MonitorObjects` of muon trigger system. There are 3 subscribers: MTRUI1 and MTRUI2 for expert view; MTRUI3 for shift view.

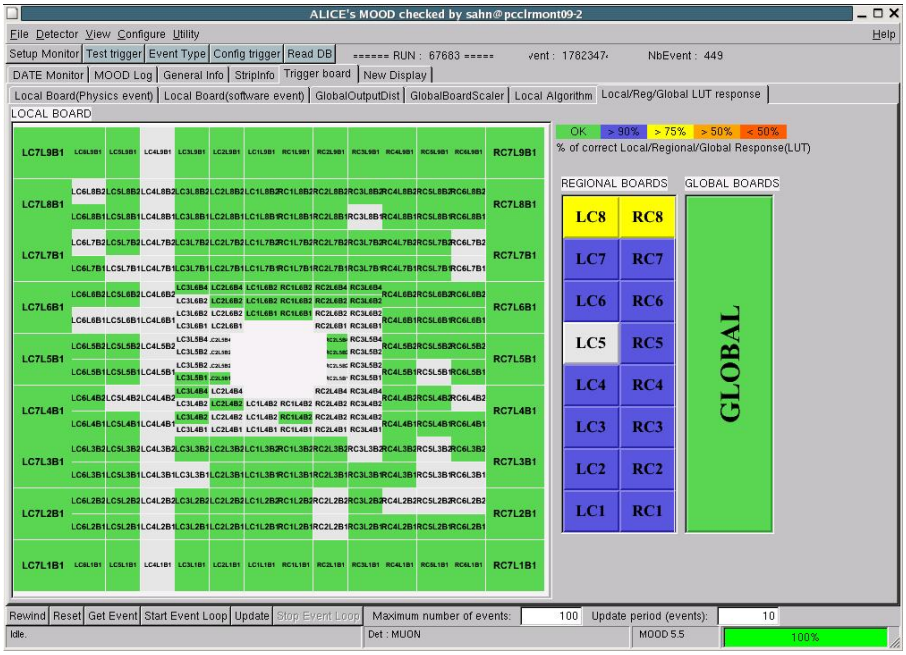

(a)

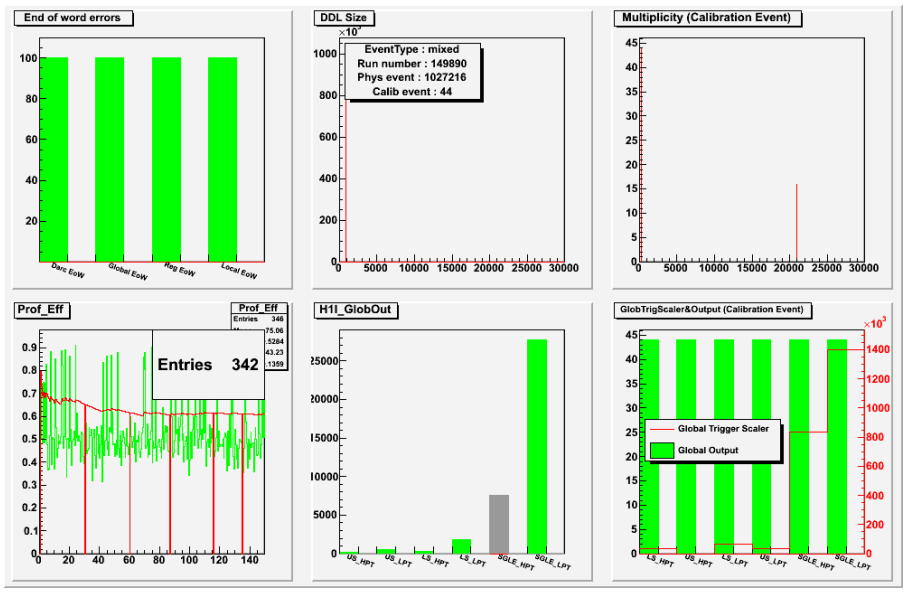

(b)

Figure 3.6: Example view of the shift version of (a) MOOD and (b) AMORE.

(CDH) of 8 words. For Muon Trigger, the equipment is referred as Dimuon-trigger Alice Read-out Controller (DARC). The data flow of ∼21,000 strips is concentrated in two DARCs, Right-DARC and Left-DARC. An overall view of a DDL event of Muon Trigger is shown in Fig. 3.7. The DDL event header contains 8 additional words, followed by 8 regional controller structures, including the 16 local controller structures. There are two types of data structure depending on the type of the trigger. For a physics trigger, only data from the detectors are read out while for software triggers (the events from calibration run) additional information (from scalers) is read out as well. The scalers allow to check the counting rate of detector: noise from detector and FEE and background from cosmic-ray. There are extra words for the DARC, global trigger board, regional trigger boards and local trigger boards.

DARC header. It consists of a word (32 bit) containing trigger occurrence (2 bits) and global trigger output (6 bits). The global output contains the 6 single and dimuon triggers: single muon high/low-p_{t}, like-sign dimuon high/low-p_{t}, and unlike-sign dimuon high/low-p_{t}. These global information are present in one DARC header (one DDL from R-DARC), in the other header, the words for global trigger board are set to zero. In addition, the header contains global board data occurrence bit, separator words, and scaler words (8 words for DARC and 10 words for global trigger boards) if the case of software event. The separator words are written at the end of each trigger board words, therefore it is also called *End of Words*. For DARC header, the separator is 0xDEADFACE and 0xDEADBEEF should be set at the end of global header.

Regional board header. The regional board header consists of 4 words: DARC status word, Regional word, and 2 words of regional input corresponding to the 16 local trigger boards data. The DARC status word contains flags for Level 0, Level 1 and Level 2 trigger accepted/rejected (1 bit each), regional trigger occurrence (1 bit) and etc. The value of the DARC status word will be set to 0xCAFEDEAD when the regional trigger board is masked or could not be readout. In the regional word, the output of re-

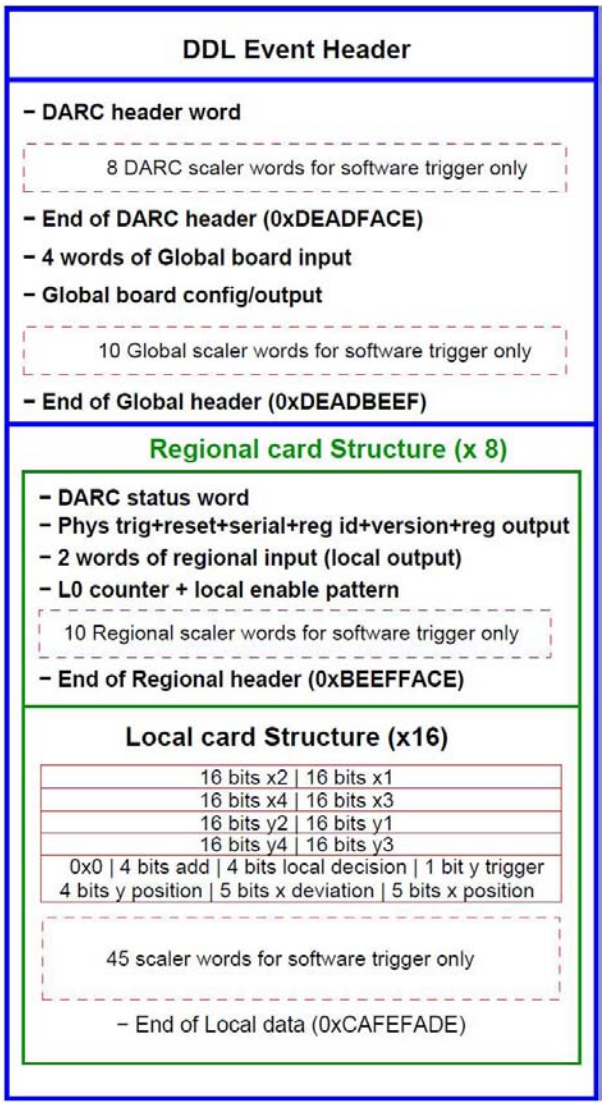

Figure 3.7: Schematic view of the DDL raw event for trigger chambers.

gional board is filled in 8 bits: 2 bits for single high-p_{t} muon; 1 bit for unlike-sign dimuon pair of high-p_{t} muon; 1 bit for like-sign dimuon pair of high-p_{t} muon; 2 bits for single low-p_{t} muon; 1 bit for unlike-sign dimuon pair of low-p_{t} muon; 1 bit for like-sign dimuon pair of low-p_{t} muon. 2 bits of low-p_{t} and 2 bits of high-p_{t} for each local board are sent as the input of regional tigger board. And 10 additional scaler words will be added when calibration run is performed. The separator word for the regional header is 0xBEEFFACE.

Local board structure. The local board structure format contains 5 words: 16 bits each ($\times$ 8) corresponding to position along x and y axis in the 4 planes of 2 stations and a word containing bits for trigger information from the local trigger board decisions and deviations. Additional 45 scaler words are added if the case of software event. The end of word for each local header is 0xCAFEFADE.

In AliRoot software package, there are several classes prepared for decoding the raw data. A detailed description can be found in [100]. The main decoding classes used for Muon Trigger are:

- `AliRawReader` is an abstract base class for reading raw data. Depending on the raw data format, file (DDL format or ROOT format) or stream provided by DATE, there are derived classes: `AliRawReaderFile` (or `AliRawReaderRoot`), and `AliRawReaderDate`. These derived classes implement the method to access the spectific detector part of raw data by using the equipment identification number (ID) of the read-out electronics of detectors. For Muon Trigger case, the equipment IDs of two DARCs, R-DARC and L-DARC of Muon Trigger are 0xB00 and 0xB01, respectively. For AMORE, the `AliRawReaderDate` class interfaced with a method provided by AMORE core is used to access the raw data. In case of MOOD, the class `TDATEEventParser` provides a method, `GetEquipmentById`, to help access the spectific detector part of raw data and dump a buffer containing the header of read-out electronics of each detectors identified by their ID number. This is implemented in `TMBaseModule`. In addition, `AliRawReader` provides some methods

which help to obtain the information about the event: `GetRunNumber` to get the run number of data currently reading, `GetType` to get the event type of data (physics event or calibration event), and `GetEventId` to get the number of events.

- `AliMUONDDLTrigger` is a dedicated class for Muon Trigger that provides interfaces to access each electronics part of raw data. The references to each part of raw data in memory and their sizes received from `AliRawReaderDate` (or `TDATEEventParser`) can be stored in this class.

The actual examples of setting raw reader and handing it over to the decoder in both MOOD and AMORE are the following:

```
// for MOOD
const equipmentHeaderStruct* const equipmentHeader =
                                    GetEquipmentById(iEquipmentId));
...
UInt_t* buffer = (UInt_t*)equipmentHeader +
                     (sizeof(equipmentHeaderStruct) + CDH_SIZE)/4;
fMTRDecoder->Decoder(buffer,iEquipmentId);
```

where `GetEquipmentById` method returns the pointer to the raw data of the corresponding equipment and the size of buffer, `equipmentHeader` is a `struct` type named `equipmentHeaderStruct` defined in the library which corresponds to the raw data in AliRoot package, `sizeof` returns the size in bytes, and `CDH_SIZE` is defined as 8×4 (= 32 bytes). To get the size of the buffer in words, we divide the calculated size by 4. Then, the decoder was called with the buffer and the equipment ID.

```
// for AMORE
SetRawReader(new AliRawReaderDate(GetEvent()->DATEEvent()));
...
UChar_t data[GetEquipmentDataSize()];
GetDecoder()->Decode((UInt_t *)data, GetEquipmentId());
```

where `SetRawReader` function set a raw reader with the data from DATE, a buffer to store the data was allocated with the size of the data, and then the buffer and the equipment ID were handed over to the decoder module.

At the beginning of decoding, the decoder takes over the data stored in the buffer and deal it with `AliMUONDDLTrigger` class. And as mentioned above, this class has interfaces to the additional classes corresponding to each trigger electronics which provide essential methods that can be used to obtain the information in the raw data at each electronics level. They are `AliMUONDarcHeader`, `AliMUONRegHeader`, and `AliMUONLocalStruct`. To get the header of DARC, for example, a method, `GetDarcHeader` in `AliMUONDDL-Trigger` class can be used, like

```
AliMUONDarcHeader* darcHeader = fDDLTrigger->GetDarcHeader();
```

where `fDDLTrigger` is an instance of `AliMUONDDLTrigger` class. In a simliar way, the global trigger output in the DARC header can be extracted by using `GetGlobalOutput` method in `AliMUONDarcHeader` class. The other useful information for checking the status of electronics and data quality are available via these classes.

3.3.2 Monitoring objects

In this section, the implemented monitoring objects in the shift version of DQM software for Muon Trigger are listed.

Raw data structure. As described above, in both cases of physics and calibration event, the structure of the raw data is solid and each level of the raw structure is separated by the separator. However, keeping eyes on the structure is not unimportant since some corruptions had been found in the structure during the commissioning phase due to the failures of the electronics or the network. By checking the *End of Words* of each header: 0xDEADFACE (DARC); 0xDEADBEEF (global board); 0xBEEFFACE (regional boards) and 0xCAFEFADE (local boards), we can estimate the corrupted rate of the raw data structure, and then it will be displayed in the monitoring module as shown in Fig. 3.8 (for MOOD implementaion) and Fig. 3.9 (for AMORE). In addtion, the size of the raw data, simply called

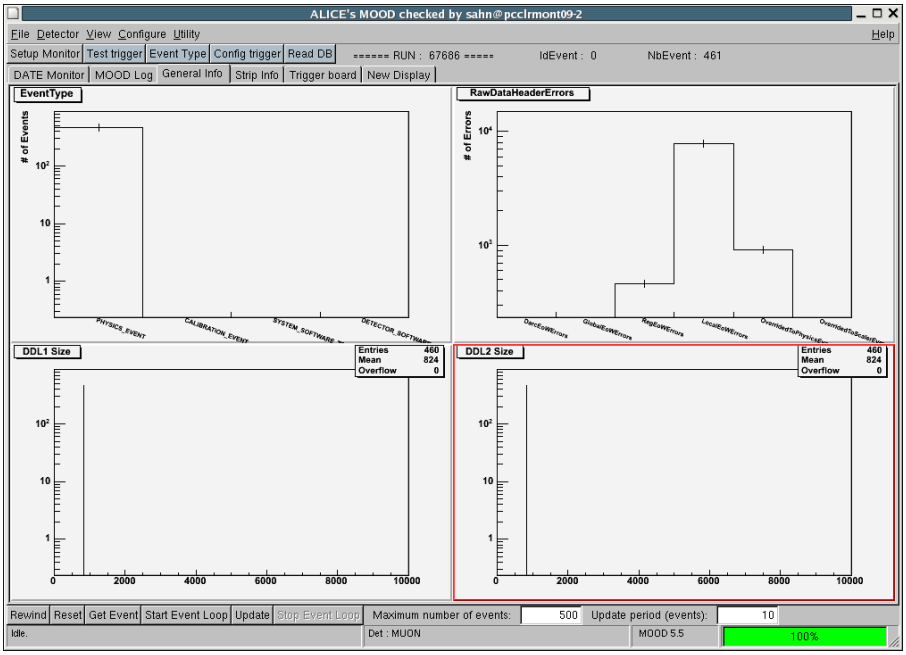

Figure 3.8: Example screen view of raw data structure of MOOD implementation for the shift version. The event type of this example is figured out physics run (top-left), and therefore the size of DDL is 824 (bottom). Some of *End of Words* errors are shown (top-right).

DDL from each side of DARC, can be also another good key to assure the quality of data. For calibration run, the size of DDL should be 6682 due to the additional scalers while 824 (without scalers) for physics run.

Multiplicities of fired electronics for calibration events. Whenever calibration run is performed, the output of electronics should be consistent unless there are problems: 20992 fired strips, 234 local trigger decisions, 16 regional trigger decisions, and 6 global trigger decisions. Therefore the changes in the multiplicity of each trigger level could be a good indicator for the status of electronics. We can check these numbers from the input of header at each trigger board level. For example, Right-side DARC header has the output of global trigger board as its input and global header has the output of regional trigger boards as the input, and so on. From this, we can figure out how many trigger boards are fired by the pulse or hits. The fired strips are shown in case of calibration run with MOOD shift module in Fig. 3.10

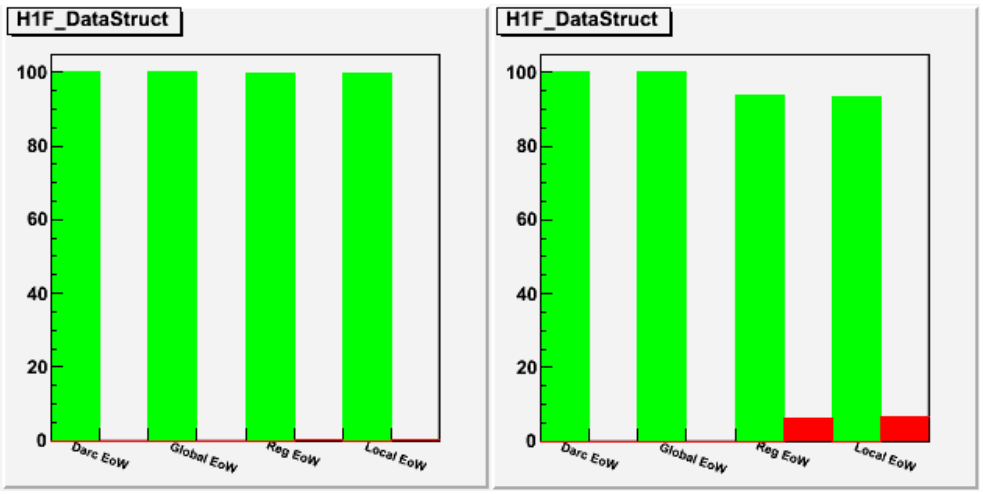

(a) (b)

Figure 3.9: Example plots of raw data structure of AMORE implementation. The green bars indicates the purity of the raw data structure at each electronic level. From the left to the right, DARC, Global, Regional and Local board. (a) No corruption is showed in the left panel. (b) In the right panel few corrupted rates of raw data structure in the regional and local structures are indicated in red color (Tested data was obatined during the cosmic ray test phase and there were few corruptions on separation words at Regional and Local words which are now fixed).

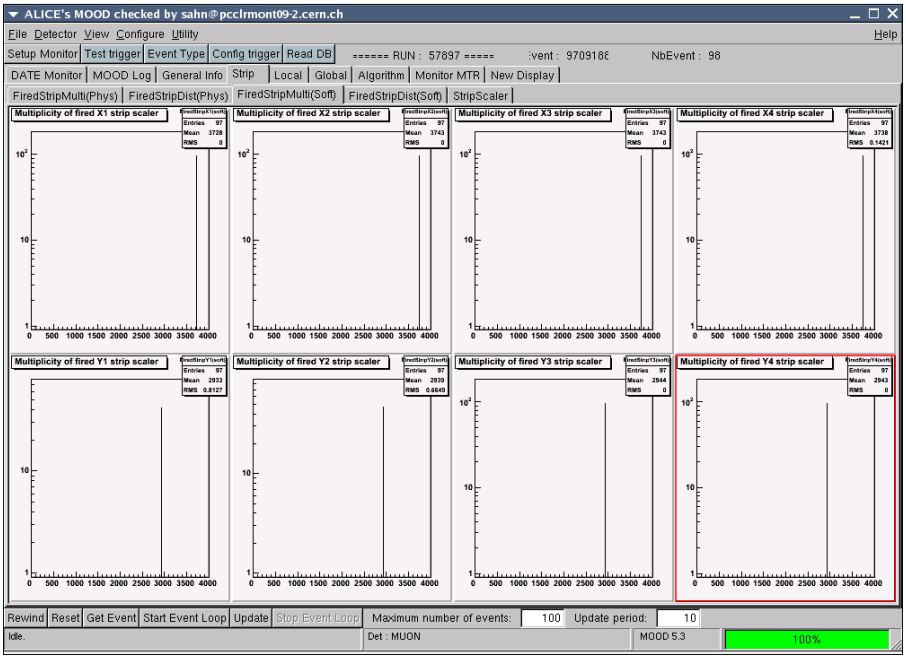

Figure 3.10: Example screen view of fired strip multiplicities with MOOD shift module.

and the multiplicities of each trigger level with AMORE shift module in Fig. 3.11.

Trigger efficiency. The ratio of the trigger rate of 4 trigger planes over the 4 planes divided by the trigger rate of 3 trigger planes over the 4 planes, which is referred to as trigger efficiency 44/34, should be consistent in both physics run (much below the 100% but converge around some point) and calibration run (∼100%) as shown in Fig. 3.12. This is not implemented in MOOD shift version, but shown in MOOD expert and AMORE shift/expert modules.

Global trigger output. The 6 muon trigger decisions: single muon low-/high-p_{t}, like-sign dimuon low-/high-p_{t} and unlike-sign dimuon low-/high-p_{t} trigger, are displayed as well as the single muon trigger choice whether low-p_{t} or high-p_{t}. If there is some errors in the global trigger algorithm, these events are indicated after the verification on the trigger algorithm. See Fig. 3.13.

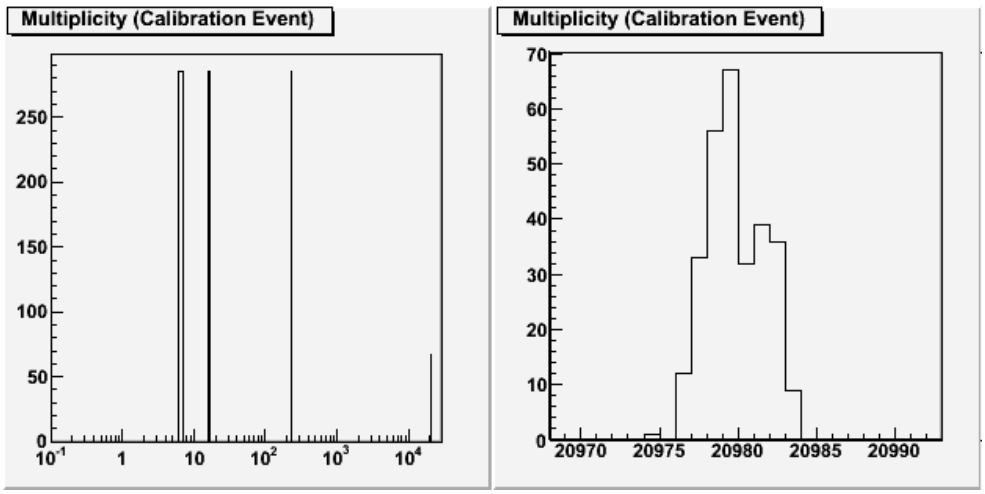

(a) (b)

Figure 3.11: Example plots of fired trigger boards with AMORE shift module. (a) The multiplicities of each trigger boards are 6 for global board, 16 for regional boards, 234 for local boards and 20992 for strips (from left). (b) The zoomed-in view of the strip multiplicity shows that fluctuation of the number of strips in muon trigger chambers event-by-event with small deviations.

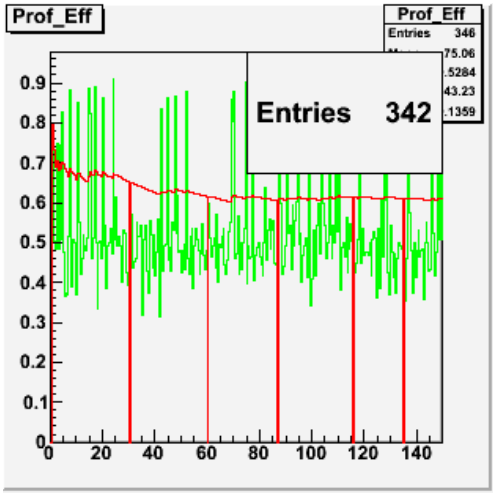

Figure 3.12: Example plot of the trigger efficiency 44/34 as a function of time implemented in AMORE shift module. The green line is the ratio for physics run over time (in minutes) and the red line indicates the overall average of the ratio at the given time which looks become stable as time goes. In this example, the calibration runs are included between the physics runs that leads to the slight increase of the overall fraction (in red).

Global scalers for calibration events. We can check the status of global trigger board by monitoring the global scalers from the header of DARC board for calibration events. As shown in Fig. 3.14, global trigger output in green bars for calibration run is consistent for all trigger decisions. In addition, L0 scaler, clock scaler and L0 hold scaler are provided in MOOD for further check.

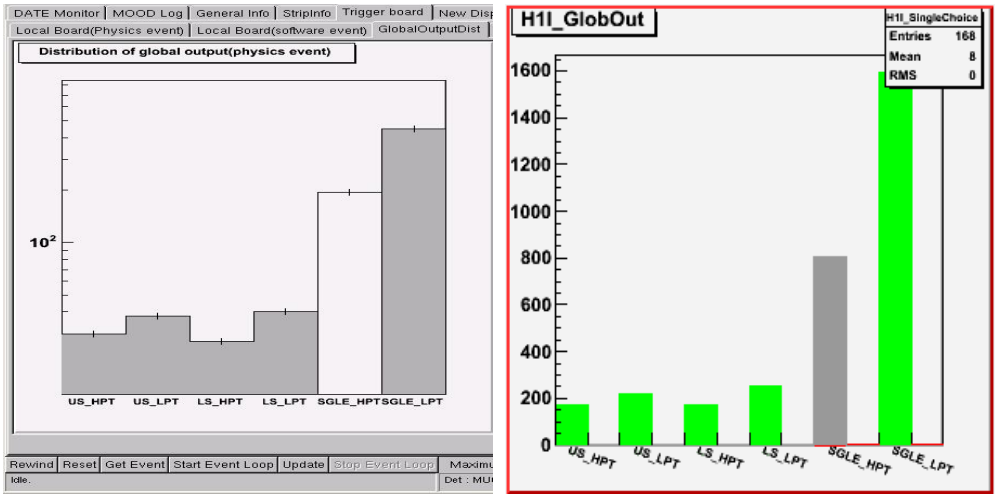

Figure 3.13: Example plots of global trigger output of MOOD implementation (left) and AMORE implementation (right). The white bar (left) and grey bar (right) represent the single muon choice which not transferred to CTP. For AMORE, red bar will be shown up if there is any errors of global trigger algorhtim (global trigger output are re-calculated with the input from lower level trigger boards in the decoder, and then it is compared with the output of global trigger board).

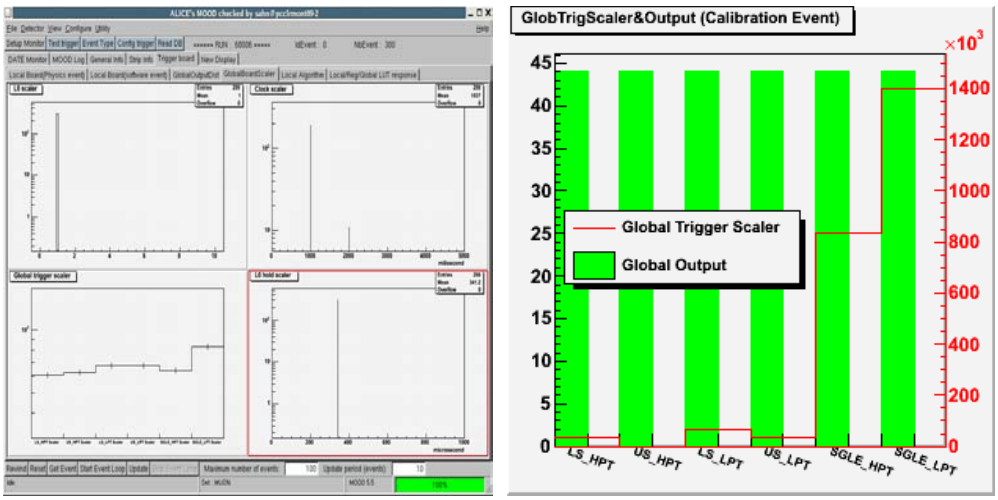

Figure 3.14: Example plots of global scaler shown in MOOD (left) and AMORE (right) for calibration run. The red line represents global scalers read-out during calibration event and the green bars represent global output of calbration run.

Chapter 4

Data Analysis

The aim of this thesis work is to measure the total cross section and the differential cross section of $\Upsilon(nS)$ in $\mu^+\mu^-$ channel in pp collisions at 7 TeV energy with the ALICE muon spectrometer. The differential cross section of $\Upsilon(nS)$ production in pp collisions as a function of the transverse momentum $p_{\rm t}$ and the rapidity y, can be expressed as the following:

$$\frac{{\rm d}\sigma_{{\rm pp}\to\Upsilon(nS)}}{{\rm d}p_{\rm t}} = \frac{1}{{\rm B}_{\Upsilon(nS)\to\mu^+\mu^-}\cdot\langle A\times\epsilon\rangle_{\Upsilon(nS)\to\mu^+\mu^-}}\cdot\frac{{\rm dN}_{\Upsilon(nS)\to\mu^+\mu^-}}{{\rm d}p_{\rm t}}\cdot\frac{\sigma_{\rm pp}}{{\rm N}_{\rm pp}}$$

$$\frac{{\rm d}\sigma_{{\rm pp}\to\Upsilon(nS)}}{{\rm dy}} = \frac{1}{{\rm B}_{\Upsilon(nS)\to\mu^+\mu^-}\cdot\langle A\times\epsilon\rangle_{\Upsilon(nS)\to\mu^+\mu^-}}\cdot\frac{{\rm dN}_{\Upsilon(nS)\to\mu^+\mu^-}}{{\rm dy}}\cdot\frac{\sigma_{\rm pp}}{{\rm N}_{\rm pp}}$$

where

- $\sigma_{\rm pp}$ is the total cross section of pp collisions at LHC energy, derived from $\sigma_{\rm V0AND}$ [1]. The recent measurement of ALICE in pp collisions at 7 TeV energy shows $\sigma_{\rm pp} = 62.3 \pm 0.4(stat.) \pm 4.3(syst.)$ mb [102].

- ${\rm N}_{\rm pp}$ is the number of minimum bias events corresponding to the muon sample used in the analysis. Together with $\sigma_{\rm pp}$, we can determine the integrated luminosity: ${\rm L}_{\rm pp} = {\rm N}_{\rm pp}/\sigma_{\rm pp}$. The integrated delivered luminosity to ALICE by LHC in 2010 is ${\rm L}_{\rm pp} \approx 0.5$ pb^{-1} [103].

- ${\rm B}_{\Upsilon(nS)\to\mu^+\mu^-}$ is the probability for each $\Upsilon(nS)$ to decay into muon

[1] Measurable cross section of two V0 detectors via van der Meer (vdM) Scan (also known as Vernier Scan) [101]

Table 4.1: The mass and branching ratio of the charmonium, J/ψ and bottomonium states, $\Upsilon(nS)$, quoted from the Particle Data Group (PDG) [2].

States	J/ψ	$\Upsilon(1S)$	$\Upsilon(2S)$	$\Upsilon(3S)$
Mass (GeV/c^2)	3.10	9.46	10.02	10.36
$B_{Q\bar{Q}\to\mu^+\mu^-}$ (%)	5.93 ± 0.06	2.48 ± 0.05	1.93 ± 0.17	2.18 ± 0.21

pair (see Tab. 4.1).

- $\langle A\times\epsilon\rangle_{\Upsilon(nS)\to\mu^+\mu^-}$ is the average value of geometrical acceptance multiplied by the reconstruction efficiency of $\Upsilon(nS)$ with the ALICE muon spectrometer. We can quantify $\langle A \times \epsilon\rangle$ correction factor by using the simulation with a realistic detector configuration corresponding to the data used for the analysis and taking the average value for whole data periods.

- $dN_{\Upsilon(nS)\to\mu^+\mu^-}/dp_t$ or $dN_{\Upsilon(nS)\to\mu^+\mu^-}/dy$ is the number of reconstructed $\Upsilon(nS)$ (signal) detected via $\mu^+\mu^-$ decay in a given p_t or y range. In order to extract the number of signal precisely, we performed a fit to the invariant mass spectrum of $\mu^+\mu^-$ pair.

This chapter contains the Monte-Carlo(MC)-based-analysis performed during the data taking period in 2010. Thanks to the MC production, we were able to build and test a C++-based-analysis-framework especially for Υ analysis (described in Sec. 2.4.2). In this chapter, we present a prediction on the yield of $\Upsilon(nS)$ when we have a certain amount of statistics, and finally a detailed discussions about the calculation of $\Upsilon(nS)$ production cross section with a part of the data collected in 2010 in pp collisions at $\sqrt{s} = 7$ TeV.

4.1 Monte Carlo based analysis: PDC09

In order to build and test a C++ based analysis framework for Υ analysis, we used a *PDC09*[2] production. Among several periods in this production,

[2]A massive MC production in pp collisions at $\sqrt{s} = 10$ TeV performed by ALICE Collaboration. At the time beginning of this analysis work, there were several scenar-

we chose LHC09a10 period in which generated $\mu^+\mu^-$ events from random species were mixed. This is called a *MUON cocktail*.

We analyzed this MC production regarding it as a real data and extracted Υ signals by fitting. Then we produced a transverse momentum distribution or a rapidity distribution. A benefit of analyzing MC production is that we have a concrete knowledge at the generation level, thus we can easily make sure that the analysis procedure is working properly by comparing the result we obtained from the reconstruction distribution with the one at the generation level.

The total number of event generated of this production is 3,420,400 with the following kinematic selection cuts applied at the stage of event generation:

- geometrical acceptance cuts on the polar angle of muons, $171^\circ < \theta^\mu < 178^\circ$,
- muon p_t threshold, $p_\mathrm{t}^\mu > 0.5$ GeV/c.

4.1.1 Signal extraction

The reconstructed $\mu^+\mu^-$ invariant mass distribution of PDC09 production in the mass range [0; 15 (GeV/c^2)] is depicted in Fig. 4.1. Above the $\mu^+\mu^-$ continuum in this spectrum, several significant peaks were seen: low mass resonances (ϕ and ρ), $c\bar{c}$ mesons (J/ψ and $\psi(2S)$), and $b\bar{b}$ mesons ($\Upsilon(1S)$, $\Upsilon(2S)$ and $\Upsilon(3S)$). We were focusing on the $b\bar{b}$ mesons, Υ family, in this analysis.

At first, it was crucial to find an appropriate distribution function for describing the shape of the spectrum in the $\Upsilon(nS)$ mass range [7; 12 (GeV/c^2)] in order to obtain the number of $\Upsilon(nS)$ signal. We chose the following distribution functions as candidates for the signal shape: the normalized Gaussian distribution function, the Crystal Ball function [104], and the normalized Gaussian distribution function convoluted with the inverted-Landau distribution function. The (single or double) exponential function is suitable to describe the $\mu^+\mu^-$ continuum. In Tab. 4.2, the definitions of each function and the parameters were summarized.

ios related to the possible beam energy in pp collisions at LHC after the accident in September 2008, and the most promising one was 10 TeV.

Table 4.2: A summary table about the definition of the distribution functions used in the analysis. G⊗L represents the normalized Gaussian convoluted with Landau function (an approximate analytic form).

Function	Definition	Parameters
Normalized Gaussian	$f_{\mathrm{G}}(m;N,\mu,\sigma)=\dfrac{N}{\sigma\sqrt{2\pi}}\cdot\exp\left(-\dfrac{(m-\mu)^2}{2\sigma^2}\right)$	N: normalization μ: Mean σ: standard deviation
Crystal Ball	$f_{\mathrm{CB}}(m;\alpha,n,\mu,\sigma,N)=\dfrac{N}{\sigma\sqrt{2\pi}}\cdot\begin{cases}\exp\left(-\dfrac{(m-\mu)^2}{2\sigma^2}\right), & \text{for } \frac{m-\mu}{\sigma}\geqslant-\alpha\\ A\cdot\left\{B-\dfrac{m-\mu}{\sigma}\right\}^{-n}, & \text{for } \frac{m-\mu}{\sigma}<-\alpha\end{cases}$ $where\ A=\left(\dfrac{n}{\lvert\alpha\rvert}\right)^n\cdot\exp\left(-\dfrac{\lvert\alpha\rvert^2}{2}\right),\ B=\dfrac{n}{\lvert\alpha\rvert}-\lvert\alpha\rvert$	α, n: random params (reproducing tails) N: normalization μ: Mean σ: standard deviation
Gauss⊗Landau	$f_{\mathrm{G}}\otimes f_{\mathrm{L}}(m;N,\mu,\sigma,w)=N\cdot\displaystyle\int_{-\infty}^{\infty}\exp\left(-\dfrac{(m-\mu)^2}{2\sigma^2}\right)\mathcal{L}\left(\dfrac{\mu-m}{0.5860\times w}\right)\mathrm{d}m$ $where\ \mathcal{L}(x)=\dfrac{1}{2\pi i}\displaystyle\int_{c-i\infty}^{c+i\infty}\exp(s\ln s+xs)\mathrm{d}s,\ \text{for } c>0$	N: normalization μ: Mean σ: standard deviation w: width
Exponential	$f_{\exp}(m;N,a)=N\cdot\exp(a\cdot m)$	N: normalization a: slope

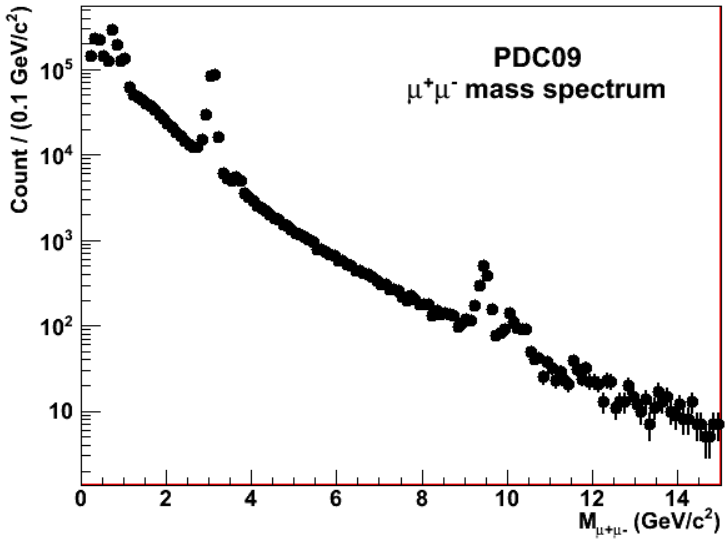

Figure 4.1: The $\mu^+\mu^-$ invariant mass distribution of PDC09 production in the mass range [0; 15 (GeV/c^2)] with logarithmic scaled Y-axis.

Table 4.3: The summary of the fit results of three different fit functions used in the fit to simulated $\Upsilon(1S)$ signal shown in Fig. 4.2.

Function	Mean (GeV/c^2)	σ (MeV/c^2)	χ^2/ndf
3×Gaussians	9.484 ± 0.002	89 ± 2	2.71
Crystal Ball + Gaussian	9.479 ± 0.002	92 ± 1	1.35
Gauss⊗Landau + 2×Gaussians	9.464 ± 0.000	94 ± 2	1.23

In order to test these functions, we performed a fit to the simulated $\Upsilon(1S)$ signal with each function. There were tails around the mean value of Υ due to the energy-loss of muon tracks. By adding one or two Gaussian functions, we can take into account the tails into the fit. The fit results were shown in Fig. 4.2 and summarized in Tab. 4.3. We chose the Gaussian convoluted with Landau function for the fit to $\Upsilon(1S)$ signal shape since it gave better χ^2/ndf, mean and standard deviation (mass resolution which is close to the designed value). For the fit to the continuum (background), single exponential function was chosen.

The global fit function used for Υ family in PDC09 production was ex-

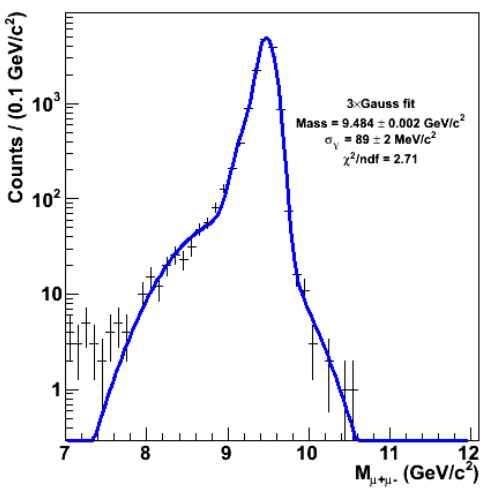

(a) 3 Gaussians

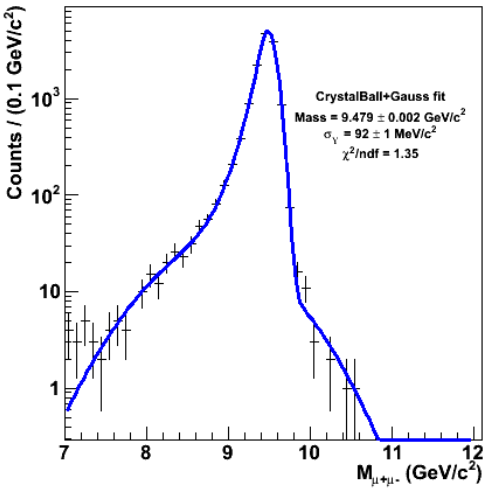

(b) Crystal Ball + Gaussian

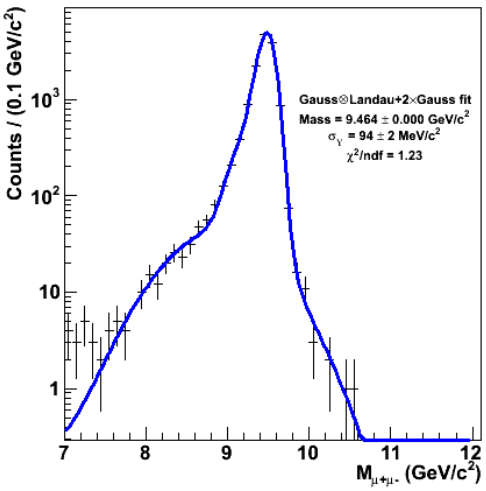

(c) Gauss⊗Landau + 2 Gaussians

Figure 4.2: The $\mu^+\mu$ invariant mass distribution (with logarithmic scaled Y-axis) of simulated Υ with the three different fits: mainly (a) Gaussian, (b) Crystal Ball and (c) Gaussian convoluted with Landau functions. In order to reproduce tails additional Gaussian functions were accumulated. Each fit gave χ^2/ndf: (a) 2.71, (b) 1.35 and (c) 1.23.

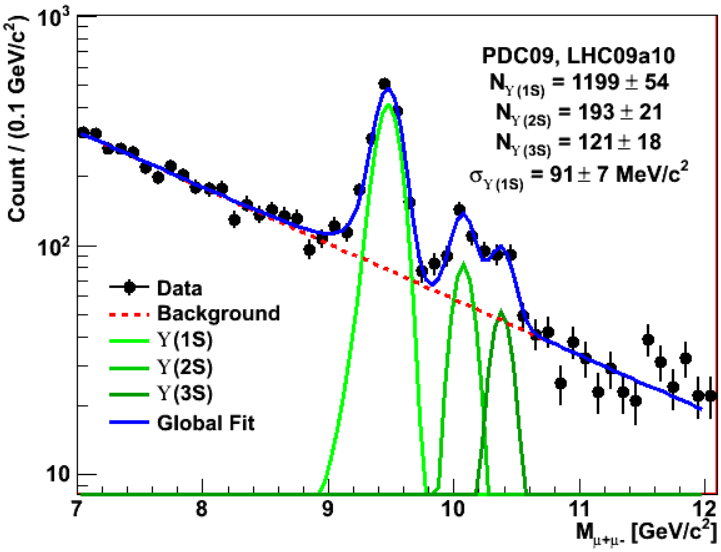

Figure 4.3: The $\mu^+\mu^-$ invariant mass distribution of PDC09 production (with logarithmic scaled Y-axis) with the global fit in the mass range [7; 12 (GeV/c^2)].

pressed as following,

$$f_{\rm global}(m) = \underbrace{f_{\rm exp}(m)}_{\text{background}} + \underbrace{f_{\rm G}\otimes f_{\rm L}(m) + f_{\rm G}(m) + f_{\rm G}(m)}_{\text{signals}}.$$

For $\Upsilon(2S)$ and $\Upsilon(3S)$ fit, the normalized Gaussian function was used. Here, the additional Gaussian functions were omitted since the entries in the tails are low in PDC09 production. We performed a fit to the $\mu^+\mu^-$ invariant mass distribution (shown in Fig. 4.1) with the global fit in the Υ family mass region [7; 12 (GeV/c^2)]. The signals extracted by the global fit for each resonance were: $N_{\Upsilon(1S)} = 1199\pm54$, $N_{\Upsilon(2S)} = 193\pm21$, and $N_{\Upsilon(3S)} = 121\pm18$. The mass resolution of $\Upsilon(1S)$ was 91 ± 7 MeV/c^2 close to the designed value because an ideal detector configuration was used in PDC09 production, and this was used to fix the mass resolution for $\Upsilon(2S)$ and $\Upsilon(3S)$ in the fit with the assumption that the mass resolutions of $\Upsilon(nS)$ are similar one another. Figure 4.3 showed the $\mu^+\mu^-$ invariant mass spectrum with the global fit. The fit results were summarized in Tab. 4.4.

Table 4.4: The summary of fit results of the global fit shown in Fig. 4.3.

States	N_{sig}	Mean (GeV/c^2)	σ (MeV/c^2)
$\Upsilon(1S)$	1,199±54	9.496±0.007	91±7
$\Upsilon(2S)$	193±21	10.07±0.01	91 (fixed)
$\Upsilon(3S)$	121±18	10.38±0.02	91 (fixed)

The p_t- and rapidity-dependence of $\Upsilon(1S)$ were also acquired by differentiating the Fig. 4.3 as a function of p_t (with 2 GeV/c intervals in p_t range [0; 10 GeV/c] and with 5 GeV/c intervals up to 20 GeV/c) and rapidity (with 0.3 intervals in rapidity range [-4.0; -2.5]) as shown in Fig. 4.4. The number of $\Upsilon(1S)$ extracted from the fit were summarized in Tab. 4.5. At some bins, we can not perform the "2-dimensional" correction on each pt and rapidity bin since they have not enough statistics. Thus we performed the "1-dimensional" correction on pt- and rapidity differential distribution, instead.

Accumulating the extracted number of $\Upsilon(1S)$ in Tab. 4.5, we were able to produce p_t- and rapidity-dependence of $N_{\Upsilon(1S)}$ ($dN_{\Upsilon(1S)}/dp_t$ and $dN_{\Upsilon(1S)}$ /dy) of the PDC09 production as shown in Fig. 4.5. The $dN_{\Upsilon(1S)}/dp_t$ and $dN_{\Upsilon(1S)}$/dy at the generation level were plotted in the same panels and it was shown that the generated and reconstructed distributions were not exactly the same, thus it was necessary to perform a simulation with the same configuration of PDC09 production to evaluate the reconstruction efficiency factor, and then proceed a correction procedure in order to reproduce the distributions at the generation level from the reconstruction spectra.

4.1.2 $\langle A \times \epsilon \rangle$ correction

MC event generations were performed to produce $\Upsilon(1S)$ signals including its family, $\Upsilon(2S)$ and $\Upsilon(3S)$ for the estimation of the acceptance times efficiency of the ALICE muon spectrometer in rapidity range $-4 < y < -2.5$. These MC events were generated in pp collisions at $\sqrt{s} = 10$ TeV energy. The kinematics of this generation were simulated with the parameterization phenomenologically scaled from the CDF experiment data in $p\bar{p}$ collisions at

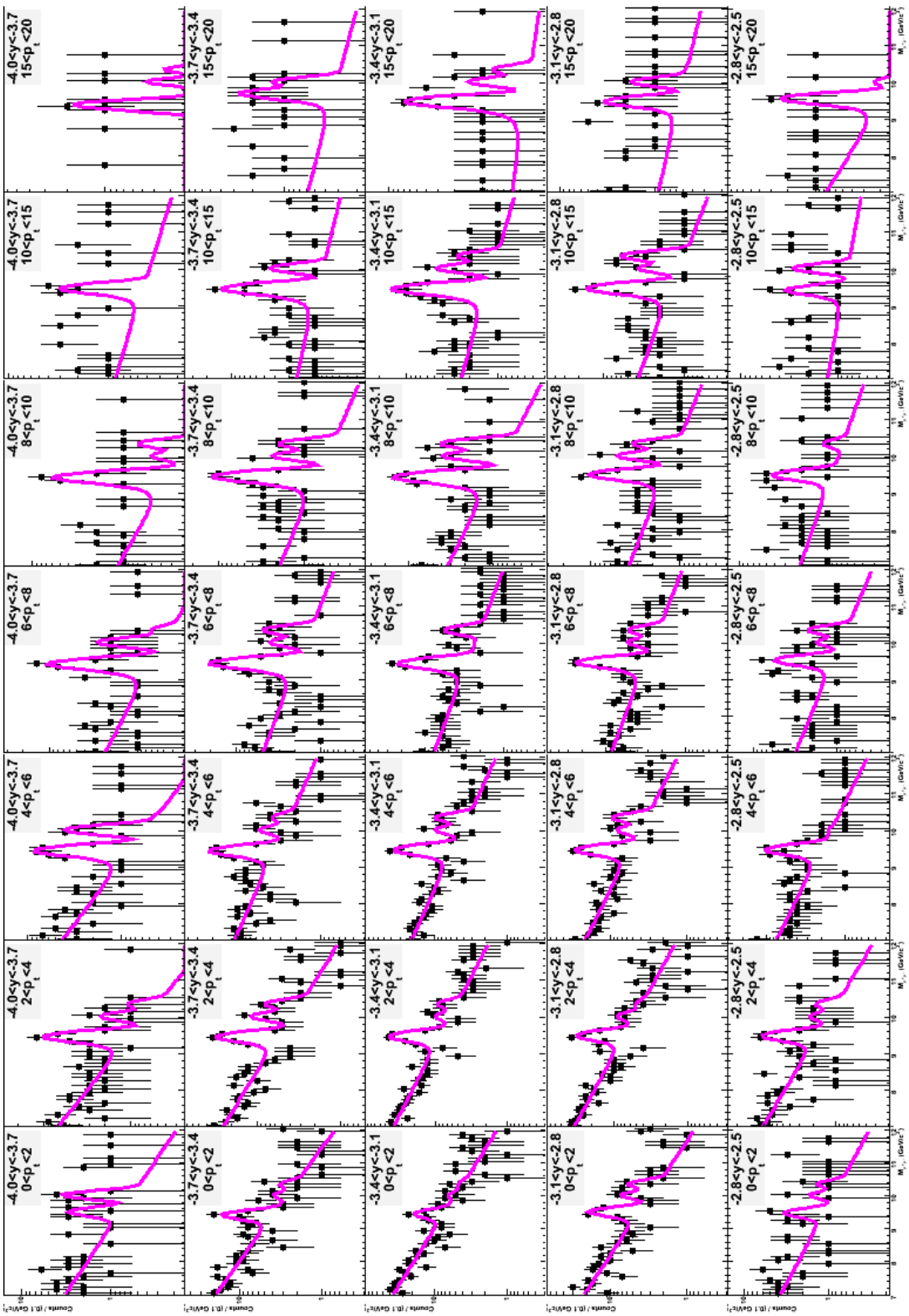

Figure 4.4: The $\mu^+\mu^-$ invariant mass distributions in mass range [7; 12 (GeV/c^2)] with different p_t and rapidity range. The intervals of p_t range were 2 GeV/c in [0; 10 (GeV/c)] and 5 GeV/c up to 20 GeV/c. Rapidity interval is 0.3.

Table 4.5: A summary table of $N_{\Upsilon(1S)}$ obtained from Fig. 4.4. Numbers in parentheses are the number of generated $\Upsilon(1S)$.

		p_t (GeV/c)						
		[0; 2]	[2; 4]	[4; 6]	[6; 8]	[8; 10]	[10; 15]	[15; 20]
y	[-4.0; -3.7]	$6 \pm 4(9)$	$26 \pm 6(31)$	$23 \pm 5(29)$	$28 \pm 6(34)$	$16 \pm 4(17)$	$3 \pm 1(6)$	$2 \pm 1(1)$
	[-3.7; -3.4]	$37 \pm 8(40)$	$75 \pm 11(95)$	$55 \pm 10(71)$	$55 \pm 9(67)$	$32 \pm 6(29)$	$14 \pm 3(16)$	$3 \pm 1(4)$
	[-3.4; -3.1]	$34 \pm 9(53)$	$106 \pm 13(105)$	$90 \pm 11(94)$	$57 \pm 9(58)$	$43 \pm 7(41)$	$16 \pm 3(18)$	$8 \pm 2(8)$
	[-3.1; -2.8]	$43 \pm 8(46)$	$70 \pm 11(76)$	$67 \pm 10(76)$	$62 \pm 9(65)$	$26 \pm 6(33)$	$18 \pm 3(17)$	$3 \pm 2(4)$
	[-2.8; -2.5]	$7 \pm 4(11)$	$23 \pm 6(23)$	$24 \pm 6(18)$	$13 \pm 5(17)$	$10 \pm 4(17)$	$3 \pm 1(4)$	$3 \pm 1(2)$

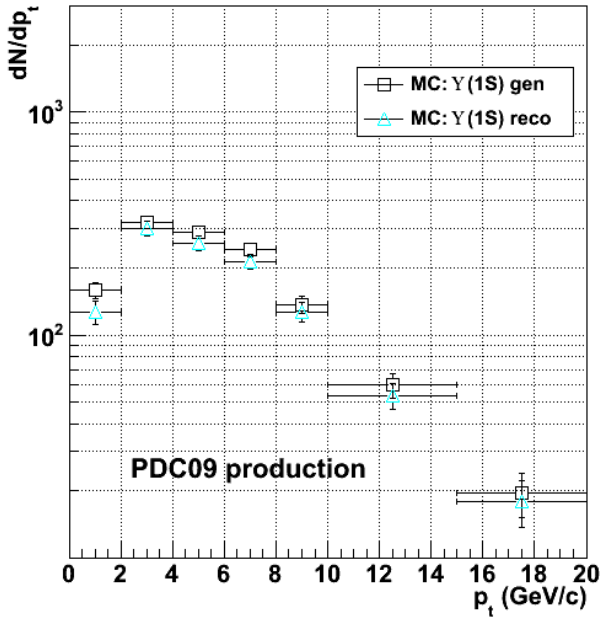

(a) p_{t}-dependence

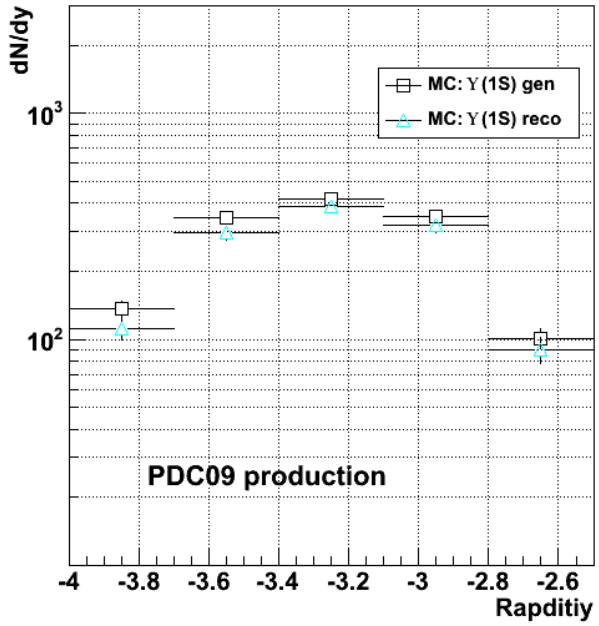

(b) Rapidity-dependence

Figure 4.5: (a) p_{t}- and (b) rapidity-dependence of $\mathrm{N}_{\Upsilon(1S)}$ for PDC09 production. Black square points represented the distribution of dN/dy or dN/dp_{t} of $\Upsilon(1S)$ at the generation level; cyan triangle points represented those of $\Upsilon(1S)$ at the reconstruction level.

Table 4.6: The number of generated Υ with two different configurations in the p_{t} range [0; 20 (GeV/c)].

Simulation conf.	4π	y-cut
$\mathrm{N}^{\mathrm{Gen}}_{\Upsilon\to\mu^+\mu^-}$	100,000	100,000
$\mathrm{N}^{\mathrm{Gen}}_{\Upsilon\to\mu^+\mu^-}(-4<\mathrm{y}<-2.5)$	4,658	29,507
$\mathrm{N}^{\mathrm{Rec}}_{\Upsilon\to\mu^+\mu^-}(-4<\mathrm{y}<-2.5)$	4,381	27,749

1.96 TeV energy [105]. $\mu^+\mu^-$ decay mode was enforced to each generated Υ and polarization was not considered in this simulation.

Two different simulations were performed in order to obtain the integrated acceptance times efficiency and the p_{t}- or rapidity-differential acceptance times efficiency. Total 100,000 events were produced for each simulation configuration.

- 4π simulation for evaluating the integrated acceptance times efficiency: Υ was generated in the full phase space, $-8 < \mathrm{y}^{\Upsilon} < 8$.
- y-cut simulation for evaluating the p_{t}- or rapidity-differential acceptance times efficiency: Υ was generated in a specific rapidity range, $-4.1 < \mathrm{y}^{\Upsilon} < -2.3$ (slightly larger than the ALICE muon spectrometer acceptance, $-4 < \mathrm{y} < -2.5$.

The statistics of these simulations were summarized in Tab. 4.6.

The mass resolution, in particular, was an important criterion in the analysis of Υ, since 100 MeV/c^2 resolution was the least requirement to resolve the Υ states. In this simulation, and the PDC09 production as well, a residual mis-alignment of the detector was taken into account at the reconstruction level in the simulation while an ideal alignment was used at the generation level. This was one of the scenarii concerning our detector status at the commissioning phase in which we assumed that our apparatus suffers few deteriorations. In addition, since we only generated Υ events without underlying events, we had to take into account the fact that the primary vertex was not able to be reconstructed by SPD (since there were not any other generated primary particles to be referred to reconstruct a primary vertex in

SPD) if we set a Gaussian distribution to the primary vertex in the simulation. That led to the fact that, consequently, the mass resolution of Υ could be worse than it was expected. In order to avoid this effect, the deviation of the primary vertex in the simulation had to be constrained without any displacements from the interaction point: (0, 0, 0)[3]. For instance, the effect of the standard deviation of z-component of the primary vertex of Υ, σ_{V_z}, was shown in Fig. 4.6. The Gaussian distribution convoluted with the Landau distribution was used to fit to the invariant mass distribution of Υ in order to obtain the mass resolution. For the case we set $\sigma_{V_z} = 5.3$ cm, the mass resolution we obtained was 149.1 MeV/c^2 (worse than the designed value); while the mass resolution of the case $\sigma_{V_z} = 0$ cm was 83 MeV/c^2 (better than the designed value). In this simulation, $\sigma_{V_z} = 0$ cm was set since it gave the mass resolution close to the one of PDC09 production, which was 91$\pm$7 MeV/c^2.

Assuming that we generated N number of $\Upsilon \rightarrow \mu^+\mu^-$ events, the only events with that both μ^+ and μ^- are in the ALICE muon spectrometer acceptance ($-4 < \mathrm{y} < -2.5$) can be reconstructed. We define:

- geometrical acceptance, A, as the ratio of the number of generated events with $\mu^+\mu^-$ inside the muon spectrometer, $\mathrm{N}^{\mathrm{gen}\in\mathrm{det}}_{\Upsilon\rightarrow\mu^+\mu^-}$, over the total number of generated events, $\mathrm{N}^{\mathrm{gen}}_{\Upsilon\rightarrow\mu^+\mu^-}$,
- reconstruction efficiency, ϵ, as the ratio of the number of reconstructed events, $\mathrm{N}^{\mathrm{rec}}_{\Upsilon\rightarrow\mu^+\mu^-}$, over the number of generated events with $\mu^+\mu^-$ inside the muon spectrometer, $\mathrm{N}^{\mathrm{gen}\in\mathrm{det}}_{\Upsilon\rightarrow\mu^+\mu^-}$.

Thus, the acceptance times efficiency of the ALICE muon spectrometer for $\Upsilon \rightarrow \mu^+\mu^-$ can be defined as,

$$(A \times \epsilon)_{\Upsilon\rightarrow\mu^+\mu^-} = \frac{\mathrm{N}^{\mathrm{rec}}_{\Upsilon\rightarrow\mu^+\mu^-}}{\mathrm{N}^{\mathrm{gen}}_{\Upsilon\rightarrow\mu^+\mu^-}}.$$

The integrated acceptance times efficiency of the process $\Upsilon(1S) \rightarrow \mu^+\mu^-$ in the ALICE muon spectrometer was calculated with the $\Upsilon(1S)$ dataset

[3]Each digit represents the standard deviation of the Gaussian distribution of a primary vertex, (σ_{V_x}, σ_{V_y}, σ_{V_z}).

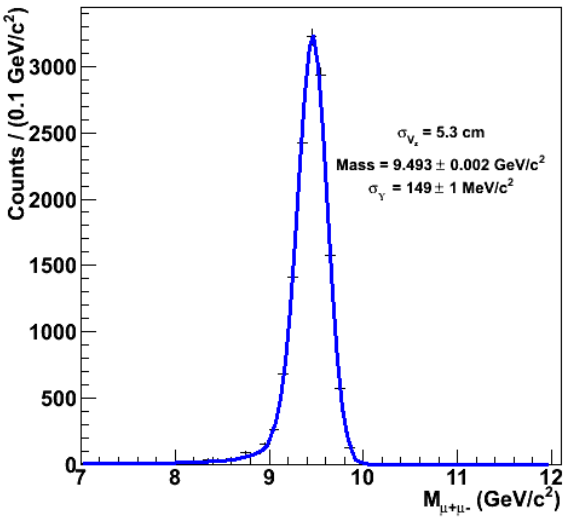

(a) $\sigma_{V_z} = 5.3$ cm

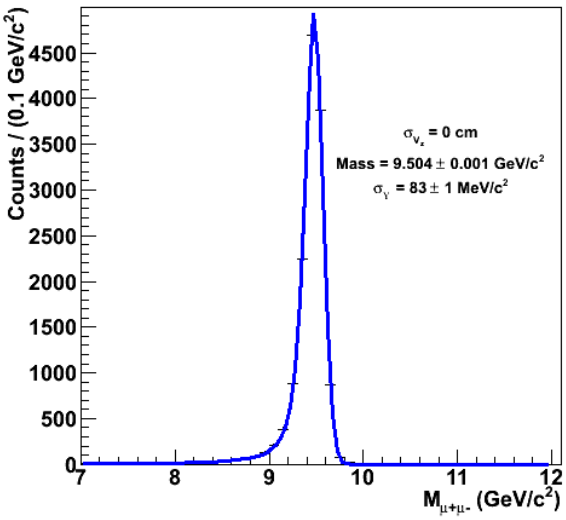

(b) $\sigma_{V_z} = 0$ cm

Figure 4.6: The effect of the distribution of z-component of a primary vertex, σ_{V_z}, on the mass resolution in the simulation. The case (a) $\sigma_{V_z} = 5.3$ cm showed that the mass resolution of Υ was 149.1 MeV/c^2, while (b) $\sigma_{V_z} = 0$ cm showed that the mass resolution was 83 MeV/c^2. The mass resolution of Υ in PDC09 production was 91$\pm$7 MeV/c^2.

Table 4.7: The integrated acceptance times efficiency of $\Upsilon \to \mu^+\mu^-$ in the ALICE muon spectrometer obtained from different simulations: in pp collisions at $\sqrt{s} = 10$ TeV energy (produced for the PDC09 analysis) and in pp collisions at $\sqrt{s} = 14$ TeV energy (the result of ALICE Physics Performance Report volume II [89]).

	4π	PPR vol. II
Integrated Acceptance	4.66%	
Integrated Acceptance $\times$ Reconstruction Efficiency	4.38%	4.41%

produced into full phase space (4π dataset) as defined above. The comparison with the acceptance times efficiency in ALICE Physics Performance Report volume II [89] estimated from a simulation performed in pp collisions at $\sqrt{s} = 14$ TeV was shown in Tab. 4.7. Considering the difference of the beam energy between two results, we were able to conclude that they are in the agreement.

We obtained the p_{t}- and rapidity-dependence of the acceptance times efficiency as well by using the y-cut dataset (see Fig. 4.7) for the purpose of correcting the $\mathrm{dN}_{\Upsilon(1S)}/\mathrm{dy}$ and $\mathrm{dN}_{\Upsilon(1S)}/\mathrm{d}p_{\mathrm{t}}$ obtained from PDC09 production. The correction worked properly since the corrected $\mathrm{dN}_{\Upsilon(1S)}/\mathrm{dy}$ and $\mathrm{dN}_{\Upsilon(1S)}/\mathrm{d}p_{\mathrm{t}}$ were well agreed with the generated ones as shown in Fig. 4.8. This correction procedure was applied to Υ analysis with the real data (see Sec. 4.3.5).

4.2 Expectation for Υ states

We performed a new simulation for Υ states with the realistic configuration including the current mis-alignment measurement and a fast simulation to draw the mass continuum deduced from the real data sample, LHC10e period data, in order to foresee the expectation of yield of Υ states for $\mathrm{L} = 1$ pb^{-1}

In order to determine the number of generated Υ states for $\mathrm{L} = 1$ pb^{-1},

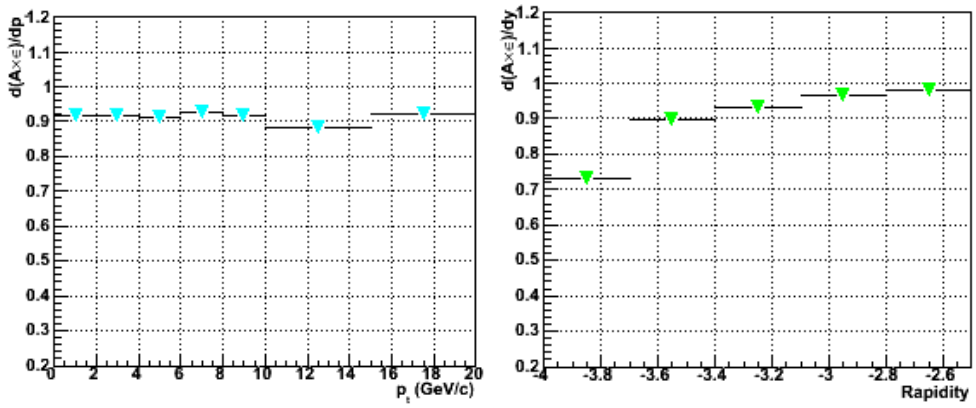

(a) $\mathrm{d}(A \times \epsilon)/\mathrm{d}p_\mathrm{t}$ (b) $\mathrm{d}(A \times \epsilon)/\mathrm{dy}$

Figure 4.7: p_t- and rapidity-differential acceptance times efficiency obtained from y-cut data set to be used for the correction on the $\mathrm{dN}_{\Upsilon(1S)}/\mathrm{dy}$ and $\mathrm{dN}_{\Upsilon(1S)}/\mathrm{d}p_\mathrm{t}$ of PDC09 production (see Fig. 4.5).

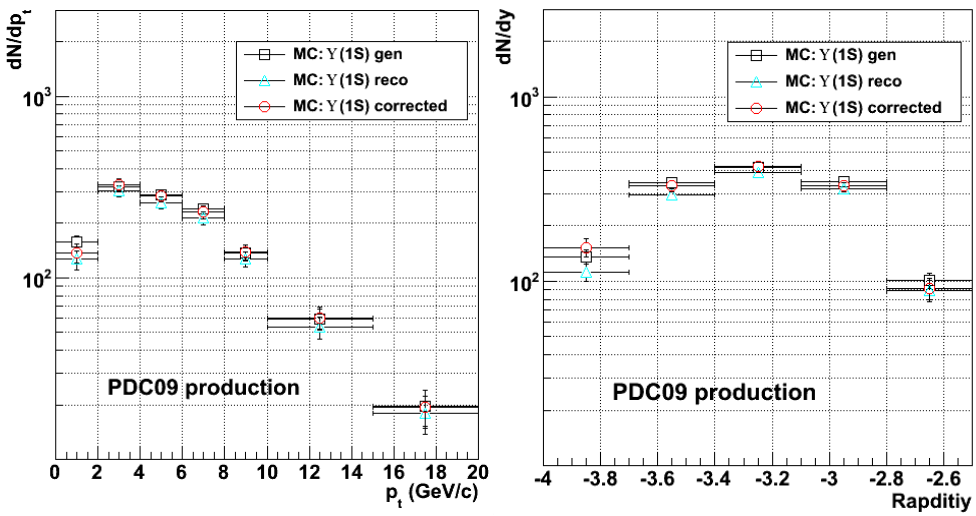

(a) p_t dependence (b) Rapidity dependence

Figure 4.8: (a) p_t and (b) rapidity distribution of Υ of PDC09 production after correction (red marker).

Table 4.8: A summary of the predicted production cross section of Υ states including direct and feedback in pp collisions at $\sqrt{s} = 7$ TeV and the estimation of the expected number of $\Upsilon(nS)$ produced for $\mathrm{L} = 1\ \mathrm{pb}^{-1}$.

	$\Upsilon(1S)$	$\Upsilon(2S)$	$\Upsilon(3S)$
$\sigma_{\mathrm{pp}\to\Upsilon(nS)}\mathrm{B}_{\Upsilon(nS)\to\mu^+\mu^-}$	11 nb	2.9 nb	1.6 nb
$\mathrm{N}^{\mathrm{expected}}_{\Upsilon(nS)}$	440	116	74

we estimated with the following expression,

$$\mathrm{N}_{\Upsilon\to\mu^+\mu^-} = \mathrm{L}\cdot\sigma_{\mathrm{pp}\to\Upsilon}\mathrm{B}_{\Upsilon\to\mu^+\mu^-}(A\times\epsilon)_{\Upsilon\to\mu^+\mu^-},$$

where, L is the integrated luminosity, $\sigma_{\mathrm{pp}\to\Upsilon}\mathrm{B}_{\Upsilon\to\mu^+\mu^-}$ is the cross section of Υ production with $\mu^+\mu^-$ decay in pp collisions and the integrated $(A\times\epsilon)_{\Upsilon\to\mu^+\mu^-}$. With the assumption of the integrated $A\times\epsilon \approx 4\%$ (deduced from the estimation at $\sqrt{s} = 10$ TeV in Tab. 4.7) and a predicted cross section of Υ states at $\sqrt{s} = 7$ TeV [106] (quoted in Tab. 4.8), the expected number of Υ states with $\mathrm{L} = 1\ \mathrm{pb}^{-1}$ were: 440 for $\Upsilon(1S)$, 116 for $\Upsilon(2S)$, and 74 for $\Upsilon(3S)$ (summarized in Tab. 4.8). With these numbers, we performed the simulation to generate each Υ state. The $\mu^+\mu^-$ invariant mass distribution for the expected Υ states from the simulation with $\mathrm{L} = 1\ \mathrm{pb}^{-1}$ are shown in Fig. 4.9. The mass resolution of $\Upsilon(1S)$ with the current mis-alignment was $\sim 230\ \mathrm{MeV/c^2}$, given by the Gaussian function fit. It was much worse than the designed value, $\sim 100\ \mathrm{MeV/c^2}$, thus it is difficult to separate the Υ resonances clearly.

For the background to be combined with the Υ signals, we performed a fast simulation by using Monte Carlo random generation with the $\mu^+\mu^-$ continuum extracted from a real data, LHC10e period data. The $\mu^+\mu^-$ invariant mass distribution of the LHC10e period data in mass range [4; 15 ($\mathrm{GeV/c^2}$)] was shown in Fig. 4.10c. The two exponential functions were used to fit the continuum in order to extract the normalization for the background and the shape of the continuum to be used for the Monte Carlo random generation for $\mathrm{L} = 1\ \mathrm{pb}^{-1}$. The mass region around Υ [8; 11 ($\mathrm{GeV/c^2}$)] was excluded in the fit. The following relation was used to deduce the normalization for

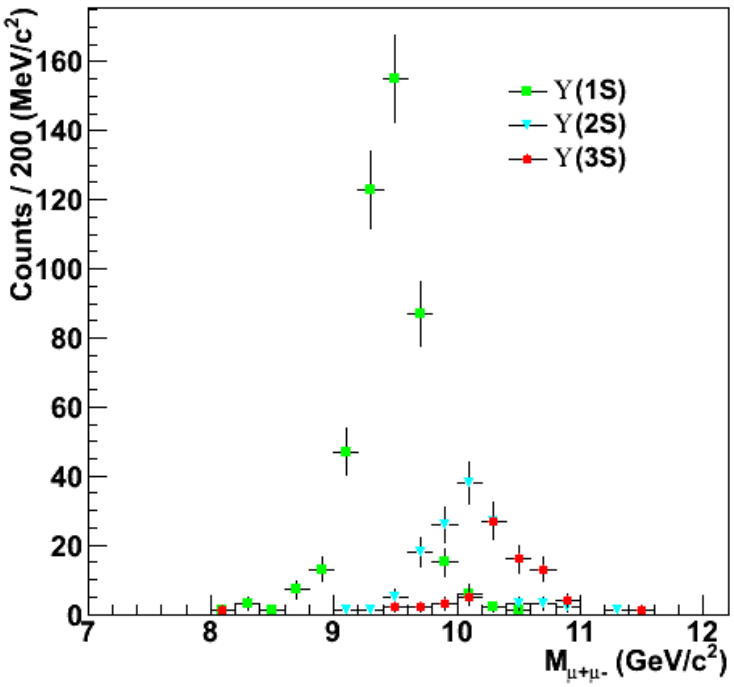

Figure 4.9: The $\mu^+\mu^-$ invariant mass distribution of Υ states, $\Upsilon(1S)$ (green), $\Upsilon(2S)$ (cyan), and $\Upsilon(3S)$ (red) of the simulation with current mis-alignment. The resonances are not separable due to the worse mass resolution, $\sim$ 230 MeV/c^2.

Table 4.9: Fit results of the predicted $\mu^+\mu^-$ mass spectrum for $L = 1$ pb^{-1} shown in Fig. 4.11. S/B and Significance were calculated in the range [Mean - 2σ; Mean + 2σ]

$N_{\Upsilon(1S+2S+3S)}$	Mean (GeV/c^2)	σ (MeV/c^2)	S/B	Signif.	χ^2/ndf
449 $\pm$ 51	9.47 ± 0.03	227 ± 30	0.42	5.05	0.92

the Monte Carlo random generation:

$$N_{cont}\Big|_{L=1\ pb^{-1}} = \frac{L(=1\ pb^{-1})}{L_{LHC10e}} \cdot N_{cont}^{LHC10e}[4; 15(GeV/c^2)],$$

where L/L_{LHC10e} was the scaling factor with $L_{LHC10e} = 22$ nb^{-1} and $N_{cont}^{LHC10e}[4;$ 15 (GeV/c^2)] = 974 (integration of the fit function over the given mass range) leading to:

$$N_{cont}\big|_{L=1\ pb^{-1}} = 44,273.$$

The shape of the background for the Monte Carlo random generation with this normalization was shown in Fig. 4.10d. Figure 4.11 showed the combined spectrum of Υ states with the continuum for $L = 1$ pb^{-1}. Two exponential functions (for the background) and Gaussian functions (for Υ states) were used for the fit and the fit results were summarized in Tab. 4.9.

Here, we were able to conclude that the current alignment needs to be improved in order to separate the Υ resonances and the expectation for $\Upsilon(nS)$ analysis with $L = 1$ pb^{-1} showed sufficient performance to measure the $\Upsilon(nS)$ production cross section, even with the current alignment.

4.3 Υ production cross section estimation

4.3.1 Method

We introduced an indirect method to calculate the Υ production cross section in pp collisions at $\sqrt{s} = 7$ TeV by using the J/ψ production cross

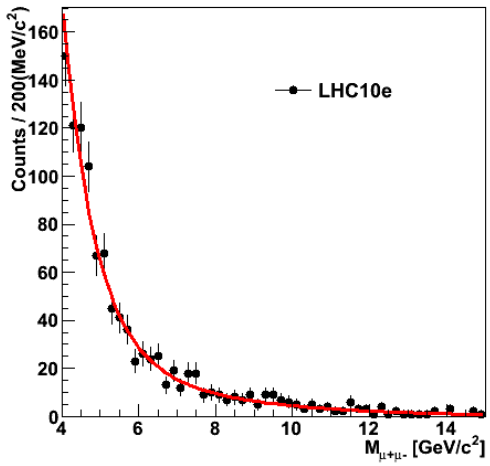

(a) LHC10e continuum

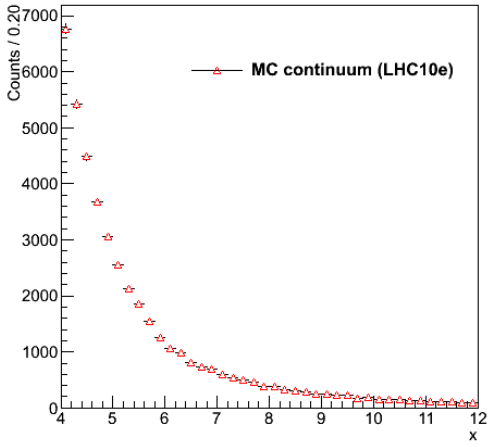

(b) MC continuum

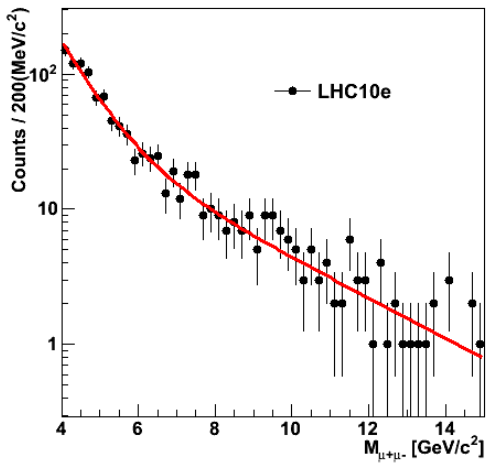

(c) LHC10e continuum (log-scaled)

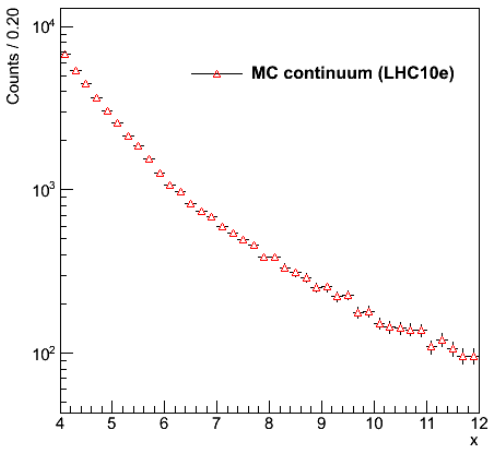

(d) MC continuum (log-scaled)

Figure 4.10: The $\mu^+\mu$ continuum of (a) LHC10e and (b) MC random generation from LHC10e continuum. Double exponential function (red curve) is used to fit to the LHC10e continuum in mass range [4; 15 (GeV/c^2)]. MC continuum is produced by a fast simulation from the LHC10e continuum.

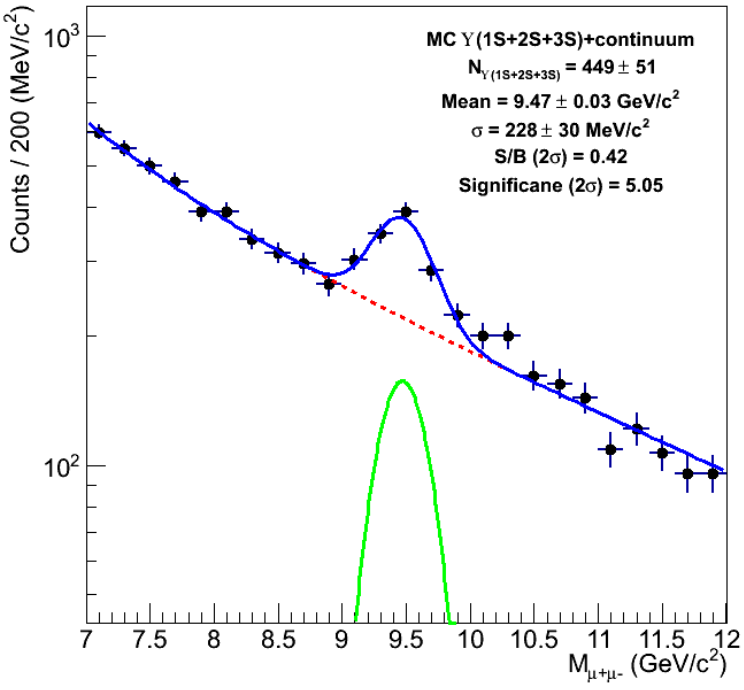

Figure 4.11: An expected $\mu^+\mu^-$ mass spectrum for L = 1 pb^{-1}. This is obtained from the combined spectrum of $\Upsilon(1S+2S+3S)$ and MC continuum from LHC10e. Double exponential function and Gaussian function are used to fit to the spectrum.

section measured at the same energy. With a given rapidity range, Δy,

$$\frac{\sigma^{\Delta y}_{pp\to\Upsilon}}{\sigma^{\Delta y}_{pp\to J/\psi}} = \frac{N^{corrected,\Delta y}_{\Upsilon\to\mu^+\mu^-}}{N^{corrected,\Delta y}_{J/\psi\to\mu^+\mu^-}} = \frac{N^{\Delta y}_{\Upsilon\to\mu^+\mu^-}}{\langle A\times\epsilon\rangle_{\Upsilon\to\mu^+\mu^-}\cdot B_{\Upsilon\to\mu^+\mu^-}} \cdot \frac{\langle A\times\epsilon\rangle_{J/\psi\to\mu^+\mu^-}\cdot B_{J/\psi\to\mu^+\mu^-}}{N^{\Delta y}_{J/\psi\to\mu^+\mu^-}}.$$

The measured production cross section of J/ψ for a rapidity range, $2.5 <$ y < 4[4] is

$$\sigma_{pp\to J/\psi}(2.5 < y < 4) = 6.31 \pm 0.25(stat.) \pm 0.80(syst.)^{+0.95}_{-1.96}(pol.)\ \mu b\ [107].$$

The advantage of this method was that we do not need to take into account the number of minimum bias event and its cross section in pp collisions in order to integrate the beam luminosities. Particularly, it would not be easy for a beam with high intensity in which high pile-up is expected. The disadvantage was that, to a certain extent, the Υ production cross section depends on the statistical and systematic uncertainties of the measurement of J/ψ production cross section.

4.3.2 Data selection

We analyzed a part of data taken in 2010 in pp collisions at $\sqrt{s} = 7$ TeV: LHC10g period data. Not all of runs, but selected runs in this period after Quality Assurance (QA) were used in this analysis. The QA for muon analysis consisted of three steps to build up a *run list*:

- selecting runs from ALICE e-logbook [108] with the following conditions: runs taken in a physics-run-partition of which including (at least) muon trigger, SPD and V0 as trigger detectors, and (at least) muon trigger/tracker, SPD and V0 as read-out detectors, having significant number of muon triggered events with L3 and dipole magnets ON ($-/-$ or $+/+$) during a data-taking period, and tagged as a *good run* after

[4]The ALICE muon spectrometer covers a negative η range, and thus a negative y range. However, since in pp collisions the physics is symmetric with respect to y = 0, we dropped the negative sign when quoting rapidity values in the result.

Table 4.10: Event statistics of LHC10g period for qualified runs taken from the Run Condition Table [109]. The total/analyzed number of events before/after applying physics selection and the number of $\mu^+\mu^-$ pair events analyzed in this analysis were shown. Note that the time sharing during this period was: 5 seconds for Min-bias and 114 seconds for Muons in every 120 seconds.

Run	Min-bias events	Muon events
135658	781,904	3,023,001
135704	517,258	2,142,017
135709	78,372	314,980
135712	25,116	130,667
135748	763,481	2,566,267
135761	285,485	1,139,315
135795	226,342	874,110
136177	4,347	27,643
136180	3,662	49,297
136189	46,029	664,396
136372	531,750	1,673,702
136376	423,106	1,193,929
Total	3,686,852	13,799,324
Analyzed	3,635,450	13,610,609
PhysSel	3,341,830	10,887,138
$N_{event}^{\mu^+\mu^-}$	-	497,979

data quality monitoring;

- rejecting runs having issues reported by DAQ operator or detector expert concerning detector malfunctioning and involving luminosity scans;
- building a table with the information about run quality for all subsystems which is called Run Condition Table (RCT) [109]. More detailed description about the QA for muon analysis can be found in [110].

Event statistics of LHC10g after QA was summarized in Tab. 4.10.

4.3.3 Event selection

The analysis cuts used in this analysis for event selection were:

- we accepted events having at least two muon tracks for di-muon analysis;

- geometrical acceptance cut, $-4.0 < \eta^{\mu} < -2.5$, and a cut on the radius at the end of front absorber, $17.6 < \mathrm{R_{abs}}^{\mu} < 89.5$ cm, to select a good muon track passing through the muon spectrometer. Especially, $\mathrm{R_{abs}}$ cut was used not only for reducing hadronic background from K, π decays, but also for reducing multiple scattering from the absorber itself. In order to help the understanding of the geometrical cuts, a schematic view was presented in Fig. 4.13;

- muon trigger p_{t}^{μ} cut on at least one muon track. In this analysis, high p_{t}^{μ} ($p_{\mathrm{t}}^{\mu} > 1$ GeV/c) trigger cut was required on both muon tracks in order to reduce background, and thus improved the significance of the signal. Especially, high p_{t}^{μ} trigger cut was efficient for Υ analysis since from the simulation the *survival rate* of Υ signal with respect to $p_{\mathrm{t}}^{\mu} > 1$ GeV/c cut was $\sim 90\%$ while that of J/ψ was less than 60%, see Fig. 4.12

4.3.4 Extracting signals

The analysis cuts defined above were equally applied to both J/ψ and Υ in the analysis. The invariant mass distributions in the J/ψ and Υ mass regions were plotted and the functions used for fitting to the distributions in order to extract the number of signal of each resonance were: exponential function for background, Crystal Ball function and Gaussian distribution function for J/ψ and Υ signal, respectively. Here, the higher states of $\Upsilon(1S)$ were taken into account to the fit since they were not negligible even with such a low statistics, unlike the higher resonance of J/ψ, $\psi(2S)$. For the fit of Υ resonances, three Gaussian functions were used in this analysis. The mean values of $\Upsilon(2S)$ and $\Upsilon(3S)$ were quoted from the Particle Data Group (PDG) [2] (see Tab. 4.1) and their mass resolutions (standard deviations) were fixed with the same value obtained from the $\Upsilon(1S)$ fit which was ~ 200 MeV/c^2. In particular, the normalization of the higher states were derived from the

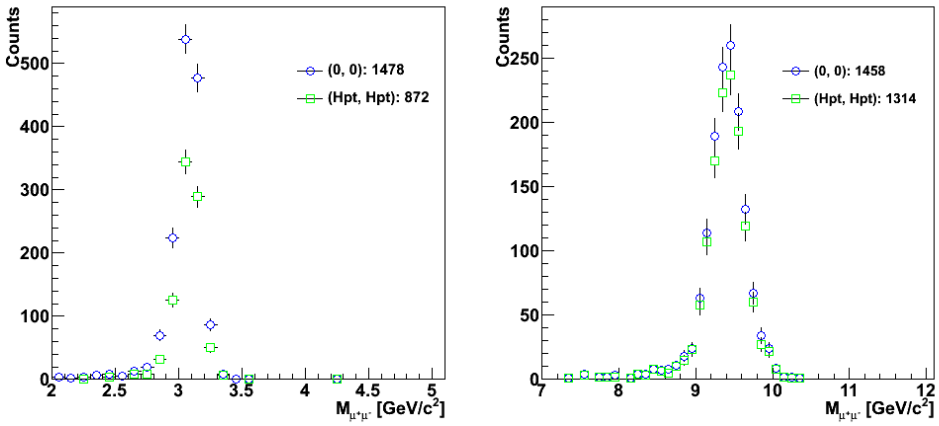

(a) (b)

Figure 4.12: The reconstructed $\mu^+\mu$ pairs of J/ψ and Υ simulation with different p_t trigger cuts: (0, 0) and (Hp_t, Hp_t). Hp_t represents ${p_t}^{\mu} > 1$ GeV/c. The survival rates with respect to (Hp_t, Hp_t) for each resonance are: (a) $\sim 59\%$ for J/ψ and (b) $\sim 90\%$ for Υ.

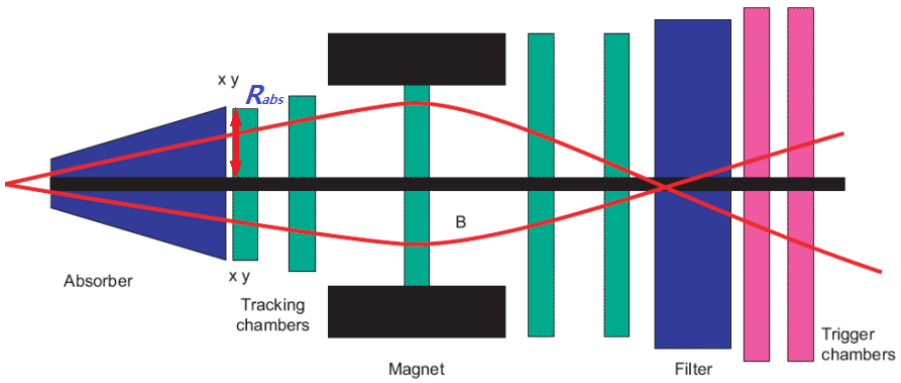

Figure 4.13: A schematic view of muon spectrometer together with muon tracks traversing within its geometrical acceptance and R_{abs} as well (see text).

Table 4.11: The summary of parameters for fitting to J/ψ and Υ mass distributions. The ratio of S (signal) and B (background), and significance of the signal were obtained in the range [Mean $- 2\sigma$; Mean $+ 2\sigma$].

States	J/ψ	$\Upsilon(1S+2S+3S)$
N_{signal}	3237 ± 107	18 ± 11
Mean (GeV/c^2)	3.125 ± 0.003	9.492 ± 0.229
σ (MeV/c^2)	80 ± 3	199 ± 91
S/B	5.489	0.562
Significance	11.570	2.622

Table 4.12: The extracted $N_{\Upsilon(1S+2S+3S)}$ from the invariant mass distributions with different binnings.

# bins	60	75	100	150
$N_{\Upsilon(1S+2S+3S)}$	14 ± 7	18 ± 11	19 ± 6	21 ± 7

CMS result of the $\Upsilon(nS)$ production cross section [111] as following:

$$N_{\Upsilon(2S)} = N_{\Upsilon(1S)} \times \frac{\sigma_{pp\to\Upsilon(2S)}}{\sigma_{pp\to\Upsilon(1S)}} \simeq N_{\Upsilon(1S)} \times 0.26,$$

$$N_{\Upsilon(3S)} = N_{\Upsilon(1S)} \times \frac{\sigma_{pp\to\Upsilon(3S)}}{\sigma_{pp\to\Upsilon(1S)}} \simeq N_{\Upsilon(1S)} \times 0.14.$$

The invariant mass distributions of J/ψ and $\Upsilon(1S+2S+3S)$ together with the fit were shown in Fig. 4.14 (see Tab. 4.11 for the fit results).

We had to make sure that the number of signal we extracted from the fit showed consistency with different binnings of the invariant mass distribution. In Fig. 4.15, we plotted the invariant mass distributions with different binnings in order to see the effect of a binning on the number of signal, particularly for $\Upsilon(1S+2S+3S)$. $N_{\Upsilon(1S+2S+3S)}$ for each binning was summarized in Tab. 4.12 and showed consistency within the errors.

4.3.5 $\langle A \times \epsilon \rangle$ estimation

We performed a realistic simulation taking into account the same detector condition when the data were collected. There is a collection of objects that

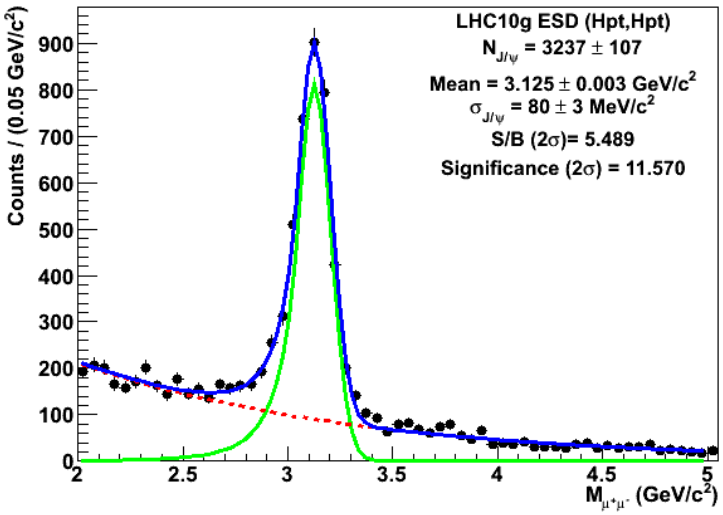

(a)

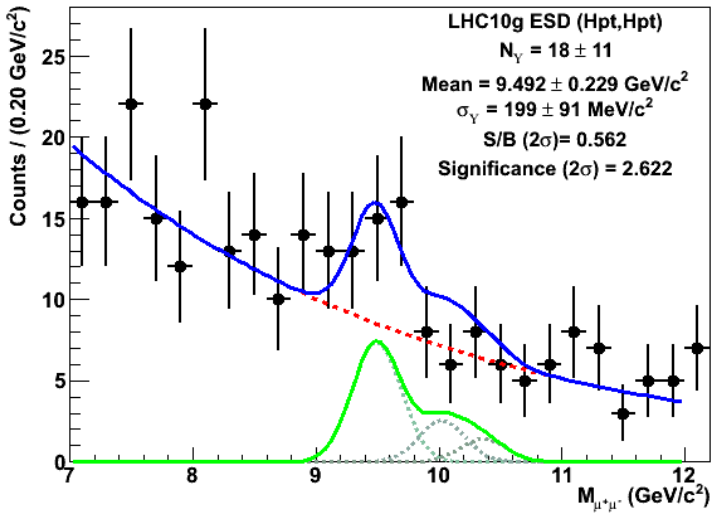

(b)

Figure 4.14: The invariant mass distributions in the (a) J/ψ and (b) Υ mass region, [2; 5(GeV/c^2)] and [7; 12(GeV/c^2)], respectively. The fit parameters were summarized in Tab. 4.11

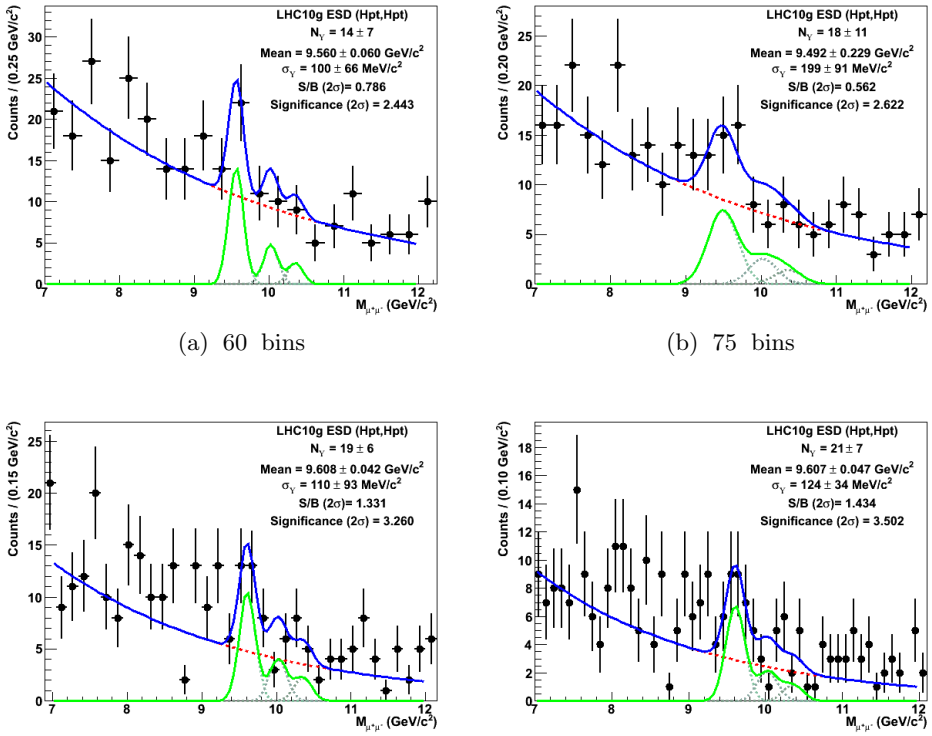

(a) 60 bins (b) 75 bins

(c) 100 bins (d) 150 bins

Figure 4.15: The invariant mass distribution of $\Upsilon(1S+2S+3S)$ with different number of bins: (a) 60, (b) 75, (c) 100, and (d) 150 bins. They showed the consistent number of signal for $\Upsilon(1S+2S+3S)$ within the errors.

stores sub-detector conditions corresponding to each data taking run. This collection is called *the Off-line Conditions Database* (OCDB). By specifying a run number which we want to simulate, we can take the corresponding OCDB objects into the simulation. In this way, we assumed that one can estimate precisely the acceptance times efficiency as close to an ideal value. A guideline of the OCDB settings for the realistic simulation, especially for muon analysis is presented here [112].

We produced 5,000 events of each J/ψ and $\Upsilon(1S)$ in $\mu^+\mu^-$ decay mode in a rapidity range $-4.1 < \mathrm{y} < -2.4$ for each run in the LHC10g period. The same kinematic cuts as described in Sec. 4.3.3 were applied to these events when we counted the number of generated/reconstructed events in order to evaluate the acceptance times efficiency. We also studied the effect of low ${p_\mathrm{t}}^\mu$ (${p_\mathrm{t}}^\mu > 0.5$ GeV/c) and high ${p_\mathrm{t}}^\mu$ (${p_\mathrm{t}}^\mu > 1$ GeV/c) trigger cuts on the acceptance times efficiency applying the different combination of these trigger cuts: (0, 0), (Lp_t, 0), (Lp_t, Lp_t), (Hp_t, 0), (Hp_t, Lp_t), and (Hp_t, Hp_t)[5] (see Fig. 4.16). As expected, the combination involving high p_t trigger cut decreased the acceptance times efficiency for J/ψ significantly while it was not true for $\Upsilon(1S)$. The average values of the acceptance times efficiency we obtained with (hpt, hpt) combination for each J/ψ and $\Upsilon(1S)$ were $\langle A \times \epsilon \rangle_{\mathrm{J}/\psi}^{(\mathrm{H}p_\mathrm{t},\mathrm{H}p_\mathrm{t})} \sim 14\%$ and $\langle A \times \epsilon \rangle_{\Upsilon(1S)}^{(\mathrm{H}p_\mathrm{t},\mathrm{H}p_\mathrm{t})} \sim 22\%$, respectively. The acceptance times efficiency for each run from the simulation was summarized in Tab. 4.13 and 4.14. The ratio of $(A \times \epsilon)_{\mathrm{J}/\psi}$ and $(A \times \epsilon)_{\Upsilon(1S)}$ as a function of run in LHC10g (see Fig. 4.17) showed a consistent trend versus runs that lead to the fact that we were able to safely use the average value of the acceptance times efficiency in the calculation of the $\Upsilon(nS)$ production cross section.

4.3.6 Results

We obtained a very preliminary result of the $\Upsilon(1S + 2S + 3S)$ production cross section by using the Eq. 4.1 with the $\langle A \times \epsilon \rangle$ for J/ψ and Υ obtained by realistic simulation (as described in Sec. 4.3.5), the branching ratio of which J/ψ and Υ decay into $\mu^+\mu^-$ (quoted in Tab. 4.1), and the number

[5] "0" meant that any of p_t trigger cut was not required.

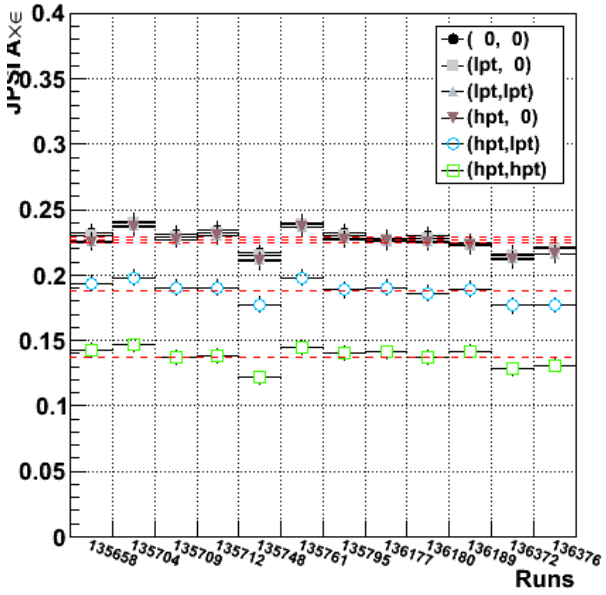

(a) $(A \times \epsilon)_{J/\psi}$ for each run

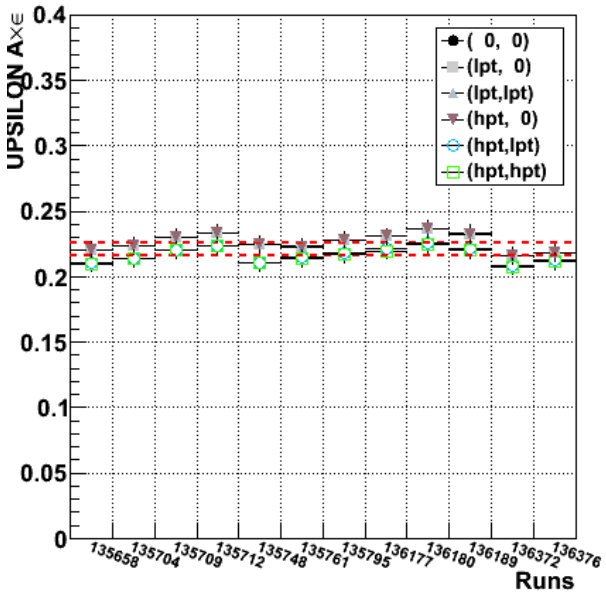

(b) $(A \times \epsilon)_{\Upsilon(1S)}$ for each run

Figure 4.16: The acceptance times efficiency as a function of run in LHC10g period for (a) J/ψ and (b) $\Upsilon(1S)$. The effects of $p_{\rm t}$ trigger cut combinations were presented: (0, 0), (L$p_{\rm t}$, 0), (L$p_{\rm t}$, L$p_{\rm t}$), (H$p_{\rm t}$, 0), (H$p_{\rm t}$, L$p_{\rm t}$), and (H$p_{\rm t}$, H$p_{\rm t}$). "L$p_{\rm t}$" represented the low $p_{\rm t}$ trigger cut ($p_{\rm t} > 0.5$ GeV/c) and "H$p_{\rm t}$" represented the high $p_{\rm t}$ trigger cut ($p_{\rm t} > 1$ GeV/c).

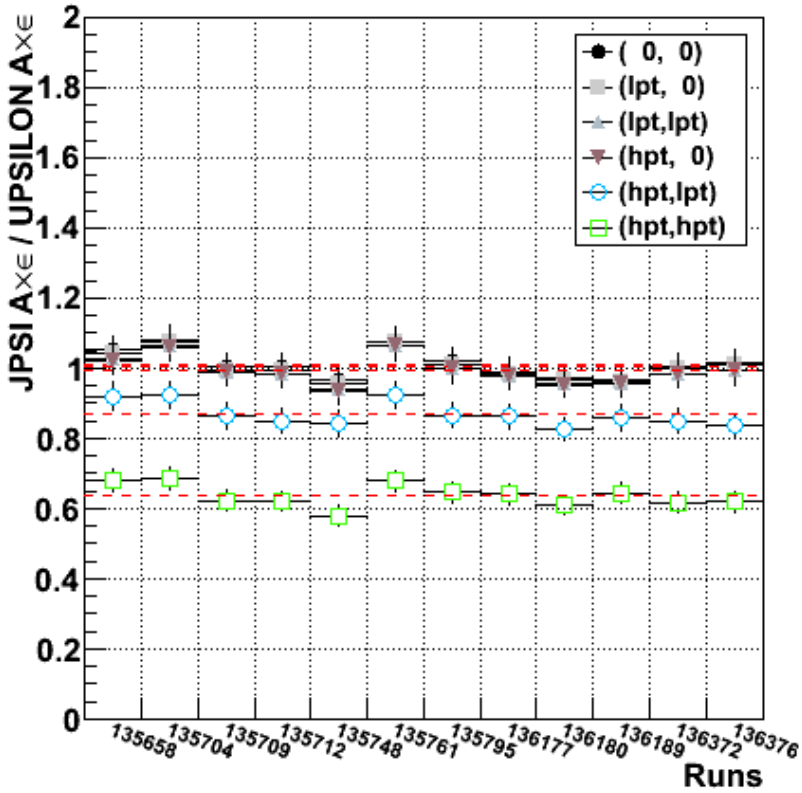

Figure 4.17: The ratio of $(A \times \epsilon)_{\mathrm{J}/\psi}$ and $(A \times \epsilon)_{\Upsilon(1S)}$ as a function of run in LHC10g. Showing a consistent trend versus runs was important because this meant that we were able to safely use the average value of the acceptance times efficiency in the calculation of the $\Upsilon(nS)$ production cross section.

Table 4.13: The acceptance times efficiency of J/ψ with different p_{t}-trigger cut combinations obtained by realistic simulation for each run in LHC10g period.

Run	$(A \times \epsilon)_{\mathrm{J}/\psi}$					
	(0, 0)	(lpt, 0)	(lpt, lpt)	(hpt, 0)	(hpt, lpt)	(hpt, hpt)
135658	$23.2 \pm 0.6\%$	$23.0 \pm 0.6\%$	$22.5 \pm 0.6\%$	$22.5 \pm 0.6\%$	$19.4 \pm 0.6\%$	$14.2 \pm 0.5\%$
135704	$24.1 \pm 0.6\%$	$24.0 \pm 0.6\%$	$23.7 \pm 0.6\%$	$23.7 \pm 0.6\%$	$19.8 \pm 0.6\%$	$14.6 \pm 0.5\%$
135709	$23.1 \pm 0.6\%$	$22.9 \pm 0.6\%$	$22.7 \pm 0.6\%$	$22.7 \pm 0.6\%$	$19.0 \pm 0.6\%$	$13.7 \pm 0.5\%$
135712	$23.4 \pm 0.6\%$	$23.2 \pm 0.6\%$	$23.0 \pm 0.6\%$	$23.0 \pm 0.6\%$	$19.0 \pm 0.6\%$	$13.8 \pm 0.5\%$
135748	$21.7 \pm 0.6\%$	$21.5 \pm 0.6\%$	$21.1 \pm 0.6\%$	$21.1 \pm 0.6\%$	$17.7 \pm 0.6\%$	$12.2 \pm 0.5\%$
135761	$24.0 \pm 0.6\%$	$23.9 \pm 0.6\%$	$23.7 \pm 0.6\%$	$23.6 \pm 0.6\%$	$19.8 \pm 0.6\%$	$14.5 \pm 0.5\%$
135795	$23.2 \pm 0.6\%$	$23.0 \pm 0.6\%$	$22.8 \pm 0.6\%$	$22.7 \pm 0.6\%$	$18.9 \pm 0.6\%$	$14.0 \pm 0.5\%$
136177	$22.8 \pm 0.6\%$	$22.6 \pm 0.6\%$	$22.5 \pm 0.6\%$	$22.5 \pm 0.6\%$	$19.1 \pm 0.6\%$	$14.1 \pm 0.5\%$
136180	$23.0 \pm 0.6\%$	$22.8 \pm 0.6\%$	$22.5 \pm 0.6\%$	$22.5 \pm 0.6\%$	$18.6 \pm 0.6\%$	$13.7 \pm 0.5\%$
136189	$22.5 \pm 0.6\%$	$22.4 \pm 0.6\%$	$22.2 \pm 0.6\%$	$22.2 \pm 0.6\%$	$18.9 \pm 0.6\%$	$14.2 \pm 0.5\%$
136372	$21.6 \pm 0.6\%$	$21.5 \pm 0.6\%$	$21.2 \pm 0.6\%$	$21.2 \pm 0.6\%$	$17.7 \pm 0.6\%$	$12.8 \pm 0.5\%$
136376	$22.1 \pm 0.6\%$	$22.0 \pm 0.6\%$	$21.6 \pm 0.6\%$	$21.6 \pm 0.6\%$	$17.7 \pm 0.6\%$	$13.1 \pm 0.5\%$
$\langle A \times \epsilon \rangle$	$22.9 \pm 0.1\%$	$22.7 \pm 0.1\%$	$22.5 \pm 0.1\%$	$22.4 \pm 0.1\%$	$18.8 \pm 0.1\%$	$13.7 \pm 0.1\%$

Table 4.14: The acceptance times efficiency of $\Upsilon(1S)$ with different p_{t}-trigger cut combinations obtained by realistic simulation for each run in LHC10g period.

Run	$(A \times \epsilon)_{\mathrm{J}/\psi}$					
	(0, 0)	(lpt, 0)	(lpt, lpt)	(hpt, 0)	(hpt, lpt)	(hpt, hpt)
135658	$22.1 \pm 0.6\%$	$22.0 \pm 0.6\%$	$22.0 \pm 0.6\%$	$22.0 \pm 0.6\%$	$21.0 \pm 0.6\%$	$21.0 \pm 0.6\%$
135704	$22.3 \pm 0.6\%$	$22.3 \pm 0.6\%$	$22.3 \pm 0.6\%$	$22.3 \pm 0.6\%$	$21.4 \pm 0.6\%$	$21.4 \pm 0.6\%$
135709	$23.0 \pm 0.6\%$	$23.0 \pm 0.6\%$	$23.0 \pm 0.6\%$	$23.0 \pm 0.6\%$	$22.0 \pm 0.6\%$	$22.0 \pm 0.6\%$
135712	$23.4 \pm 0.6\%$	$23.4 \pm 0.6\%$	$23.4 \pm 0.6\%$	$23.4 \pm 0.6\%$	$22.4 \pm 0.6\%$	$22.3 \pm 0.6\%$
135748	$22.5 \pm 0.6\%$	$22.5 \pm 0.6\%$	$22.5 \pm 0.6\%$	$22.5 \pm 0.6\%$	$21.1 \pm 0.6\%$	$21.0 \pm 0.6\%$
135761	$22.3 \pm 0.6\%$	$22.3 \pm 0.6\%$	$22.3 \pm 0.6\%$	$22.3 \pm 0.6\%$	$21.5 \pm 0.6\%$	$21.3 \pm 0.6\%$
135795	$22.8 \pm 0.6\%$	$22.8 \pm 0.6\%$	$22.8 \pm 0.6\%$	$22.8 \pm 0.6\%$	$21.8 \pm 0.6\%$	$21.7 \pm 0.6\%$
136177	$23.1 \pm 0.6\%$	$23.1 \pm 0.6\%$	$23.1 \pm 0.6\%$	$23.1 \pm 0.6\%$	$22.1 \pm 0.6\%$	$22.0 \pm 0.6\%$
136180	$23.6 \pm 0.6\%$	$23.6 \pm 0.6\%$	$23.6 \pm 0.6\%$	$23.6 \pm 0.6\%$	$22.5 \pm 0.6\%$	$22.4 \pm 0.6\%$
136189	$23.3 \pm 0.6\%$	$23.2 \pm 0.6\%$	$23.2 \pm 0.6\%$	$23.2 \pm 0.6\%$	$22.1 \pm 0.6\%$	$22.0 \pm 0.6\%$
136372	$21.6 \pm 0.6\%$	$21.6 \pm 0.6\%$	$21.6 \pm 0.6\%$	$21.6 \pm 0.6\%$	$20.8 \pm 0.6\%$	$20.8 \pm 0.6\%$
136376	$21.8 \pm 0.6\%$	$21.8 \pm 0.6\%$	$21.8 \pm 0.6\%$	$21.8 \pm 0.6\%$	$21.2 \pm 0.6\%$	$21.1 \pm 0.6\%$
$\langle A \times \epsilon \rangle$	$22.7 \pm 0.2\%$	$22.6 \pm 0.2\%$	$22.6 \pm 0.2\%$	$22.6 \pm 0.2\%$	$21.7 \pm 0.2\%$	$21.6 \pm 0.2\%$

of signals extracted in Sec. 4.3.4. The result was:

$$\sigma_{\Upsilon(1S+2S+3S)}(2.5 < \mathrm{y} < 4) = 52.6 \pm 32.4(stat.)\ \mathrm{nb}. \tag{4.1}$$

We also estimated the $\Upsilon(1S)$ production cross section by applying a scaling factor, 0.716 ± 0.017 (the ratio of $\Upsilon(1S)$ cross section over $\Upsilon(1S+2S+3S)$ cross section, obtained from the CMS result) to Eq. 4.1. The result was:

$$\sigma_{\Upsilon(1S)}(2.5 < \mathrm{y} < 4) = 37.7 \pm 23.2(stat.)\ \mathrm{nb}. \tag{4.2}$$

We compared our preliminary result with the CMS and LHCb [113] measurements of $\Upsilon(1S)$ in $\mu^+\mu^-$ decaying channel with different rapidity acceptances: $|\mathrm{y}| < 2$ (CMS) and $2 < \mathrm{y} < 4.5$ (LHCb). In order to make the comparison easier, all the results were expressed as the cross section multiplied by the branching ratio, $\sigma_{\Upsilon(1S)} \times \mathrm{B}_{\Upsilon \to \mu^+\mu^-}$. Unfortunately, we were not able to measure the rapidity-differential production cross section of $\Upsilon(1S)$ due to the insufficient statistics. Instead, we normalized our result to the rapidity unit by dividing the production cross section by 1.5 (the rapidity range of our apparatus, $2.5 < \mathrm{y} < 4$), thus we had:

$$\frac{\mathrm{d}\sigma_{\Upsilon(1S)} \times \mathrm{B}_{\Upsilon \to \mu^+\mu^-}}{\mathrm{dy}}(2.5 < \mathrm{y} < 4) = 0.62 \pm 0.38(stat.)\ \mathrm{nb}. \tag{4.3}$$

The estimation of any systematic uncertainties did not carry out in this analysis. However, if we consider the systematic uncertainties coming from the J/ψ production cross section measurement, the Eq. 4.1, including the polarization, we had the systematic errors for this estimation: +19.7%, − 33.5%. Consequently,

$$\frac{\mathrm{d}\sigma_{\Upsilon(1S)} \times \mathrm{B}_{\Upsilon \to \mu^+\mu^-}}{\mathrm{dy}}(2.5 < \mathrm{y} < 4) = 0.62 \pm 0.38(stat.)^{+0.12}_{-0.21}(syst.)\ \mathrm{nb}. \tag{4.4}$$

Figure 4.18 showed the rapidity-differential production cross section of $\Upsilon(1S)$ measured in pp collisions at $\sqrt{s} = 7$ TeV by CMS and LHCb compared with our preliminary result. The corresponding integrated luminosities were $\mathrm{L} = 3\ \mathrm{pb}^{-1}$ for CMS and $\mathrm{L} = 32.4\ \mathrm{pb}^{-1}$ for LHCb, respectively. As shown in Fig. 4.18, our preliminary result was consistent with the measure-

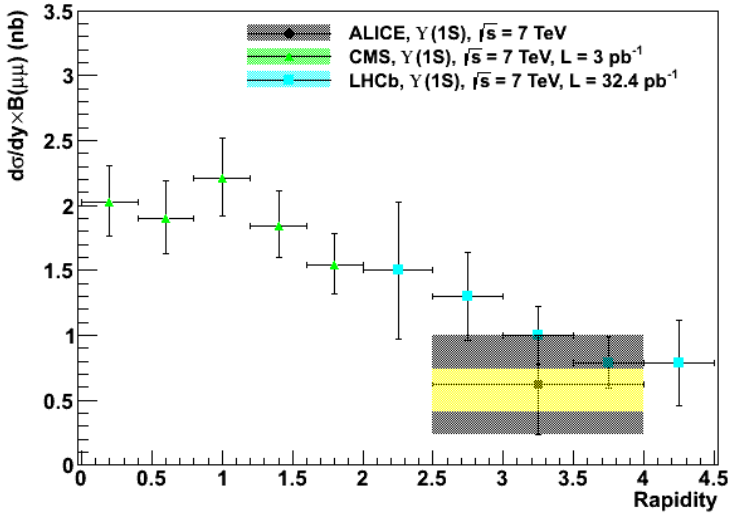

Figure 4.18: The rapidity-differential production cross section of $\Upsilon(1S)$ measured in pp collisions at $\sqrt{s} = 7$ TeV. The data points of CMS (corresponding integrated luminosity $\mathrm{L} = 3$ pb^{-1}) and LHCb (corresponding integrated luminosity $\mathrm{L} = 32.4$ pb^{-1}) were described by green triangles and cyan squares, respectively. The error bars included the statistical uncertainties and systematics. The black point represented our preliminary result estimated with LHC10g data. Statistical errors and systematic errors were indicated by black and yellow bands, respectively.

ments done by other experiments within the uncertainties. However, as the large statistical errors reflected the insufficient statistics, we needed to have more data in the future for the precise Υ measurement.

Chapter 5

Conclusion

The ALICE experiment is a general-purpose detector that has been built to search for, especially, the Quark-Gluon Plasma in heavy-ion collisions by using the highest energy beams in the world produced at LHC. The one of the most promising evidence for the existence of the QGP is the suppression of yield of heavy quarkonia production in heavy-ion collisons compared to pp collisions. The measurement of heavy quarkonia is crucial not only for heavy-ion physics, but also for pp physics since their production mechanism in hadronic collisions is still ambiguous. J/ψ has been well measured in the previous experiments, while Υ was only observed. Its measurement at LHC is expected to be feasible, and thus will reveal a new characteristic of the QGP and provide a new input to models of heavy quarkonia production as well.

J/ψ and Υ meansurement in their muon decay can be done in the ALICE experiment by using the forward muon spectrometer equipped with a set of absorbers, a warm dipole magnet, tracking and trigger stations. The ALICE muon spectrometer was well commissioned and now it is fully operational in pp and Pb–Pb collisions. The first measurement of J/ψ production cross section in leptonic decay channel, $\mu^+\mu^-$ and e^+e^-, in pp collisions at $\sqrt{s} = 7$ TeV has been published [107]. Also the first observation of the J/ψ suppression in Pb–Pb collisions has been performed recently [114].

In this thesis work, we participated in the development of the online monitoring software for shifters of muon trigger system based on two dif-

ferent DQM framework: MOOD and AMORE. The MOOD was heavily utilized at the commissioning phase, AMORE, a new DQM framework based on the publish-subscribe model upon a monitor-object (histogram) pool, now becomes a standard for the online DQM in the ALICE experiment. Two different versions of the online monitoring software for shifters have been developed and installed in the machines at the ALICE control room.

We started the data analysis for Υ by performing a simulation in order to obtain a the acceptance times efficiency correction factor. The PDC09 production, an official massive MC production, was used for testing the correction procedure developed specially for Υ analysis based on the correction framework. A part of data ($\sim 13\%$ of total muon events) collected in 2010, LHC10g period, was analyzed in this thesis. Although the statistics was not enough to perform further analysis for Υ, we estimated the total $\Upsilon(1S)$ production cross section, which was a very preliminary result. Our estimation showed an agreement with the CMS and LHCb measurement.

In 2011, we collected more statistics and observed a clear Υ signal as shown in Fig. 5.1[1]. This analysis was performed at the Laboratoire de Physique Corpusculaire in Clermont-Ferrand based on the committed analysis code developed in this thesis work. Further analysis, such as p_{t}- and rapidity-differential production cross sections and polarization in pp collisions as well as nuclear effect in Pb–Pb collisions for Υ, will be proceed, and more precise result of the production cross section of Υ in pp collisions will be done together with the improved detector alignment by using the GMS as well as the sigle muon analysis with magnetic field ON in near future.

[1] lopez@clermont.in2p3.fr

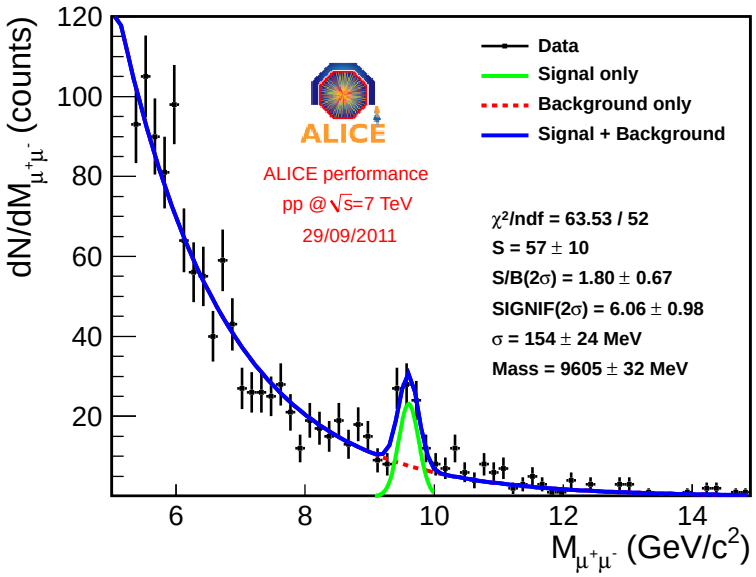

Figure 5.1: A performance plot for Υ signal. The analysis is done with a portion of data taken in 2011.

References

[1] D. J. Gross and F. Wilczek. *Phys. Rev. Lett.*, 30:1343, 1973.

[2] K. Nakamura *et al.* [Particle Data Group]. *J. Phys. G*, 37:075021, 2010.

[3] S. Bethke. *Eur. Phys. J. C*, 64:689–703, 2009. arXiv:hep-ph/0908.1135v2.

[4] F. Karsch. *Nucl. Phys. A*, 590:372, 1995.

[5] R. Stock. arXiv:0807.1610v1.

[6] R. Rapp, T. Schäfer and E. V. Shuryak. *Annals Phys.*, 280:35, 2000.

[7] F. Karsch and E. Laermann. *Quark Gluon Plasma 3*. World Scientific, 2004. arXiv:hep-lat/0305025v1.

[8] K. Rajagopal M. G. Alford and F. Wilczek. *Nucl. Phys. B*, 537:443, 1999.

[9] D. H. Rischke. *Progr. Part. Nucl. Phys.*, 52:197, 2004.

[10] K. Aamodt *et al.* [ALICE Collaboration]. *Phys. Rev. Lett.*, 105:252301, 2010.

[11] E598 Collaboration. *Phys. Rev. Lett.*, 33:1404, 1974.

[12] SLAC-SP-017 Collaboration. *Phys. Rev. Lett.*, 33:1406, 1974.

[13] S. W. Herb *et al. Phys. Rev. Lett.*, 39:252, 1977.

[14] W. R. Innes *et al. Phys. Rev. Lett.*, 39:1240, 1977. Erratum-ibid. **39** (1977) 1640.

[15] K. Ueno *et al. Phys. Rev. Lett.*, 42:486, 1979.

[16] G. Goldhaber *et al. Phys. Rev. Lett.*, 37:255, 1976.

[17] I. Peruzzi *et al. Phys. rev. Lett.*, 37:569, 1976.

[18] B. Knapp *et al. Phys. Rev. Lett.*, 37:882, 1976.

[19] C. Bebek *et al. Phys. Rev. Lett.*, 46:84, 1981.

[20] M. Basile *et al. Lett. Nuovo Cim.*, 31:97, 1981.

[21] N. Brambilla *et al. Eur. Phys. J. C*, 71:1534, 2011. arXiv:1010.5827v3.

[22] T. Matsui and H. Satz. *Phys. Lett. B*, 178:416, 1986.

[23] H. Satz. *Nucl. Phys. A*, 783:249, 2007. arXiv:hep-ph/0609197.

[24] Á. Mócsy and P. Petreczky. *Phys. Rev. Lett.*, 99:211602, 2007. arXiv:hep-ph/0706.2183v2.

[25] H. Paukkunen K. J. Eskola and C. A. Salgado. *JHEP*, 0904:065, 2009. arXiv:hep-ph/0902.4154.

[26] R. Vogt C. Lourenco and H. K. Woehri. *JHEP*, 0902:014, 2009. arXiv:hep-ph/0901.3054.

[27] R. Vogt. *Phys. Rev. C*, 71:054902, 2005. arXiv:hep-ph/0411378.

[28] R. Vogt. *Phys. Rev. C*, 61:035203, 2000. arXiv:hep-ph/9907317.

[29] NA50 Collaboration. *Eur. Phys. J. C*, 39:335, 2005. arXiv:hep-ex/0412036.

[30] R. Arnaldi for NA60 Collaboration. *Nucl. Phys. A*, 830:345c, 2009. arXiv:nucl-ex/0907.5004.

[31] PHENIX Collaboration. *Phys. Rev. Lett.*, 98:232301, 2007. arXiv:nucl-ex/0611020.

[32] PHENIX Collaboration. *Phys. Rev. Lett.*, 107:142301, 2011. arXiv:nucl-ex/1010.1246v1.

[33] C-H. Chang. *Nucl. Phys. B*, 172:425, 1980.

[34] G. A. Schuler. *CERN-TH.7170/94*. arXiv:hep-ph/9403387v1.

[35] CDF Collaboration. *Phys. Rev. Lett.*, 69:3704, 1992.

[36] S. Fleming E. Braaten, M. A. Doncheski and M. L. Mangano. *Phys. Lett. B*, 333:548, 1994. arXiv:hep-ph/9405407.

[37] E. Braaten and T. C. Yuan. *Phys. Rev. Lett.*, 71:1673, 1993. arXiv:hep-ph/9303205.

[38] J. P. Lansberg. *Eur. Phys. J. C*, 60:693, 2009. arXiv:hep-ph/0811.4005v1.

[39] H. Fritzsch. *Phys. Lett. B*, 67:217, 1977.

[40] J. F. Amundson *et al. Phys. Lett. B*, 372:127, 1996.

[41] G. T. bodwin *et al. Phys. Rev. D*, 72:014004, 2005. arXiv:hep-ph/0504014.

[42] CDF Collaboration. *Phys. Rev. Lett.*, 79:578, 1997.

[43] W. E. Caswell and G. P. Lepage. *Phys. Lett. B*, 167:437, 1986.

[44] CDF Collaboration. *Phys. Rev. Lett.*, 99:132001, 2007. arXiv:0704.0638v2.

[45] S. P. Baranov. *Phys. Rev. D*, 66:114003, 2002.

[46] D0 Collaboration. *Phys. Rev. Lett.*, 101:182004, 2008. arXiv:0804.2799v2.

[47] ALICE Collaboration. *Journal of Instrumentation*, 3:S08002, 2008.

[48] B. Adeva *et al. Nucl. Instrum. Meth*, A 289:35, 1990.

[49] ALICE Collaboration. *CERN-LHCC-99-012*. `http://edms.cern.ch/file/398932/1`.

[50] ALICE Collaboration. *CERN-LHCC-2000-001.* http://cdsweb.cern.ch/record/451098.

[51] ALICE Collaboration. *CERN-LHCC-2001-021.* http://cdsweb.cern.ch/record/519145.

[52] ALICE Collaboration. *CERN-LHCC-2000-012.* http://cdsweb.cern.ch/record/430132.

[53] A. Akindinov *et al. Eur. Phys. J.*, C 34:s325, 2004.

[54] ALICE Collaboration. *CERN-LHCC-98-019.* http://cdsweb.cern.ch/record/381431.

[55] Y. Andres *et al. Eur. Phys. J. Direct.*, C 4:25, 2002.

[56] ALICE Collaboration. *CERN-LHCC-99-004.* http://cdsweb.cern.ch/record/381432.

[57] ALICE Collaboration. *CERN-LHCC-2006-014.* http://cdsweb.cern.ch/record/932676.

[58] A. Fernández et al. *Nucl. Instrum. Meth. A*, 572:102, 2007.

[59] H.-U. Bengtsson and T. Sjöstrand. *Comput. Phys. Commun.*, 46:43, 1987.

[60] X.N. Wang and M. Gyulassy. *Phys. Rev.*, D 44:3501, 1991.

[61] M. Gyulassy and X.N. Wang. *Comput. Phys. Commun.*, 83:307, 1994.

[62] ALICE Collaboration. *CERN-LHCC-99-005.* http://cdsweb.cern.ch/record/381433.

[63] ALICE Collaboration. *CERN-LHCC-99-032.* http://cdsweb.cern.ch/record/451099.

[64] ALICE Collaboration. *CERN-LHCC-2004-025.* http://cdsweb.cern.ch/record/781854.

[65] J. Conrad *et al. ALICE Internal Note ALICE-INT-2005-025.* http://cdsweb.cern.ch/record/960438.

[66] J.R. Alfaro *et al. ALICE Internal Note ALICE-INT-2004-021.* https://edms.cern.ch/document/494149/1.

[67] B. Cheynis *et al. ALICE Internal Note ALICE-INT-2000-29.* https://edms.cern.ch/document/303914/1.

[68] B. Rapp. PhD thesis, Lyon University, Lyon France, 2004. http://lyoinfo.in2p3.fr/alice/BR/these-rapp.pdf.

[69] ALICE Collaboration. *CERN-LHCC-96-032.* http://cdsweb.cern.ch/record/314011.

[70] ALICE Collaboration. *CERN-LHCC-99-022.* http://cdsweb.cern.ch/record/401974.

[71] ALICE Collaboration. *CERN-LHCC-2000-046.* http://cdsweb.cern.ch/record/494265.

[72] S. Grigoryan *et al. ALICE Internal Note ALICE-INT-2002-06.* https://edms.cern.ch/document/338221/2.

[73] A. Rimai *et al. ALICE Internal Note ALICE-INT-1997-23.* https://edms.cern.ch/document/106754/1.0.

[74] Y. Le Bornec R. Wurzinger and N. Willis. *ALICE Internal Note ALICE-INT-1997-10.* https://edms.cern.ch/document/106932/1.0.

[75] B. Genolini J. Peyré and J. Pouthas. *ALICE Internal Note ALICE-INT-1998-28.* https://edms.cern.ch/document/106760/1.0.

[76] M. Arba *et al. ALICE Internal Note ALICE-INT-2002-17.* https://edms.cern.ch/document/347613/1.

[77] G. Chabratova *et al. ALICE Internal Note, ALICE-INT-2003-002.* https://edms.cern.ch/document/371480/1.

[78] A. Zintchenko *et al.* *ALICE Internal Note, ALICE-INT-2003-006.* https://edms.cern.ch/document/373848/1.

[79] P. Courtat *et al.* *ALICE Internal Note ALICE-INT-2004-026.* https://edms.cern.ch/document/504014/1.

[80] http://aliweb.cern.ch/Offline/.

[81] http://root.cern.ch.

[82] P. Saiz *et al.* *Nucl. Instrum. Meth.*, A 502:437, 2003.

[83] http://alien2.cern.ch.

[84] R. Brun *et al.* *CERN data handling division DD/EE/84-1*, 1985. http://wwwinfo.cern.ch/asdoc/geantold/GEANTMAIN.html.

[85] M. Goossens *et al.* *CERN program library long write-up W5013*, 1994. http://cdsweb.cern.ch/record/1073159.

[86] S. Agostinelli *et al.* *Nucl. Instrum. Meth*, A 506:250, 2003. CERN-IT-2002-003, http://cdsweb.cern.ch/record/602040.

[87] A. Fassò *et al.* *World Scientific, Singapore*, 1994.

[88] http://aliceinfo.cern.ch/Offline/Activities/ConditionDB.html.

[89] ALICE Collaboration. *J. Phys. G: Nucl. Part. Phys.*, 32:1295–2040, 2006.

[90] http://aliceinfo.cern.ch/Offline/Activities/Analysis/CORRFW.html.

[91] F. Antinori. http://aliceinfo.cern.ch/secure/Offline/sites/aliceinfo.cern.ch.secure.Offline/files/uploads/trigger/class-naming-01.pdf.

[92] http://aliweb.cern.ch/Offline/Activities/Analysis/AnalysisFramework/index.html#Physics_selection_for_2009.

[93] http://ph-dep-aid.web.cern.ch/ph-dep-aid.

[94] CERN ALICE DAQ Group. *ALICE Internal Note ALICE-INT-2005-015*. http://cdsweb.cern.ch/recorde/960457.

[95] Ö. Çobanoğlu S. Chapeland and F. Roukoutakis. *Fermilab, Batavia Illinois U.S.A.*, 2007.

[96] S. Chapeland and F. Roukoutakis. *Victoria BC, Canada*, 2007. http://cdsweb.cern.ch/record/1066450.

[97] B. C. Smith. PhD thesis, Massachusetts Institute of Technology, 1982. http://dspace.mit.edu/handle/1721.1/15961.

[98] http://www.mysql.com.

[99] L. Aphecetche *et al.* *ALICE Internal Note ALICE-INT-2005-012*. https://edms.cern.ch/document/591904/3.

[100] http://aliceinfo.cern.ch/static/Offline/dimuon/muon_html_release/README_raw.html.

[101] S. var der Meer. *ISR-PO/68-31*, 1968.

[102] K. Oyama. *CERN-Proceedings-2011-001*, page 39.

[103] M. Ferro-Luzzi. *Proceedings of the LHC Beam Operation Workshop - Evian, December 2010.* https://indico.cern.ch/getFile.py/access?contribId=8&sessionId=0&resId=0&materialId=paper&confId=107310.

[104] J. E. Gaiser. *SLAC-R-255*, 1982. Ph.D. Thesis.

[105] CDF Collaboration. *Phys. Rev.*, D 71:032001, 2005.

[106] M. Bedijidian *et al.* *arXiv:hep-ph/0311048v1*, 2003.

[107] K. Aamodt *et al.* [ALICE Collaboration]. *Phys. Lett. B*, 704:442, 2011. arXiv:1105.0380.

[108] https://alice-logbook.cern.ch.

[109] alimonitor.cern.ch/configuration.

[110] https://twiki.cern.ch/twiki/bin/view/ALICE/QAForTheSelectionOfGoodPhysicsRunsForMuonPhysics#pp_collisions.

[111] CMS Collaboration. *Phys. Rev. D*, 83:112004, 2011.

[112] https://twiki.cern.ch/twiki/pub/ALICE/PWG3Muon/OCDB4Sim.pdf.

[113] LHCb Collaboration. LHCb-CONF-2011-016.

[114] P. Pillot for the ALICE Collaboration. In *Quark Matter 2011*. Annecy, France, 2011. arXiv:1108.3795v1 [hep-ex].

[115] L. Betev and P. Chochula. *ALICE Internal Note ALICE-INT-2003-038*. https://edms.cern.ch/document/406391/2.

List of Tables

List of Figures

Appendix A

ALICE coordinate system

The ALICE coordinate system is a right-handed orthogonal Cartesian system with point of origin $x, y, z = 0$ at the IP as shown in Fig. A.1. The axis, azimuthal angle ϕ and polar angle θ are defined as follows [115]:

- x-axis is perpendicular to the beam direction aligned with the horizontal. Positive x is pointing to the LHC ring center from the IP,
- y-axis is perpendicular to the x-axis and the beam direction. Positive y is pointing upward from the IP,
- z-axis is parallel to the beam direction. Positive z is pointing toward the Point 1 of LHC from the IP,
- ϕ (azimuthal angle) increases with rotating counter-clockwise from x around the z-axis ($\phi = 0 \sim 2\pi$),
- θ (polar angle) increases from $z(\theta = 0)$ to $-z(\theta = \pi)$ through (positive) $x - y$ plane.

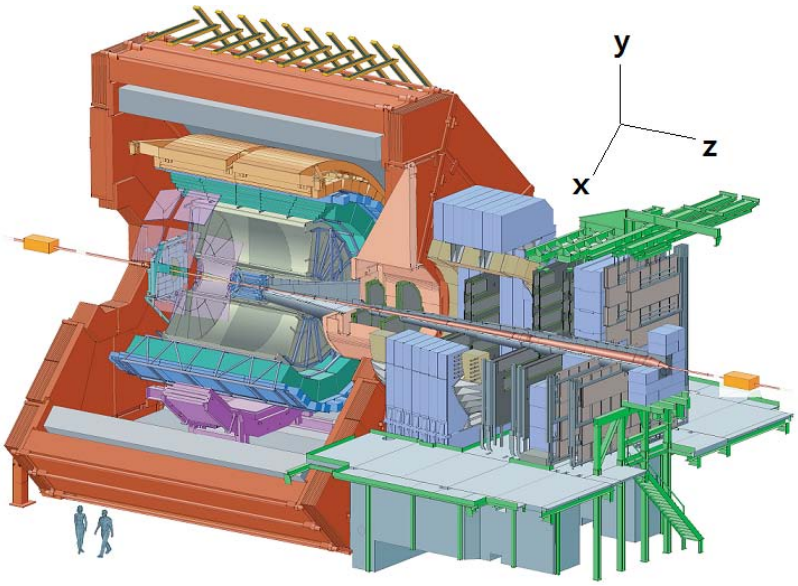

Figure A.1: The ALICE coordination system.

Appendix B

Kinematic variables

B.1 Transverse momentum

The transverse momentum, p_{t}, is the component of momentum of a particle in $x-y$ (transverse) plane (perpendicular to the beam direction) is defined by (see Figure):

$$p_{\mathrm{t}} = \sqrt{p_x^2 + p_y^2}$$

where p_x and p_y are the components of momentum in x- and y-axes.

B.2 (Pseudo-)Rapidity

Rapidity, y, is defined as

$$y = \frac{1}{2}\ln\left(\frac{E + p_z}{E - p_z}\right)$$

where E is the energy of a particle and p_z is the z-axis component of momentum. If the mass and momentum of a particle are unknown, pseudo-rapidity is useful. It is defined by

$$\eta = -\ln\left[\tan\left(\frac{\theta}{2}\right)\right]$$

where θ is the polar angle of a particle defined in Sec. A.

Appendix C

Error propagation

C.1 Sum (or Difference)

If the dependent variable x is the sum (of difference) of N measured quantities, u, v, ... , the propagation of the uncertainties are given by:

$$\sigma_x = \frac{1}{N}\sqrt{\sigma_u^2 + \sigma_v^2 + ...}$$

C.2 Multiplication (or Division)

If the dependent variable x is the multiplication (or division) of measured quantities, u and v, the propagation of the uncertainties are given by:

$$\left(\frac{\sigma_x}{x}\right)^2 = \left(\frac{\sigma_u}{u}\right)^2 + \left(\frac{\sigma_v}{v}\right)^2.$$

Appendix D

Glossary

ABC	Abstract Base Class
ACORDE	ALICE Cosmic Ray Detector
ADC	Analog Digital Converter
AGS	Alternating-Gradient Synchrotron
ALICE	A Large Ion Collider Experiment
AMORE	Automatic Monitoring Environment
AOD	Analysis of Data
API	Application Programming Interface
BNL	Brookhaven National Laboratory
CDH	Common Data Header
CEM	Color Evaporation Model
CERN	Conseil d'Européenne Recherche Nucléaire
CFL	Color-Flavor Locking
CMS	Compact Muon Solenoid
COM	Color Octet Model
CPV	Charged Particle Veto
CROCUS	Cluster Read Out Concentrator Unit System
CRT	Data Concentrator
CSM	Color Singlet Model
CTP	Central Trigger Processor
DAQ	Data Acquisition

DARC	Di-muon-trigger ALICE Read-out Controller
DATE	Data Acquisition and Test Environment
DCA	Distance of Closest Approach
DDL	Detector Data Link
DQM	Data Quality Monitoring
ECS	Experiment Control System
EMCAL	Electromagnetic Calorimeter
ESD	Event Summary Data
FEE	Front-End Electronics
FFT	Frontal Fan-out Trigger
FMD	Forward Multiplicity Detectors
FNAL	Fermi National Accelerator Laboratory
FRT	Frontal readout boards
FSM	Finite State Machines
FTD	Frontal Trigger Dispatching cards
GMS	Geometry Monitoring System
GSI	Gesellschaft für Schwerionenforschung
GUI	Graphic User Interface
HMPID	High Momentum Particle Identification Detector
IP	Interaction Point
ITS	Inner Tracking System
LEP	Large Electron Positron collider
LHC	Large Hadron Collider
LO	Leading Order
MANAS	Multiplexed Analogic Signal processor
MANU	MANAS Numérique
MARC	Muon Arm Readout Chip
MOOD	Monitoring of Online Data
MTR	Muon Trigger
NA49	North Area experiment 49
NLO	Next-to-leading Order
NNLO	Next-to-next-to-leading Order
NRQCD	Non-Relativistic QCD

OCDB	Off-line Conditions Data Base
PATCH	Protocol for ALICE Tracking Chambers
PDC	Physics Data Challenges
PHOS	Photon Spectrometer
PID	Particle Identification
PMD	Photon Multiplicity Detector
PMT	Photo Multiplier Tube
PPR	Physics Performance Report
PS	Proton Synchrotron
PWG	Physics Working Group
QA	Quality Assurance
QCD	Quantum Chromodynamics
QGP	Quark Gluon Plasma
RCT	Run Condition Table
RICH	Ring Imaging Cherenkov counters
RHIC	Relativistic Heavy-Ion Collider
RPC	Resistive Plate Chamber
SDD	Silicon Drift Detectors
SIS	Schwerionen-Synchrotron
SLAC	Stanford Linear Accelerator Center
SPD	Silicon Pixel Detectors
SPS	Super Proton Synchrotron
SSD	Silicon micro-Strip Detectors
T0	Time ZERO
TCI	Trigger CROCUS Interface
TOF	Time of Flight
TPC	Time Projection Chamber
TRD	Transition Radiation Detector
UML	Unified Modeling Language
V0	VZERO
VDM	Van deer Meer scan
ZDC	Zero Degree Calorimeter

ABSTRACT IN FRENCH

Analyse de la production de Υ dans les collisions pp à 7 TeV avec le spectromètre à muons de l'expérience ALICE

L'expérience ALICE est une des quatre grandes expériences fonctionnant auprès du LHC au CERN et dont le but principal est l'étude du plasma de quarks et de gluons (ou QGP) produit dans les collisions d'ions lourds. Une des observables priviligiées pour sonder le QGP est la production des quarkonia lourds qui doit être modifiée dans les collisions d'ions lourds comparée aux collisions pp. L'intérêt des quarkonia n'est pas limitée aux collisions d'ions lourds puisque leur mécanisme de production dans les collisions pp n'est pas encore très bien compris. Le but de ce travail de thèse est l'estimation de la section efficace de production des $\Upsilon(nS)$ en collision pp à une énergie de $\sqrt{s} = 7$ TeV à l'aide du canal de désintégration en dimuon avec le spectromètre à muons de l'expérience ALICE. Le spectromètre à muons dans ALICE est situé à grande rapidité $-4 < \mathrm{y} < -2.5$. Il consiste en un système d'absorbeurs, un dipôle chaud, des stations de trajectographie et de déclenchement. Ce travail de thèse décrit une contribution au logiciel de conrôle en ligne (online monitoring) du système de déclenchement des muons qui a été développé dans un esprit d'efficacité. Une partie des données enregistrées en 2010 a été analysée pour estimer la section efficace de production du Υ. La section efficace de production du J/ψ publiée par ALICE à la même énergie est exploitée par la méthode d'estimation. Le résultat préliminaire obtenu dans l'intervalle en rapidité $2.5 < \mathrm{y} < 4$ est $\sigma_{\Upsilon(1S)} \times \mathrm{B}_{\Upsilon(1S)\to\mu^+\mu^-} = 0.62 \pm 0.38(stat.) \pm^{0.12}_{0.21} (syst.)$ nb par unité de rapidité.

ABSTRACT IN KOREAN

CERN 거대 강입자 가속기 실험에서 ALICE 뮤온 분광기를 이용한 ϒ 입자 생성 연구

ALICE 실험은 다목적의 검출기로써 CERN LHC에서 행하는 중이온 충돌 실험을 통한 쿼크-글루온 플라즈(QGP) 연구를 위해 고안되었다. 중이온 충돌에서의 무거운 쿼코늄 생성은 QGP의 여러 탐색 방법 중 하나이다. 이러한 무거운 쿼코늄들에 대한 관심은 비단 중이온 충돌 실험에서만 국한 되지 않는다. 왜냐하면 양성자 충돌에서의 무거운 쿼코늄들의 생성 원리 또한 여전히 불명확하기 때문이다. 본 논문의 목적은 7 TeV 에너지의 양성자 충돌에서 뮤온쌍으로 붕괴하는 $\Upsilon(nS)$의 생성 단면적을 ALICE 뮤온 분광기를 이용하여 측정하는 것이다. ALICE 뮤온 분광기는 전방 신속도 지역($-4 < \mathrm{y} < -2.5$)에 위치해 있고, 다양한 흡수체들, 쌍극 자석, 입자 추적 장치 및 트리거 장치로 이루어져 있다. 원활한 데이터 수집을 돕기 위해 뮤온 트리거 장치를 위한 실시간 데이터 감시 소프트웨어를 개발했고, 이에 대한 상세한 과정이 논문에 기술되어 있다. ϒ 분석에는 2010년도 데이터 중 일부분이 사용되었다. ϒ 생성 단면적 계산 과정에는 앞서 발표된 같은 충돌 에너지에서의 J/ψ 생성 단면적이 이용되었다. 신속도 범위 $2.5 < \mathrm{y} < 4$에서의 사전 결과는 단위 신속도당 $sigma_{\Upsilon(1S)\times \mathrm{B}_{\Upsilon(1S)\to\mu^+\mu^-}} = 0.62 \pm 0.38(stat.)^{+0.12}_{-0.21}(syst.)$ nb 이다.

주제어: 거대 강입자 가속기, ALICE 검출기, 뮤온 분광기, ϒ, 생성 산란 단면적